Dissertation

submitted to the
Combined Faculties for the Natural Sciences and for Mathematics
of the Ruperto-Carola University of Heidelberg, Germany
for the degree of
Doctor of Natural Sciences

Put forward by
Dipl.Phys. Nina Malchus
born in Zweibrücken, Germany

Oral examination: 27 October 2011

On the spatial organization of cell organelles and diffusion of proteins in organelle membranes

Referees: Prof. Dr. Michael Hausmann
Prof. Dr. Matthias Weiss

Zusammenfassung

Im ersten Teil dieser Arbeit untersuchen wir die Diffusion des (un)gefalteten Transmembranproteins VSVG im Endoplasmatischen Retikulum (ER) lebender Zellen. Ungefaltetes VSVG wechselwirkt mit der Qualitätskontrollmaschinerie des ERs. Mit Hilfe der Fluoreszenzkorrelationsspektroskopie untersuchen wir diese Interaktionen in vivo. Wir finden, dass sowohl gefaltetes als auch ungefaltetes VSVG anomal diffundiert, die ungefaltete Form zeigt jedoch eine signifikant stärkere Anomalie. Die experimentellen Daten und begleitende Simulationen lassen darauf schließen, dass Teile der Qualitätskontrollmaschinerie ungefaltetes VSVG oligomerisieren und so zu einer stärker anomalen/behinderten Diffusion führen. Die Differenz in der Anomalie verschwindet wenn ungefaltetes VSVG einen Komplex mit dem Chaperon Calnexin bildet. Folglich löst Calnexin Oligomere auf und verhindert so eine Vergiftung des ERs.
Der zweite Teil der Arbeit widmet sich dem Einfluss der Zellform auf die innere Zellorganisation. Unsere Daten zeigen, dass die Positionen der Organellen in einem Zellensemble gleicher Geometrie stark variieren und so der Idee einer "Standardzelle" widersprechen. Abhängig von der Symmetrie der Zellgeometrie zeigt das Zentrosom allerdings eine bevorzugte Verschiebungsrichtung relativ zum Zellmittelpunkt. Simulationen der durch Mikrotubuli ausgeübten Schubkräfte auf das Zentrosom und der Abstoßung des Zellkerns durch die Zellmembran erklären die Positionierung.

Abstract

In the first part of this thesis, we study the diffusive motion of the (un)folded transmembrane protein VSVG in the endoplasmic reticulum (ER). Unfolded VSVG interacts with the ER's quality control machinery. These interactions are probed by Fluorescence Correlation Spectroscopy in vivo. We find that both, folded and unfolded VSVG show anomalous diffusion, however, the unfolded protein has a significantly stronger anomaly. Our experimental data and accompanying simulations suggest that parts of the quality control oligomerize unfolded VSVG, leading to a more anomalous/obstructed diffusion. The difference in anomaly subsides when unfolded VSVG is in a complex with its chaperone calnexin. Hence, calnexin dissolves the oligomers and thus prevents ER poisoning.
The second part of this work is dedicated to the influence of cell's shape on its internal organization. We find that organelle positions show large variations in ensembles of equally shaped cells, hence challenging the idea of a "standard cell". However, depending on cell geometry and symmetry, the centrosome shows a preferential direction of displacement from the cell center. Simulations that include pushing forces of microtubules on the centrosome and the repulsion of the nucleus by the cell membrane explain this localization.

Contents

Chapter 1

Introduction

Cells are the smallest living entities and the building blocks of each and every living organism. But not only big organisms are fascinating and complicated objects, but also a single cell is a system of incredible complexity. Its interior is divided into several compartments by membranes and its structure is ensured by the cytoskeleton (see Fig. 1.1). The DNA of each mammalian cell encodes for over 500.000 different species of proteins, the main class of functional biomolecules. For many of these, their biological function still remains to be elucidated. And yet, an understanding of how a cell works requires more than understanding the function of each protein on its own or clarifying its structure. A huge amount of proteins we know regulate gene expression, translation of other proteins or their activity. Thus, one has to deal not only with a vast amount of different species, but also with their interactions. Many of these interactions are not of permanent nature, but rather occur transiently. Functional units can be composed of several proteins or contain proteins and their substrate molecules and it is crucial for a cell how fast these units assemble and how long they stay in contact thereafter. In other words, dynamics and transport play an essential role in living cells.

The most prominent transport process in cells is diffusion, the non-directed random motion of single particles due to thermal energy. In a simple liquid or gas, the mean square displacement of a diffusing particle is proportional to time. The diffusion coefficient is a constant that reflects size and shape of the diffusing object and the viscosity of the medium. However, in crowded and complex systems such as cells, diffusion has been shown to be often anomalous, meaning that the mean square displacement scales as t^{α}, were α is the anomaly coefficient [1]. It has been shown that anomalous diffusion of molecules in cells promotes the process of finding an interaction partner by diffusion [2].

Obtaining data about dynamics on the single-cell level often requires going beyond classical biochemical and molecular biology experiments that suffer from several drawbacks: Many of these methods work either in vitro or by overexpressing and

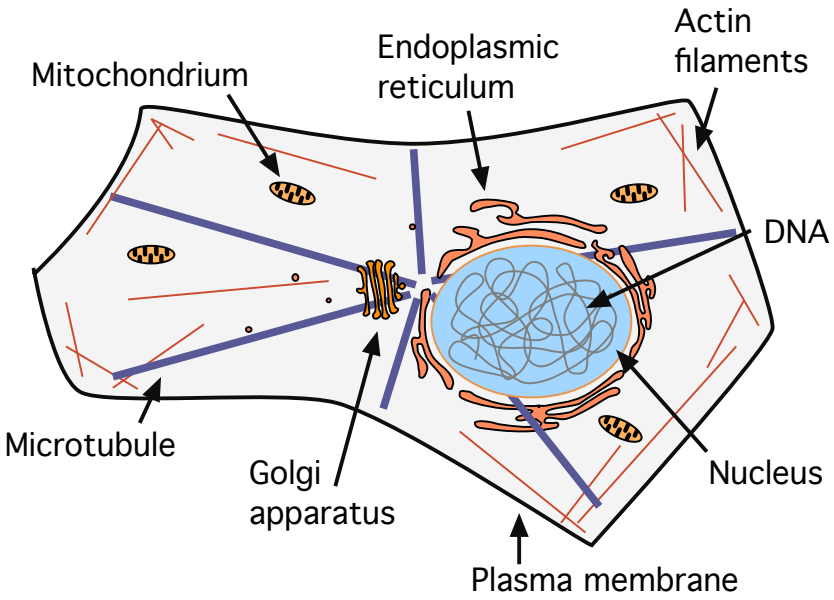

Figure 1.1: *Schematic picture of an eukaryotic (animal) cell. Its interior is structured into several membranous compartments, such as nucleus, endoplasmic reticulum, Golgi apparatus and mitochondria. Actin filaments and microtubules form part of the cytoskeleton that stabilizes cell shape. For details on specific functions of the cellular components see Chapter 3.*

extracting large amounts of a protein of interest from a cell population. This results in a complete loss of dynamic information and only provides evidence about the mean of a population.

Here, biophysical methods come to play. Methods such as light microscopy can provide information about the localization of cellular components within the cell or overall transport rates. Single-cell methods such as single-particle tracking or Fluorescent Correlation Spectroscopy provide information about dynamics of single molecules. Different kinds of motion, such as normal or anomalous diffusion, can be detected. Another valuable tool in cell biology are computer simulations. On one hand, simulations can be used to address questions that are not accessible with other methods such as microscopy due to limitations in the resolution. On the other hand, simulations and experiment often go hand in hand. Simulations, using parameters obtained from experiments, can often be employed to dissect necessary components of a system from additional regulatory factors with minor impact. Therefore, an understanding of fundamental mechanisms can be obtained.

Going from classical biochemical and molecular biology experiments to single-cell measurements brings along another advantage: These techniques allow to analyze not only the mean but also cell-to-cell variabilities in the quantities of interest.

When considering that some proteins are being present only in a few copies per cell while as much as millions of copies of other proteins exist, it becomes clear that protein species with low copy number are subject to the influence of noise of all kinds.

Indeed, several studies have highlighted the importance of noise in different biological contexts. For example, noise has been found to stabilize the function of circadian clocks, our internal time keepers [3]. When looking at the influence of transcription factor levels on gene expression in bacteria, the level of general transcription factors in the cell influences the total number of protein copies. Remarkably, deviations from the mean were found to be long lasting, i.e. they lasted over a whole cell cycle [4]. In virus infection, large cell-to-cell variability was observed and could be related with the cell context of the individual cell [5].

In this thesis, experimental measurements on the single-cell level combined with simulations were used to study two biological problems:

First, for cells, the quality control of each of their building blocks is of vital importance. Many mechanisms regulate and monitor the integrity of the different cellular components. For proteins, proper folding into their three-dimensional configuration is essential. Dysfunctioning of control mechanisms can lead to diseases. Cystic fibrosis, for example, is known to be caused by the retention and degradation of only slightly mutated proteins in the endoplasmic reticulum (ER), a membranous organelle at which transmembrane proteins are produced. Regardless of the mutation, these proteins had been fully functional if exported, i.e. the ER retention system and not the original mutation causes the disease phenotype. Hence, a good understanding of ER retention and quality control mechanisms is of high interest. In general, the ER retention mechanism is responsible for selective export of correctly folded proteins towards the cell's plasma membrane or the extracellular space and the retention and degradation of misfolded proteins. Until the first dynamic data were available, it had been believed that unfolded proteins are binding to immobile structures in the ER and thus cannot be exported. However, a fluorescence recovery after photobleaching study (FRAP) showed no difference in the diffusion of unfolded and folded proteins [6]. This highlights again the importance of dynamic information. However, FRAP relies on a large protein population. In contrast, Fluorescence Correlation Spectroscopy (FCS) is a on-average single-molecule technique and it can also provide information on shorter time scales than FRAP. With the help of FCS, we revisit the problem of diffusion of folded versus unfolded proteins in the ER and, indeed, we find a difference in their diffusive behavior. Accompanying computer simulations are employed to explain these findings.

Once proteins are correctly folded in the ER, they surpass the retention mechanism and are transported to the Golgi apparatus and further on to the plasma membrane. In contrast to the ER, which spans through most of the cell, the Golgi

is a compact organelle. Its localization is hence an interesting factor when looking at transport and cellular organization. Transport from the ER to the Golgi takes place in vesicles that fuse to form larger transport intermediates which are moved along rigid protein polymers, so-called microtubules. Microtubules are highly interesting polymers, possessing two states: a state in which they grow rapidly and one in which the shrink. They emanate from the centrosome, a small organelle which was named after the fact that it usually lies close to the cell center.

The second part of this thesis is dedicated to the influence of cell shape on the overall spatial organization of cellular organelles, such as nucleus, Golgi apparatus and centrosome. While the shape of culture cells varies largely, it is often highly regulated in tissues. Here, we use micropatterns to mimic this situation and obtain cells with a predefined geometry. We thus remove the external noise source 'cell shape' from our data and study the mean and variations of the internal spatial organization in this harmonized cell population. Again, the experimental data is completed with computer simulations.

In detail, the structure of this work is as follows:

Part one consists of three chapters, providing background information on (anomalous) diffusion, the biology of the questions studied and on Fluorescence Correlation Spectroscopy.

The second part contains the results on unfolded proteins in the ER. In Chapter 5 we look at the dynamic properties of unfolded versus folded transmembrane proteins in the endoplasmic reticulum of living cells. We employ the on-average single-molecule technique FCS to challenge already existing FRAP studies that suffer from the need for high expression levels of protein and monitoring a large protein pool at once. Indeed, we see a difference in the diffusion behavior of folded and unfolded proteins that has not been observed before. This difference can be linked to interactions with chaperones, proteins that assist folding and are very abundant in the ER. Computer simulations elucidate the underlying mechanism causing the differences in the anomaly. In the following chapter, accompanying classical molecular biology studies on one of the chaperons playing a role in the quality control in the endoplasmic reticulum are presented. Here, the question of protein localization within the secretory pathway is addressed.

In the third and last part, the spatial organization of organelles in equally shaped cells is studied. Chapter 7 describes methods to restrict cell growth in cell culture to certain areas of the substratum, and thus obtain cells of a certain geometry. The protocols and method setup are explained. In the last chapter, the findings about the spatial organization of cell organelles are reported. In particular, the positions still show a remarkable noise level, contradicting the idea of using micropatterns as a tool to obtain a "standard cell". However, depending on the geometry of the cell, the centrosome shows a preferential direction of displacement from the cell center. Computer simulations, modeling the cell shape, the nucleus

and microtubules explain the experimentally found positions of the nucleus and the centrosome.

Part I

Prerequisites

Chapter 2

Diffusion

In this chapter, a mathematical description of normal diffusion is given. Afterwards, the concept of anomalous diffusion and possible reasons for it to occur are introduced.

2.1 Normal diffusion

The Scottish Botanist Robert Brown (1773-1858) discovered the random motion of small particles in solution when observing pollen under the microscope. "Brownian motion", thermally driven motion, is the microscopic origin of diffusion. The mathematical description was given by Einstein in 1905. Before that, Fick had already successfully described diffusion macroscopically with the famous differential equation of diffusion (see Eq. (2.3)) [7].

When treating diffusion microscopically in one dimension, one looks at a particle performing a random walk on a lattice. At each time point, it jumps with 50% probability one step to the left or to the right. The process is Markovian, i.e. the probability for a jump into any direction does not depend on any events in the past. The probability distribution function $P(x,t)$ of having moved a distance x from the starting point at time t is given by a binomial distribution.

Due to the central limit theorem, the probability distribution function in a d-dimensional space approaches a Gaussian for a large number of steps.

$$P(x,t) = \frac{1}{(4\pi Dt)^{\frac{d}{2}}}\, e^{-\frac{|x|^2}{4Dt}} \tag{2.1}$$

Here, D denotes the diffusion coefficient, given in units $\frac{m^2}{s}$. The Gaussian proba-

bility distribution is completely characterized by its first and second moment.

$$\begin{aligned} \langle x \rangle &= 0 \\ \left\langle x^2 \right\rangle &= 2dDt \end{aligned} \tag{2.2}$$

As a consequence, the mean square displacement (2.2) in normal diffusion grows linearly in time. If at $t = 0$ all particles are concentrated at $x = 0$, the width of their distribution spreads according to Eq. (2.2).

Macroscopically, (concentration) diffusion can be described by the diffusion equation:

$$\frac{\partial n(\vec{r}, t)}{\partial t} = D\Delta n(\vec{r}, t) \tag{2.3}$$

which can be obtained from Fick's first law $\vec{j} = -D\nabla n$, which states that the flow $\vec{j}$ arises from a concentration gradient, and the continuity equation $\frac{\partial n}{\partial t} = -\nabla\vec{j}$. Eq. (2.3) can also be interpreted in terms of probabilities $P(\vec{r}, t)$ instead of concentrations $n(\vec{r}, t)$. Its solution then represents the probability of finding a particle at place $\vec{r}$ at time t. With the initial condition $P(0, 0) = \delta(\vec{r}, t)$ one recovers Eq. (2.1).

2.2 Anomalous diffusion

All diffusion processes for which the mean square displacement behaves as

$$\left\langle x^2 \right\rangle = 2d\Gamma t^{\alpha} \tag{2.4}$$

with $\alpha \neq 1$ are called anomalous. For α smaller than unity the motion is said to be subdiffusive, and for $\alpha > 1$ it is called superdiffusive. For $\alpha = 1$ one obtains normal diffusive behavior. In the case of ballistic motion $\alpha = 2$ holds true. The transport coefficient Γ has the dimension of an area per fractional time ($\frac{\mu m^2}{s^{\alpha}}$). Heuristically, one can introduce a time-dependent diffusion coefficient $D(t) = \Gamma t^{\alpha-1}$ in analogy to the diffusion constant D for normal diffusion. For anomalous diffusion processes, the probability distribution function now deviates from the Gaussian derived for normal diffusion. The resulting mean square displacement as a function of time is shown in Fig. 2.1.

Anomalous diffusion has been observed for various systems, e.g. subdiffusion of charges in amorphous semiconductors [8] or of proteins in cells [9]. Superdiffusion has for example been seen in turbulent flow [10] or in bacterial motion [11].

2.2.1 Mechanisms causing anomalous diffusion

Anomalous diffusion generally arises when the probability distribution function $P(x, t)$ for being at a certain distance x from the starting point at time t cannot

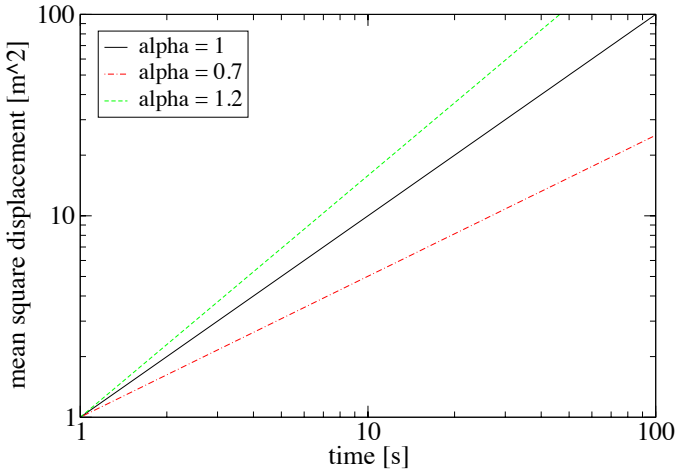

Figure 2.1: *Mean square displacement over time, for normal diffusion ($\alpha = 1$) , subdiffusion ($\alpha = 0.7$) and superdiffusion ($\alpha = 1.2$).*

be described by a simple Gaussian as in Eq. (2.1) or in other words, when the central limit theorem cannot be applied. This can arise from memory effects or long-range correlations in the system - for example when immobile obstacles are present. Anomalous diffusion also occurs if jump lengths or waiting times for the underlaying random walk are drawn from a broad distribution. Such fat-tailed distributions may lead to a diverging first moment of the waiting time probability distribution function and/or a diverging second moment of the jump length distribution. Therefore, a deviation from a Gaussian - which is characterized by finite first and second moments - arises (see Eq. (2.2) and Eq. (2.2)). In the remainder, we will restrict the discussion to subdiffusive motion.

Anomalous diffusion due to immobile obstacles

Particles that diffuse in a homogenous environment show normal diffusive behavior. However, when obstacles are present, i.e. the particles diffuse in a disordered media, subdiffusion can emerge. This is due to the fact that particles are slowed down as they pass through narrow holes or get trapped in bottle-necks of the surrounding medium.

A simple model to describe anomalous diffusion due to spatial disorder is diffusion in so-called percolation clusters. These percolation models can either be studied on lattices or in the continuum. In the case of lattice percolation models, a percolation cluster emerges when obstacles are randomly placed on the lattice to occupy either vertices or bonds (site percolation or bond percolation model). When two neighboring vertices or bonds are occupied, these obstacles are connected and form

part of the same cluster of obstacles. At a certain obstacle concentration C_c, one large cluster appears. This is called the percolation threshold. Below the percolation threshold, finite clusters exist. ξ is the typical size of holes and clusters for $C < C_c$ [12].

Percolation clusters may be considered to be random fractals. In general, a fractal is a geometric object that is self-similar. Fractals are described by their fractal dimension d_f, which measures the mass $M(r)$ of the cluster within a sphere of radius r [13].

$$M(r) \propto \begin{cases} r^2 & for \quad r > \xi \\ r^{d_f} & for \quad r < \xi \end{cases} \tag{2.5}$$

Interestingly, the path of a tracer performing a random walk is already an example of a fractal.
Particles diffusing in percolation clusters show an anomalous diffusion behavior. The times and distances over which anomalous behavior is seen depends on the obstacle concentration. For obstacle concentrations $C < C_p$, subdiffusion occurs for short time and length scales, for which the cluster is a fractal. Here, tracers are trapped in bottle-necks and dead-ends as described above. So, the direction of the steps of the random motion depends on the position of the tracer within the surrounding medium and hence the normal diffusion behavior is lost. For long times and lengths, the cluster is homogenous and normal diffusion is recovered. At the percolation threshold, the cluster is self-similar for all time and length scales, and anomalous diffusion persists asymptotically. For obstacle concentrations $C > C_p$, no long-range diffusion occurs, as particles are trapped in local lakes that are not connected to other parts of the environment. So, for $t \to \infty$ three cases emerge

$$\left\langle r(t)^2 \right\rangle \propto \begin{cases} t & for \quad C < C_p \\ t^\alpha & for \quad C = C_p \\ \xi(C)^2 & for \quad C > C_p \end{cases} \tag{2.6}$$

In general, anomalous diffusion due to obstacles has been extensively studied in Monte Carlo simulations on lattices with fixed obstacles [14–16]. The cross-over time τ_α and anomaly coefficient α depend on the obstacle concentration as well as on size and shape of tracers and obstacles. α in general decreases with increasing obstacle concentration to reach a limiting value at the percolation threshold. For continuum models of percolation clusters, the following limiting values of α have been found: For a two-dimensional percolation cluster, the anomaly index $\alpha \approx 0.697$ and for a 3-dimensional system $\alpha \approx 0.526$ [17]. The value $\alpha \approx 0.7$ for a 2-dimensional system thus represents a lower cut-off for observed anomalies which can be explained by obstruction [18].

Anomalous diffusion due to trapping

Subdiffusion can also arise in systems in which trapping or binding takes place. Diffusing particles bind to traps and get immobilized transiently. When only some traps with certain binding energies E_B are present, anomalous diffusion only exists for a certain time scale. As soon as particles are bound to all traps, i.e. the system is in equilibrium, normal diffusion reemerges. This cross-over time t_C increases, when the hierarchy of traps grows. When an infinite hierarchy of traps with increasing binding energies exists, anomalous diffusion is observed for all times [19].

As the cross-over time is reached when the tracers are in equilibrium with the traps, increasing concentration of traps leads to longer cross-over times t_C. The diffusion coefficient D for times $t > t_C$ is also influenced by the presence of traps and higher concentrations lead to a decrease of D.

The escape time from a trap is proportional to the Boltzmann factor $\exp(-\frac{E_B}{kT})$. Changing the binding energy E_B leads to a change in the escape time from a trap. Thus, an infinite hierarchy of binding energies for the traps leads to a fat-tailed distribution of binding times.

Mathematically, subdiffusion due to transient binding can be described by the Continuous Time Random Walk (CTRW). Here, the particles do not jump to a new position every Δt as it was assumed for normal diffusion, but the waiting times between two successive jumps are drawn from a suitable distribution function $w(t)$, the so-called waiting time probability density function. The first moment, the mean waiting time, is given by

$$\langle T_w \rangle = \int_0^\infty t w(t) dt \tag{2.7}$$

As long as the $\langle T_w \rangle$ is finite, normal diffusion occurs. However, for diverging $\langle T_w \rangle$, anomalous diffusion arises. Waiting time probability density function $w(t)$ with the asymptotic behaviour

$$w(t) \sim (\frac{\tau}{t})^{1-\alpha} \tag{2.8}$$

lead to anomalous diffusion with a mean square displacement $\sim t^\alpha$.

An interesting feature of the CTRW is the fact that it is non-ergodic, i.e. the time average and the ensemble average are not equal [20].

The CTRW scenario discussed above is only one of the possible CTRW scenarios. Anomalous diffusion, more precisely superdiffusion, occurs if the mean waiting time is finite, but instead the jump length variance diverges. More complicated scenarios have also been studied, where jump length and waiting times can no longer be treated as independent random variables [21].

Chapter 3

The endoplasmic reticulum and the secretory pathway

In this chapter biological background information on the studied problem is given. In particular, the secretory pathway, with a special focus on the endoplasmic reticulum (ER), is discussed. A review of studies on ER retention mechanisms and diffusional properties of proteins in the ER follows. Finally, the spatial relationship of some cellular organelles is described.

3.1 The cell

The cell is the smallest structural and functional unit of all known living organisms. Some organisms, such as most bacteria, are unicellular. Other organisms, such as humans, are multicellular.

A eukaryotic (animal) cell has a typical size of 5 to 30μm. The plasma membrane, a heterogeneous lipid bilayer, forms the outer boundary. The interior is filed with cytoplasm and well structured by membranes and protein filaments such as actin filaments or microtubules. These extend through the whole cell and stabilize its shape. With a diameter of about 5 to 15μm, the nucleus is the biggest compartment. It contains the DNA (deoxyribonucleic acid). Other membranous compartments of the cell are the endoplasmic reticulum (ER), the Golgi apparatus, lysosomes and mitochondria. The ER and the Golgi apparatus form part of the secretory pathway and will be described in detail in the next section. Lysosomes are very acid compartments that take care of waste disposal within the cell. Mitochondria are the power plants of the cell. A schematic picture of an animal cell is shown in Fig. 3.1.

In the nucleus transcription of DNA into messenger-ribonucleic acid (mRNA) takes

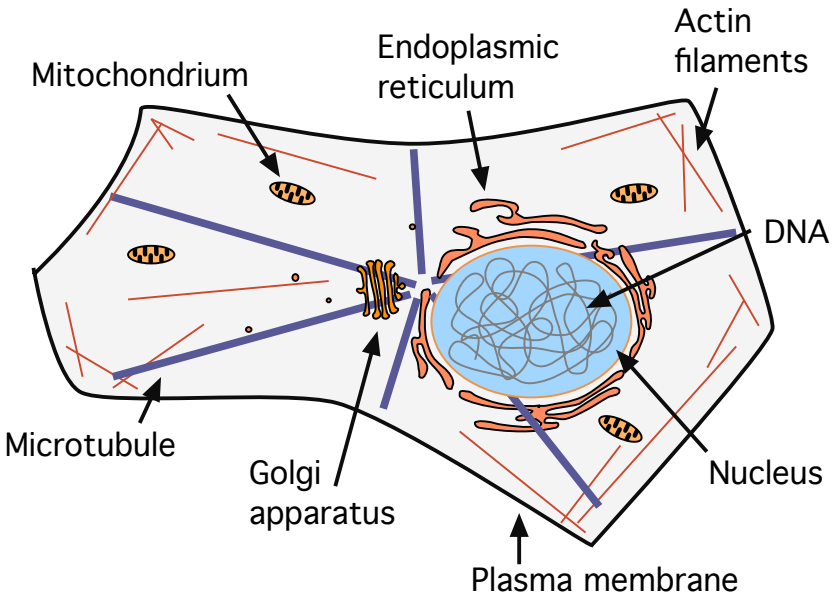

Figure 3.1: *Schematic picture of a eukaryotic cell. The cytoplasm filling the cell is separated from the extracellular space by the plasma membrane. The nucleus is the biggest compartment containing the DNA. Endoplasmic reticulum and Golgi apparatus form part of the secretory pathway, through which transport of membrane proteins and secretory proteins takes place. Microtubules and actin filaments are components of the cytoskeleton which stabilizes the cell. Mitochondria are the power plants of the cell.*

place. It serves as an intermediate step in the production of functional proteins. The mRNA strands are transported into the cytoplasm and bind to protein-rRNA complexes called ribosomes, where they are translated into proteins - the major class of functional biomolecules. Proteins are made of amino acids joined via peptide bonds. Most proteins have a globular (spherical) shape with a diameter of about 1 - 10nm. Each protein folds into a very specific three-dimensional configuration immediately after translation, sometimes assisted by chaperones, a special class of proteins that facilitates individual folding steps. The shape of a protein is essential for its proper functioning. The total concentration of macromolecules in the cytoplasm is about 50 to 400$\frac{mg}{ml}$. Thus, the cytoplasm is densely populated and subdiffusion due to macromolecular crowding may occur [1].

However, not all proteins are soluble. Some are attached to the various cellular membranes. They all possess a hydrophobic amino acid sequence or acylations that are inserted into the membrane. They enter the membranous system at the endoplasmic reticulum (ER), from where they are shuttled via the Golgi apparatus towards their final destination, e.g. the plasma membrane.

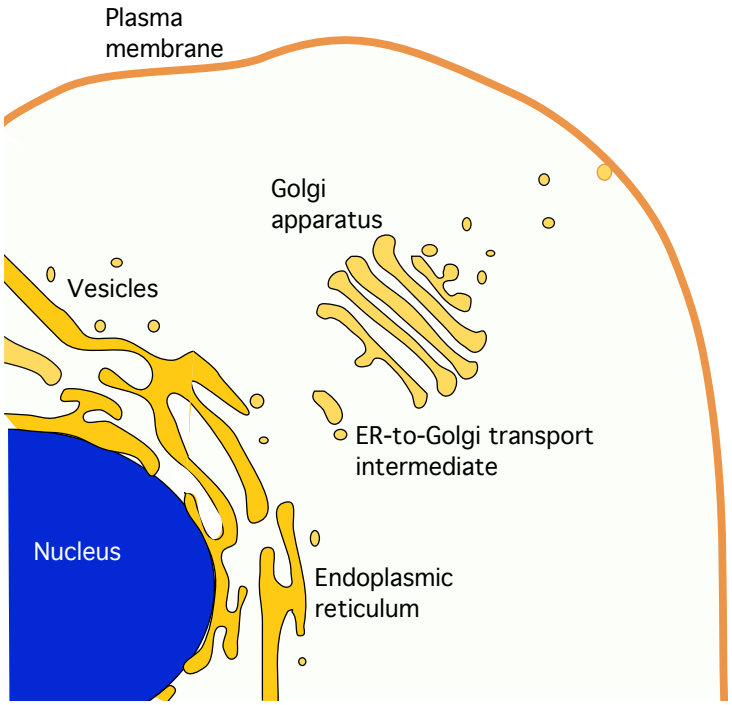

Figure 3.2: *The secretory pathway in mammalian cells. The endoplasmic reticulum forms a continuous membrane system including the nuclear envelope. It is the starting point of the secretory pathway. Here, proteins and lipids are packed in COPII-coated vesicles. On the way to the Golgi apparatus, vesicles fuse to form ER-to-Golgi transport intermediates (ERGIC). In the Golgi apparatus, proteins undergo modifications and are sorted into clathrin-coated vesicles. These are transported to the plasma membrane, with which they fuse, leaving their content either on the plasma membrane in the case of membrane-bound particles or secreting it into the extracellular space.*

3.2 The secretory pathway

In the first part of this thesis, the emphasize will be on the endoplasmic reticulum (ER). It forms part of the secretory pathway which consists of the ER, the Golgi apparatus, the plasma membrane and vesicular-tubular transport intermediates. Lipids, proteins and carbohydrates reach the exterior of the cell via this pathway. In a nutshell, proteins are translated and pre-processed in the ER, shuttled in COPII-coated vesicles towards the Golgi apparatus, where the are further modified and sorted into clathrin-coated vesicles (see Fig. 3.2). These finally fuse with the plasma membrane. This directional flow is balanced by retrograde pathways [22].

3.2.1 The ER is the starting point of the secretory pathway

The ER is the largest organelle of the secretory pathway and can be regarded as its starting point. The ER consists of interconnected membrane tubules and sheet-like structures, including the nuclear envelope, a double membrane that separates the cytoplasm from the nucleoplasm. The ER extends throughout most of the cytoplasm like a network and it interacts with cytoskeletal elements. It contains differentiated domains responsible for functions such as protein folding and assembly, lipid metabolism, detoxification, and intracellular calcium concentration regulation.

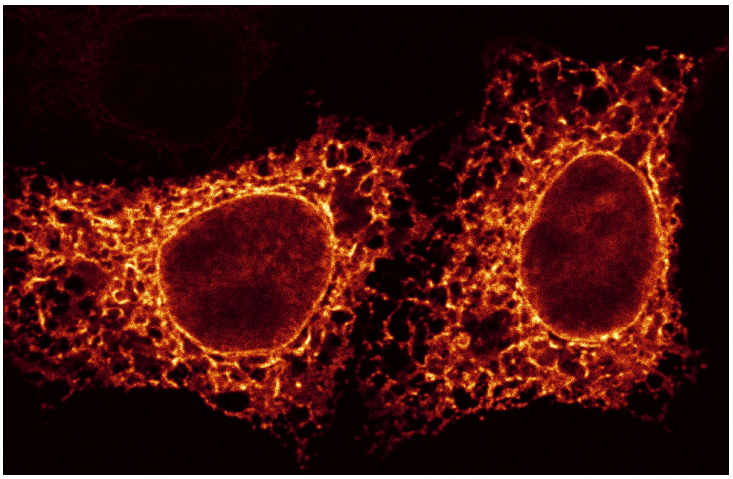

Figure 3.3: *Confocal image of calnexin-GFP, an ER-membrane protein expressed in HeLa wt cells. The nuclear envelope and the net-like structure of the ER are visible.*

Protein translation and insertion take place within the rough ER, the part of the ER to which ribosomes are attached on the cytosolic side. About 30% of all proteins enter the ER and undergo chaperone-assisted folding [23]. Other functions are taken care of in the smooth ER. Fluorescence loss in photobleaching (FLIP) studies [24] have shown that rough and smooth ER are interconnected and quickly exchange their protein contents. In most cell types (including HeLa cells, which are human cervical cancer cells used for parts of this study) rough and smooth parts are dispersed and do not form clearly segregated domains [25]. FRAP studies found GFP-tagged ER membrane proteins to be highly mobile, with diffusion coefficients from 0.2 to 0.5 $\frac{\mu m^2}{s}$ [6], which is close to the theoretical limit for protein diffusion in a bilayer [26].

Correctly folded secretory proteins are separated from ER resident proteins and sorted into so-called ER exit sites. These are special domains of about 1 - 2μm

in diameter that are scattered over the surface of the ER. Time-lapse imaging has revealed that ER exit sites are quite immobile and long-lived structures [27]. Here, budding of COPII-coated vesicles takes place [28]. The coat proteins that promote budding are recruited in several steps from the cytoplasm to the exit sites [29]. Folded proteins and lipids are transported in these vesicles, which then fuse with each other to form larger transport intermediates (vesicular-tubular clusters) that shuttle nascent proteins to the Golgi apparatus [30].

3.2.2 The Golgi apparatus is a polar organelle where protein sorting takes place

In most eukaryotic cells, the Golgi apparatus is made of flat cisternae that form one or several stacks. Its main functions are the processing of oligosaccharide side chains of proteins as well as sorting proteins for onward transport to different cellular locations. The Golgi apparatus is a polar organelle, e.g. new material fuses at the so-called *cis* face and old material leaves at the *trans* face. It is still a matter of debate, how this polarity is maintained and how material is shuttled through the Golgi apparatus [31, 32]. During mitosis, the Golgi apparatus breaks down at least partly and many Golgi-resident proteins fuse with ER membranes. At the onset of interphase, a new Golgi apparatus emerges. It remains unclear if a Golgi template is needed for this process or if the Golgi apparatus has the capability to form de novo [33]. Interestingly, Golgi apparatus phenotypes in plants, *Drosophila melanogaster* and yeast differ from the pile of flat cisternae observed in mammals. In plant cells, many dispersed mini-Golgi stacks exist, in yeast, cisternae are dispersed through the cytoplasm, and in the fruit fly, the Golgi apparatus is a disordered collection of transport vesicles [34, 35]. For the scope of this thesis, we are interested in the localization of the Golgi apparatus within the cell that will be discussed separately in Section 3.4.

3.3 ER protein assembly and export

Membrane and secretory proteins are post- or co-translationally inserted into the ER membrane, i.e. unfolded amino acid chains pass through large protein channels - the translocons - into the ER either after or during translation of the protein by a ribosome. In the ER, these proteins need to fold into their native configuration. As proper folding is essential for the functionality of proteins, various mechanisms are at work to ensure that the native configuration is reached or that misfolded proteins are destroyed before they can damage the cell. As the ER is the only part of the secretory pathway that has the ability to support folding, it is essential that no immature and dysfunctional proteins leave the ER [36].

3.3.1 The ER quality control mechanism ensures correct protein folding

In the ER, various chaperones exist in very high concentrations to facilitate folding and to recognize misfolded proteins. Chaperones interact with unfolded or partially folded proteins via exposed hydrophobic regions. Furthermore, they are able to stabilize correct folding intermediates and prevent aggregation. Misfolded proteins can be assisted in overcoming the energy barrier that separates them from the folded state.

During the folding process, proteins often bind sequentially to different chaperones. In the ER, chaperones of the well-know heat shock chaperone family are present. Additionally, lectins, chaperones specialized in folding glycoproteins, exist. Two prominent members of this family are the transmembrane protein calnexin (CNX) and its soluble counterpart calreticulin.

Indeed, the majority of the proteins that are translocated into the endoplasmic reticulum in eukaryotic cells are N-glycosylated and will thus interact with lectin chaperones. The glycosylation takes place during translocation. Glycans - oligosaccharides of composition $Glc_3Man_9GlcNAc_2$ (where Glc is glucose, Man is mannose and GlcNAc is N-acetylglucosamine) are attached as one core oligosaccharide to asparagine side-chains of growing polypeptides. Immediately thereafter, glucoses are trimmed by the sequential action of glucosidases I and II, which remove all but one glucose present in the original core glycan [37].

These monoglycosylated proteins can then interact with the two lectins - the soluble calreticulin and the membrane-bound calnexin. It the last glucose is also removed the binding to calnexin or calreticulin is inhibited and as a consequence some glycoproteins fail to fold or assemble efficiently [38]. The lectins are supposed to facilitate folding by binding the glycoproteins and presenting them to enzymes of the PDI family (protein disulfide isomerases). These induce disulfide bonds that stabilize the tertiary structure of proteins. Upon release of the substrate from calnexin or calreticulin, the last glucose residue is removed by glucosidase II. To increase the efficiency of this folding process, another enzyme, the glycosyltransferase UGT1 reglycosylates proteins that did not manage to fold correctly. This glucose residue acts as a tag for incompletely folded proteins. Hence, these proteins undergo another round of interaction with calnexin/calreticulin and get another chance to obtain their native configuration. This calnexin/calreticulin cycle is visualized in Fig. 3.4 [23, 39].

If the folding process fails completely, proteins are finally disposed. Degradation takes place by a process called ER-associated degradation (ERAD). Misfolded proteins are retranslocated to the cytoplasm via translocons, where an ubiquitin residue is attached to them. This ubiquitylation is the sign for degradation in the proteasomes - big RNA-protein complexes filled with degradation enzymes.

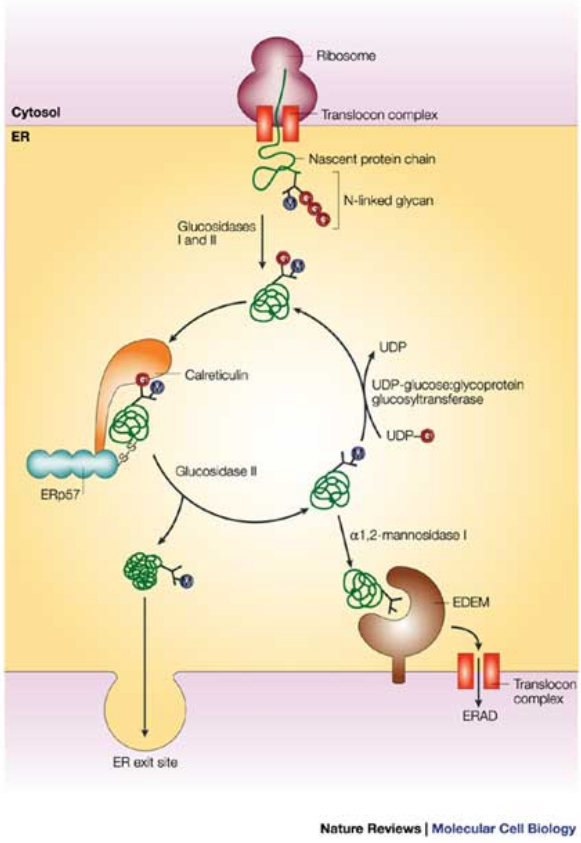

Figure 3.4: *The calnexin-calreticulin cycle. For simplicity, only calreticulin-assisted folding is shown. After attachment of the core oligosaccharide to the nascent protein chain, two glucoses are removed by glucosidase I and II. The monoglycosylated protein then interacts with calnexin or calreticulin. These chaperones are associated with thiol-disulphide oxidoreductase ERp57, which forms disulfide bonds during folding. Cleavage of the remaining glucose residue by glucosidase II releases the protein. Correctly folded proteins can then leave the ER. Others are recognized by UDP-glucose, reglycosylated and thus able to interact again with calnexin or calreticulin. If the protein is permanently misfolded, further modifications by mannosidase I lead to ER-associated degradation (ERAD) and export of the protein to the cytoplasm, where it is destroyed. Reprinted by permission from Macmillan Publishers Ltd: Nature Reviews Molecular Cell Biology [23], copyright 2003.*

Retention and degradation of misfolded proteins in the ER is the origin of several diseases, e.g. cystic fibrosis [40].

3.3.2 Misfolded proteins are retained in the ER

A partially still unsolved question is how misfolded proteins and ER-resident proteins are excluded from the ER export process.

For some soluble ER-resident proteins the mechanism of retrieval is known. They possess a common amino acid sequence, the so-called KDEL-sequence [41]. These proteins leave the ER, but a special receptor that cycles between Golgi apparatus and ER and recognizes the KDEL-sequence, captures escaped molecules and brings them back to the ER. Other retrieval sequences , e.g. KKXX, have also been identified [42, 43]. Nevertheless, there are also ER-resident proteins which never leave the ER.

Also many misfolded proteins never leave the ER, whereas the correctly folded counterparts are exported [6]. How exactly this segregation works is still a matter of debate. Several mechanisms have been suggested in the past:

1. unfolded proteins leave the ER, but interact with KDEL-tagged chaperones which bind to KDEL-retrieval receptors and are thus retrieved from post-ER compartments
2. export is receptor-mediated and thus only correctly folded proteins are recognized and exported
3. misfolded proteins are kept out of the ER exit sites either by a) aggregation of unfolded proteins, b) interaction with an ER-matrix or c) due to hydrophobic mismatch induced sorting mechanisms

The first model of retrieval clearly cannot be true for those proteins that never leave the ER.

In the past, the second model of receptor-mediated export has been popular for a long time. According to this model, many specialized export receptors for folded proteins were thought to exist. Without a proper receptor, no protein should be leaving the ER. However, exogenously expressed test proteins were transported correctly in host cells that do normally not contain the test protein. Therefore, these cells should also lack the specific export receptor for the test protein. On the other hand, many proteins - including VSV-G-GFP, a frequently used glycosylated cargo protein - possess binding sequences for COPII coat proteins. VSV-G-GFP has been shown to be actually concentrated 5- to 10-fold in ER exit sites during vesicle budding [44]. Thus, COPII might act here as a selective export receptor for folded proteins.

Another popular model is the bulk flow model [45]: According to this theory, proteins are non-selectively exported from the ER proportionally to their normal ER concentration. Different export rates can be explained by kinetics of folding and diffusion into the budding vesicles. Here, retention of unfolded proteins could be explained by the third model - keeping unfolded proteins out of the ER exit sites. In agreement with this, it has been shown that chaperones such as calnexin are largely excluded from ER exit sites [46]. The same as been observed for a VSVG mutant deprived of the acidic motif (which interacts with COPII) [47].

Exclusion from exit sites could be achieved by immobilizing misfolded proteins elsewhere in the ER, so that they simply cannot diffuse into the exit sites. This could in principle be achieved by binding to an immobile ER matrix or the formation of large aggregates. However, in the last years, there has been strong evidence against immobilization of unfolded proteins: folded and unfolded VSV-G has been shown to have similar mobilities in FRAP experiments. Additionally, many chaperones, including calnexin, are highly mobile within the ER and do by no means form an ER matrix [6, 48].

In principle, formation of (smaller) aggregates that are still mobile could lead to exclusion from budding vesicles by simple steric hindrance. Evidence for aggregate formation was found for temperature-sensitive tyrosinase, a tyrosinase mutant that (un)folds according to temperature. Here, different diffusional properties have been measured [49] depending on the folding status, in disagreement with the findings from FRAP measurement on VSVG mentioned above.

Not only steric hindrance but also hydrophobic mismatch could lead to exclusion from exit sites: Hydrophobic mismatch means that a protein with a certain length of hydrophobic transmembrane domain prefers staying in a membrane of similar thickness. If the lengths of the hydrophobic domain and the membrane differs, a mismatch occurs. If different membrane domains exist, this process can be used for sorting [50, 51]. Within the cell, the thickness of the membranes seems to increase from the ER, to the Golgi apparatus to the plasma membrane [52]. Indeed, it has also been experimentally shown that a fluorescent protein with a transmembrane domain of length 17 is retained in the ER, whereas the form with 22 hydrophobic amino acids is exported to the plasma membrane [53].

In summary, as of yet there is no single model capable of explaining the different findings about ER retention of unfolded proteins and their diffusional properties. In Chapter 5, we will revisit the problem of folding-dependent diffusion of VSVG.

3.4 Spatial organelle organization within cells

Within mammalian cells not only well defined compartments exist, but also their position is regulated. Important for the spatial arrangement of compartments is

the centrosome, which lies close to the cell center.

3.4.1 The centrosome is a microtubule-organizing center

The centrosome is composed of two centrioles and the pericentriolar material, a cloud of various microtubule binding proteins, γ-tubulin ring complexes and other proteins.

The centrioles are cylindrical microtubule structures. During interphase, e.g. the phase of the cell cycle were no cell division takes place, they organize the pericentriolar material. During mitosis, e.g. the cell division, the two centrioles move to opposite sites of the nucleus and form the spindle poles.

Very importantly, centrosomes act as microtubule organizing centers (MTOC). Microtubules nucleate at the γ-tubulin ring complexes that are contained in the pericentriolar material and grow to the cell periphery in a star-like manner ("aster"). In mitosis, each centriole acts as a separate MTOC, thus forming the bipolar mitotic spindle [54]. Microtubules emerging from these spindle poles capture the chromosomes that are then split into two halves and pulled towards the poles. Via this mechanism cells ensure that each daughter cell obtains a complete set of genetic information.

The centrosome usually locates close to the cell center. In vitro, a microtubule aster is sufficient to find the middle of a dish [55]. This is due to the fact that the stiff microtubules hit the boundary of the dish while growing and thus exert pushing forces on the MTOC and thereby centralize it. In vivo, several other factors such as interactions with the Golgi apparatus, the nucleus and actin filaments, cell-cell contacts, cell substratum or pulling forces generated by microtubule-associated proteins in the cell periphery might also influence the exact position of the centrosome [56–59].

3.4.2 The Golgi apparatus and the nucleus position close to the centrosome

In mammalian cells, ER-to-Golgi intermediate carriers are transported along microtubules towards the cell center. As the microtubules emanate from the centrosome, the Golgi material is concentrated in the proximity of the centrosome. Here, the stacks often fuse laterally to form one broad Golgi ribbon. However, this picture seems to be oversimplified as the pericentriolar position of the Golgi apparatus was also found to depend on Golgi-associated proteins and actin fibers present at the Golgi apparatus. Also some microtubules were found to nucleate

rather on the Golgi complex than on the centrosome. The exact mechanism of Golgi apparatus localization therefore still remains unknown [57]. In cell migration, the relative position of the Golgi apparatus, the centrosome and the leading edge were found to depend on the cell substratum [58].

Also the nucleus positions itself in the proximity of the centrosome. In mammalian cells, the nucleus is attached to the centrosome via a protein link. The linkage is very stable and survives cell lysis and nucleus extraction [60]. Forces are transferred via nuclear-envelope proteins to the nuclear lamina [61].

So far, it remains unknown, whether centrosome positions are influenced by nucleus positions or vice versa or whether the positioning might be even uncorrelated.

In the last chapter of this thesis, we address this question by studying the position of centrosome, Golgi apparatus and nucleus in cells of different geometries and symmetries. Computer simulations explaining the experimental data suggest that different forces act on nucleus and centrosome and the interplay leads to the final spatial arrangement.

Chapter 4

Fluorescence Correlation Spectroscopy

In this chapter details on fluorescence correlation spectroscopy are given. The experimental setup, the mathematical treatment of different scenarios and disturbing factors are discussed.

4.1 Introduction

Fluorescence correlation spectroscopy (FCS) was first introduced in the 1970s by Magde, Elson and Webb [62], but only became a valuable tool with the availability of confocal microscopy. It is a very sensitive confocal microscopy technique to study motion of fluorescent particles on short length and time scales. The basic principle of FCS is shown in Fig. 4.1. In contrast to other microscopy techniques, FCS does not rely on the average fluorescence intensity but rather exploits the fluorescence fluctuations. These fluctuations arise due to the motion of fluorescent molecules into and out of the confocal volume, due to e.g. diffusion. Thus, to measure a FCS curve, the focus of a confocal microscope is placed on the spot of interest in a cell and the fluorescence intensity F(t) is recorded over some time. This signal is temporally autocorrelated. The autocorrelation curve reflects the self-similarity of the fluorescence fluctuations over time and hence describes the temporal persistence of information. Its exact form depends on the underlying mechanism which caused the fluctuations in the first place.

In principle, all physical processes giving rise to fluorescence fluctuations can be quantified by the use of FCS [63]. Mostly, one is interested in the dynamic properties of mobile fluorescent particles. Here, the fluctuations are caused by fluorescent particles that enter or leave the focal volume. By quantitative analysis, different

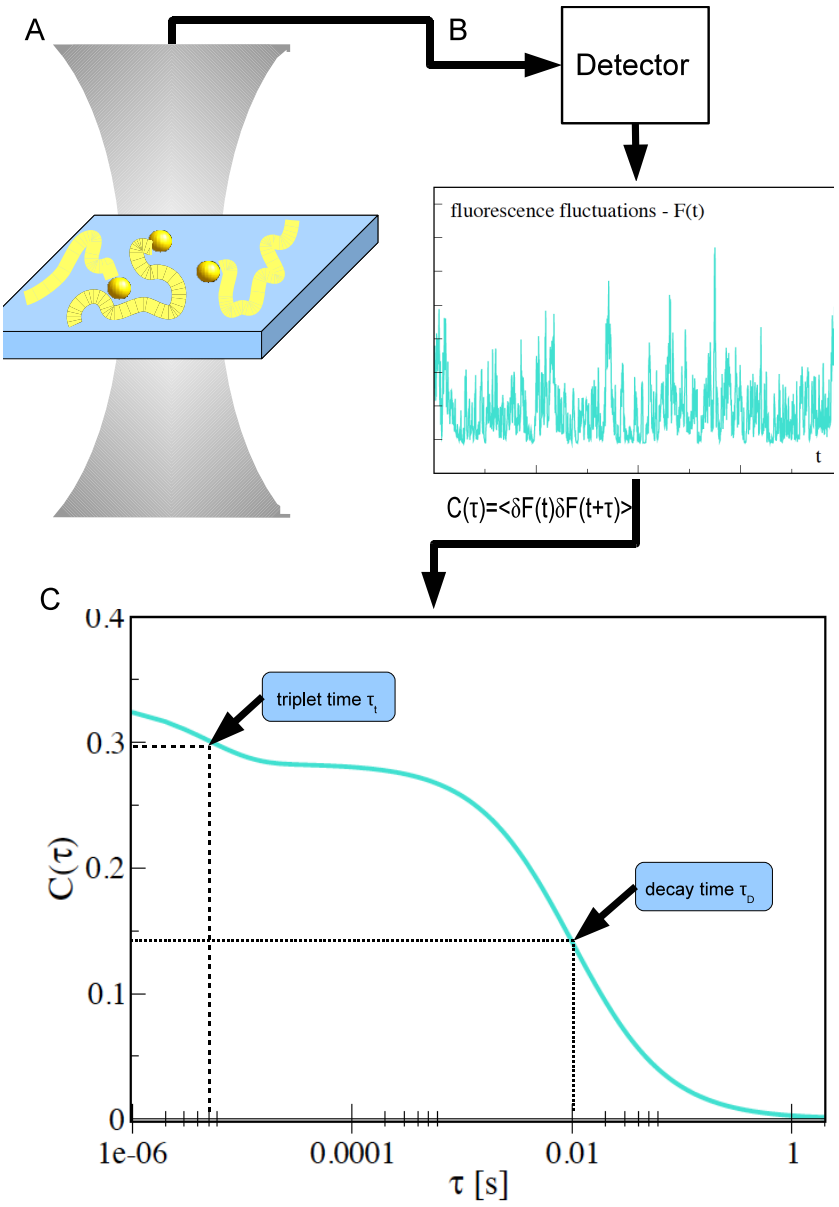

Figure 4.1: *Typical setup and course of an FCS experiment: Fluorescent particles move through the focal volume of a confocal microscope and emit photons. These are collected by a detector. The resulting intensity fluctuations are then autocorrelated. From the autocorrelation curve, typical times of experiment, such as triplet time of the fluorophore τ_t and the mean dwell time of the particles in the focal volume τ_D can be extracted.*

types of motion such as normal and anomalous diffusion or directed transport can be discriminated. FCS has been used to quantify a variety of parameters, such as translational and rotational diffusion coefficients [64], local particle concentrations or molecular interactions [65]. Via FCS one can also determine the number of fluorescent species in a sample. Using FCS, also anomalous diffusion has been observed in the cytosol due to molecular crowding [66] as well as for membrane proteins [9].

As the technique is based on the autocorrelation of fluctuations, it is crucial that the ratio of fluctuations to the total intensity is large in order to obtain a good signal-to-noise ratio. This can be achieved by monitoring only very few particles at a time. Therefore, very dilute samples with concentrations in the nanomolar range are typically used. Hence, FCS can be called an "on-average" single molecule technique. Additionally, one minimizes the detection volume by using a confocal microscope with a focal volume of about $1\mu m^3$. High photon yields per molecule increase the signal quality. Working with low particle concentration also has the benefit of avoiding artifacts due to unnaturally high expression levels of proteins.

Disturbing effects when analyzing FCS data arise from processes that cause additional fluctuations. Prominent examples are the photophysics of fluorophores, e.g. transitions into non-fluorescent triplet states, photobleaching or conformational changes.

4.2 Confocal setup, illumination and detection

4.2.1 Confocal setup

In general, confocal microscopes are used for FCS experiments, as they show a better axial resolution in comparison with bright field microscopes. The typical setup of a confocal microscope is illustrated in Fig. 4.2. It differs in two important factors from a bright field microscope. First, a collimated laser beam is used as a point excitation source. This source is confocal with the objective lens used for detection. Therefore, the in focus-signal is increased compared to the out-of focus signal. Second, a pinhole is placed in the image plane of the objective lens to further reduce out-of focus light [67]. Due to diffraction, the illuminated volume, the focal volume V_c, has a finite size. According to Abbe's resolution theorem the diameter of the focal volume is given by

$$\omega = \frac{\lambda}{2NA} \tag{4.1}$$

with λ being the illumination wavelength and $NA = n \sin \alpha$ the numerical aperture of the objective. Here, n is the refractive index of the immersion liquid and α is

half of the opening angle of the objective. In order to obtain a small focal volume, high NA values are desired. As the refractive index of biological probes resembles that of water, one typically uses water immersion objectives with $NA \geq 0.9$. As detectors one typically uses an avalanche photodiode, which converts the number of detected photons into an electrical signal. In the following paragraph, the mathematical treatment of the process illumination - fluorescence - detection is described following the approach of Rigler et al. [68].

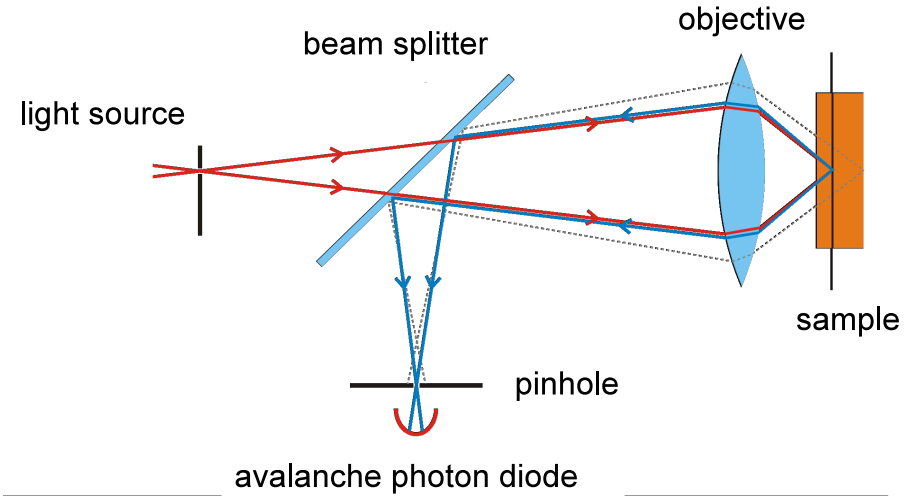

Figure 4.2: *Diagram of a confocal microscope: The point light source is confocal with the objective lens and a pinhole in the image plane further decreases out-of focus light.*

4.2.2 Illumination

The illumination profile of the laser beam depends on the laser, the objective and the refractive index of the sample. Perpendicular to the optical axis the cross section of a fundamental mode of a laser beam has a Gaussian profile. In the focal plane the width at $1/e^2$ intensity is $\omega_0 = \frac{\lambda}{n\pi \tan(\delta)}$, with δ being the focusing angle of the laser beam in the sample at $1/e^2$ intensity, n the refractive index of the sample, and λ the illumination wavelength in vacuum. For a focused beam, the width changes along the direction of propagation according to $\omega(z)^2 = \omega_0^2 + z^2 \tan(\delta)^2$, with z being the distance from the object plane along the optical axis. The intensity profile is Gaussian in the radial direction, and Lorentzian perpendicular to it:

$$I_{ill}(\vec{r}, z) = \frac{2P}{\pi\omega(z)^2} \exp\left\{-2\frac{\vec{r}^2}{\omega(z)^2}\right\} \tag{4.2}$$

where P is the power of the laser beam and r the radial coordinate in the sample space.

4.2.3 Detection

The emitted light is collected by the objective lens and transmitted through the pinhole onto the detector. Here the intensity is measured in terms of number of photons per unit time ("counts per second"). The detection characteristics of the objective-pinhole combination is described by the so-called collection efficiency function CEF. It describes the fraction of emitted light that is transmitted through the pinhole.

$$CEF(\vec{r}', z) = \frac{1}{\delta} \int T(\vec{r}) PSF(\vec{r}, \vec{r}', z) d\vec{r} \tag{4.3}$$

with $T(\vec{r})$ the transmission function of the pinhole and $PSF(\vec{r}, \vec{r}', z)$, the point spread function. The transmission function is given as the projection of the pinhole into the sample space:

$$T(\vec{r}) = circ\left\{\frac{\vec{r}}{s_0}\right\} \tag{4.4}$$

$$circ\left\{\frac{\vec{r}}{s_0}\right\} = \begin{cases} 1 & if \quad |r| \leq s_0 \\ 0 & else \end{cases} \tag{4.5}$$

where s_0 is the radius of the pinhole projected to the sample space. The PSF describes the image of a point source, located at $\vec{r}'$ in the sample, in the image plane. It can be approximated by a disk function centered at $\vec{r}'$

$$PSF(\vec{r}, \vec{r}', z) = \frac{circ\left\{\frac{(\vec{r}-\vec{r}')}{R(z)}\right\}}{\pi R(z)^2} \tag{4.6}$$

$$R(z)^2 = R_0^2 + z^2 \tan(\alpha)^2 \tag{4.7}$$

$R(z)$ is the radius of the image spot of a point source at a distance z from the focal plane, R_0 the resolution limit of the objective and α the aperture half-angle of the objective.

Multiplying the illumination profile $I(\vec{r}', z)$ with the collection efficiency function $CEF(\vec{r}', z)$ one obtains the so-called molecule detection efficiency $MDE(\vec{r}', z)$. This function describes the properties of the whole optical setup.

4.2.4 Illumination- fluorescence - detection

Overall one obtains the following expression for the emission characteristic of the microscope: $I_{em}(\vec{r}, z) = qeCEF(\vec{r}, \vec{r}', z) I_{ill}(\vec{r}; z)$, where q is the photon yield per

illumination intensity of a single fluorophore and e the detection efficiency of the detectors and filters. As Rigler et al. have shown [68], this function can be well approximated by a Gaussian profile in radial as well as in axial direction, as long as the radius and location of the pinhole is chosen appropriately. The condition for the pinhole radius projected to the sample space reads: $\omega_0 < s_0 < \frac{0.5\tan(\alpha)\omega_0}{\tan(\delta)}$.

The emission characteristic of the total setup thus becomes

$$I_{em}(x, y, z) = qeI_0 \exp\left\{\frac{-2(x^2+y^2)}{\omega_0^2} - \frac{2z^2}{(\omega_0 S)^2}\right\} \tag{4.8}$$

S is a dimensionless factor - the so called structure factor. It's typically in the range $S = 3 - 10$ and takes into account the relative elongation of the focal volume in axial direction compared to the lateral direction. This approximated Gaussian profile now renders it possible to derive analytical expressions for the autocorrelation curves obtained in FCS experiments.

4.3 FCS analysis

Next, we introduce the concept of autocorrelation analysis to extract physical information from the measured fluorescence signal. Some frequently used autocorrelation functions will be considered.

4.3.1 The autocorrelation function

In general, autocorrelation analysis is used to detect a possible self-similarity or periodic pattern in noisy data. The autocorrelation function of a variable $h(t)$ is defined as

$$C(\tau) = \langle h(t)h(t+\tau)\rangle = \lim_{T\to\infty}\frac{2}{T}\int_{-T}^{T} h(t)h(t+\tau)dt \tag{4.9}$$

The value of the autocorrelation function at time τ compares the value of h at each time point $t \in \{t_0, t_{max} - \tau\}$ to the value of h at $t + \tau$. It therefore is a measure for the persistence of information over the time period τ. For completely random numbers $h(t)$ the autocorrelation function $C(\tau)$ would equal zero.

In fluorescence correlation spectroscopy, it is the aim to extract information from the intensity fluctuations. The measured fluorescence signal $F(t)$ depends on the overall emitted intensity of a fluorophore at a certain position in the sample and the fluorophore concentration $n(\vec{r}, t)$.

$$F(t) = \int I_{em}(\vec{r})n(\vec{r}, t)d\vec{r} \tag{4.10}$$

The fluorescence signal $F(t)$ and the concentration $n(\vec{r}, t)$ can be split into a constant and a fluctuating term.

$$F(t) = \overline{F} + \delta F(t) \tag{4.11}$$

$$n(\vec{r}, t) = \overline{n} + \delta n(\vec{r}, t) \tag{4.12}$$

Assuming that the fluctuations have zero mean and are uncorrelated at different positions, one obtains with Eqs. (4.9) - (4.12) for the autocorrelation of the fluorescence

$$\begin{aligned} \langle F(t)F(t+\tau)\rangle &= (\overline{n}\int I(\vec{r})d\vec{r})^2 + \\ &\int\int I_{em}(\vec{r})I_{em}(\vec{r'})\left\langle \delta n(\vec{r}, t)\delta n(\vec{r'}, t+\tau)\right\rangle d\vec{r}d\vec{r'} \end{aligned} \tag{4.13}$$

The first term is a constant, namely $\langle F(t)^2\rangle$. The second term is the autocorrelation function of the fluctuations. Typically, one works with the normalized autocorrelation function that decays to zero for $t \to \infty$.

$$\begin{aligned} C(\tau) &= \frac{\langle \delta F(t)\delta F(t+\tau)\rangle}{\overline{F}^2} \\ &= \frac{\int\int I_{em}(\vec{r})I_{em}(\vec{r'})\left\langle \delta n(\vec{r}, t)\delta n(\vec{r'}, t+\tau)\right\rangle d\vec{r}d\vec{r'}}{\overline{F}^2} \end{aligned} \tag{4.14}$$

If the underlying process that causes the fluctuations in the density is Markovian, e.g. $\left\langle \delta n(\vec{r}, t)\delta n(\vec{r'}, t+\tau)\right\rangle = \left\langle \delta n(\vec{r}, 0)\delta n(\vec{r'}, \tau)\right\rangle$, the autocorrelation function is independent of the starting time.

4.3.2 One freely diffusing species

If the density fluctuations $\delta n(t)$ arise due to the diffusion of one species of particles, the propagator $\left\langle \delta n(\vec{r}, 0)\delta n(\vec{r'}, 0+\tau)\right\rangle$ can be obtained analytically from the diffusion equation 2.3. With the initial condition $\left\langle \delta n(\vec{r}, 0)\delta n(\vec{r'}, 0)\right\rangle = \overline{n}\delta(\vec{r} - \vec{r'})$ one calculates via Fourier transformation

$$\left\langle \delta n(\vec{r}, 0)\delta n(\vec{r'}, \tau)\right\rangle = \frac{\overline{n}\exp\left\{\frac{-|\vec{r}-\vec{r'}|^2}{4D\tau}\right\}}{(4\pi D\tau)^{\frac{3}{2}}} \tag{4.15}$$

Inserting this propagator (4.15) and the Gaussian emission profile (4.8) into Eq. (4.15), the x-component of the autocorrelation function is given by

$$C_x(\tau) = \frac{\overline{n}(qel_0)^2}{\overline{F}^2(4\pi D\tau)^{\frac{1}{2}}}\int\int \exp\left\{\frac{-(x-x')^2}{4D\tau}\right\}\exp\left\{\frac{-2(x^2+x'^2)}{\omega_0^2}\right\}dxdx' \tag{4.16}$$

After substituting $\sqrt{2}\alpha = \frac{x+x'}{\omega_0}$, $\sqrt{2}\beta = \frac{x-x'}{\omega_0}$ and solving the y- and z-component in an analogous way, the full autocorrelation function for free 3-dimensional diffusion reads

$$C(\tau) = \frac{1}{V_{eff}\ \overline{n}}\ \frac{1}{1+\frac{\tau}{\tau_d}}\ \frac{1}{\sqrt{1+\frac{\tau}{\tau_d S^2}}} \tag{4.17}$$

This is the decay curve that is expected for a FCS experiment for a single fluorescently-labeled species in water (see Fig. 4.3a).

From the derivation, the effective volume emerges as $V_{eff} = \pi^{\frac{3}{2}}\omega_0^2 z_0$, where z_0 is focal width in axial direction. V_{eff} multiplied by the average concentration just gives the average number of particles N within the focal volume. Hence, FCS can be used to measure concentrations, after having determined V_{eff} in a calibration measurement.

The value of the autocorrelation function for a given time lag τ will depend on the similarity of the shifted and unshifted fluorescence signals, $F(t)$ and $F(t+\tau)$. The autocorrelation curve reaches its maximum for $\tau \to 0$, since the fluorescence values at times t and t + τ converge to the same value. For intermediate lag times τ smaller than the typical residence time τ_D of a fluorophore in the focus, a positive correlation value is obtained since the fluorescence values $F(t)$ and $F(t+\tau)$ arise from the same set of fluorophores that only assumes different spatial configurations in the confocal volume. In the opposite limit, $\tau >> \tau_D$, the fluctuations are caused by completely different fluorophores. Thus, there is no correlation between the fluctuation values and consequently $C(\tau) = 0$. From the decay of $C(\tau)$ it is therefore possible to extract the particles' mean dwell time τ_D in the confocal volume. For normal diffusion, this is related to the diffusion coefficient D via $\tau_D = \omega_0^2/(4D)$, where ω_0 is the extension of the confocal volume. Hence, one can measure diffusion constants via FCS by extracting τ_D from a fit of expression (4.17) to the experimentally obtained curve. However, for absolute measurements, the dimensions of the focal volume have to be determined carefully. Typical values are: For the focal width $\omega_0 = 250nm$ and for the structure factor $S = 5$. A fluorescent dye such as Alexa488 shows a diffusion time of $\tau_D \approx 30\mu s$ in water, which corresponds to $D \approx 520\frac{\mu m^2}{s}$.

In the case of membrane proteins, the correlation function for two-dimensional diffusion perpendicular to the optical axis is of interest:

$$C(\tau) = \frac{1}{N}\ \frac{1}{1+\frac{\tau}{\tau_D}} \tag{4.18}$$

Lipids in a membrane have a diffusion time of $\tau_D \approx 2.5ms$ which yields a diffusion coefficient $D \approx 6(\frac{\mu m^2}{s})$ [69]. As membrane proteins are bigger than lipids, they show larger τ_D and hence smaller diffusion coefficients. Therefore, one expects diffusion coefficients $D < 6\frac{\mu m^2}{s}$ in FCS experiments on membrane proteins.

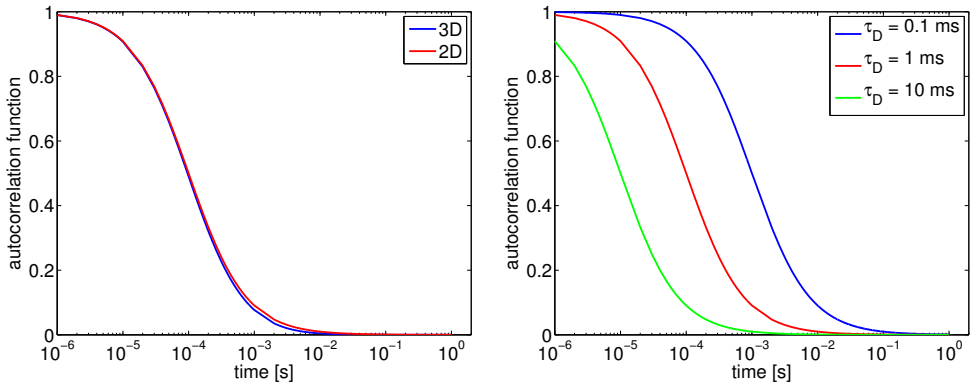

(a) (b)

Figure 4.3: *(a) Autocorrelation function for three-dimensional and two-dimensional diffusion with mean dwell time τ_D = 1ms. The two curves differ only for larger times, due to the influence of the elongation of the focal volume in z-direction. (b) Autocorrelation function for two-dimensional diffusion with diffusion times τ_D = 0.1ms, 1ms and 10ms respectively.*

4.3.3 Several diffusing species

For two freely diffusing species the autocorrelation curve is the sum of two terms with mean dwell times τ_{D1} and τ_{D2} and fractions f and $1-f$ respectively. For two-dimensional diffusion the autocorrelation curve is given by

$$C(\tau) = \frac{f}{N}\,\frac{1}{1+\frac{\tau}{\tau_{D1}}} + \frac{1-f}{N}\,\frac{1}{1+\frac{\tau}{\tau_{D2}}} \tag{4.19}$$

This can easily be extended to more than two species. However, for globular (spherical) proteins, a change in mass of the object by an order of magnitude only gives rise to a two-fold change in mobility - as the Einstein-Stokes relationship states that $D \propto 1/r$, where r is the radius of the protein and $m \propto r^3$. For membrane proteins, the Saffmann-Delbrück equation gives a dependence of the diffusion coefficient of $D \propto \log(1/r)$ [70]. Thus, only particles that differ sufficiently in size can be separated via FCS analysis. In Fig. 4.4a autocorrelations curves for two dimensional diffusion of two species with mean dwell times of 10ms and 100μs are shown.

4.3.4 Anomalous diffusion

In anomalous diffusion the mean square displacement grows as $(\Delta x)^2 = 4\Gamma\tau^\alpha$, with $\alpha < 1$ for subdiffusive motion and $\alpha = 1$ for normal diffusion. The transport

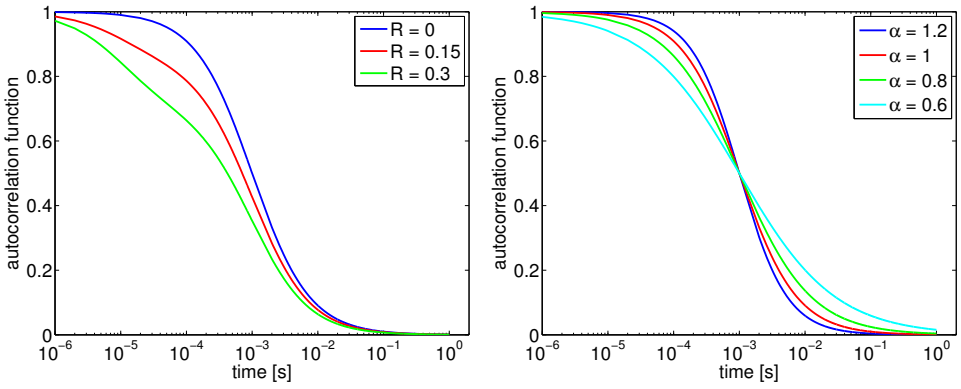

(a) (b)

Figure 4.4: *(a) Autocorrelation curve for a two-component system, with mean dwell times $\tau_{D1} = 10ms$ and $\tau_{D2} = 0.1ms$. R is the fraction of the fast component (b) autocorrelation curve for particles showing anomalous diffusion with different anomaly coefficients α. $\alpha = 1.2$ is a superdiffusive case, $\alpha = 1$ normal diffusive and $\alpha < 1$ subdiffusive. τ_D was chosen to be 1ms.*

coefficient Γ has the dimension of an area per fractional time ($\frac{\mu m^2}{s^\alpha}$). Independent of the physical reason for the anomaly, one can heuristically introduce a time-dependent diffusion coefficient $D(t) = \Gamma t^{\alpha-1}$. From a modified diffusion equation with the time dependent diffusion coefficient, one obtains an altered propagator for two-dimensional anomalous diffusion:

$$\left\langle \delta n(\vec{r}, 0)\delta n(\vec{r'}, \tau) \right\rangle = \frac{\exp\left\{\frac{-|\vec{r}-\vec{r'}|^2}{4\Gamma\tau^\alpha}\right\}}{4\Gamma\tau^\alpha} \tag{4.20}$$

Therefore, the autocorrelation function reads

$$C(\tau) = \frac{1}{N}\,\frac{1}{1+(\frac{\tau}{\tau_d})^\alpha} \tag{4.21}$$

Typical curves are shown in Fig. 4.4b.

This heuristic approach is problematic for $\tau \to 0$ and $\alpha < 1$ as $D \to \infty$. A mathematically sound expression was derived in the continuous time random walk (CTRW) model [21]. Nevertheless, it has been shown that fitting with the heuristic equation 4.21 yields good results even if the precise stochastic mechanism is a different one, since $C(\tau)$ only depends on the propagator's second moment [71, 72].

4.4 Experimental challenges and disturbing processes

In a real FCS experiment, one typically does not observe a pure diffusive process. Rather, the autocorrelation curve shows additional decay patterns resulting from the photophysics of the fluorophore, ongoing chemical reactions, or distortions of the optical setup and the detectors. Some of these effects can be accounted for in the analysis of the autocorrelation curve, others have to be avoided during the measurement.

4.4.1 Triplet correction

Many fluorophores used for FCS, e.g. the green fluorescent protein (GFP), switch between a bight and a dark state. The dark state, which emits no photons, has two effects: First, it reduces the apparent concentration of particles in the confocal volume. Second, when switching from the bright to the dark state while being in the focus, the fluorophore is no longer visible. It hence appears as if the fluorophore had left the focus. This effect gives rise to an additional fast decaying component in the fluctuations that is visible in the autocorrelation function at short lag times τ.

In more detail, this additional decay time corresponds to the lifetime of the metastable triplet state T_1 that represents a dark state since it can only decay radiationless. The electron transition from T_1 to the singlet ground state S_0 occurs in the order of μs and is thus accessible in a typical FCS experiment. In contrast, the radiative transition from the first exited singlet state S_1 happens within a few nanoseconds.

Mathematically, the temporal evolution of the occupation probabilities of the ground state S_0, the first exited singlet state S_1 and the triplet state T_1 can be described by a system of coupled differential equations [73]

$$\frac{d}{dt}\begin{pmatrix} S_0(t) \\ S_1(t) \\ T_1(t) \end{pmatrix} = \begin{pmatrix} -k_{12} & k_{21} & k_{31} \\ k_{12} & -k_{21}-k_{23} & 0 \\ 0 & k_{23} & -k_{31} \end{pmatrix} \begin{pmatrix} S_0(t) \\ S_1(t) \\ T_1(t) \end{pmatrix} \tag{4.22}$$

Only those fluorophores that have emitted a photon at time $t = 0$ and are in state S_0 (and can thus be excited again) contribute to the autocorrelation function. This leads to the initial condition

$$\frac{d}{dt}\begin{pmatrix} S_0(t) \\ S_1(t) \\ T_1(t) \end{pmatrix} = \begin{pmatrix} 1 \\ 0 \\ 0 \end{pmatrix} \tag{4.23}$$

The solution of the occupation probabilities $S(t)$ is of the form $S(t) = \sum_{i=1}^{3} c_i e^{\lambda_i t}$ where the λ_i and c_i are eigenvalues and eigenvectors of the transition matrix in Eq. 4.22. The important eigenvalue is

$$\lambda_3 = -k_{31} - \frac{k_{12}k_{23}}{k_{12} + k_{21}} = \frac{1}{\tau_T} \tag{4.24}$$

where τ_T is the lifetime of the triplet state. The occupation fraction of the triplet state in equilibrium is given by

$$f_T = \frac{k_{12}k_{23}}{k_{21}(k_{23} + k_{31}) + k_{31}(k_{21} + k_{23})} \tag{4.25}$$

The other eigenvalues correspond to the steady-state and a decay process in the time range of *ns*, which is not accessible with our FCS setup. This so-called photon anti-bunching causes the autocorrelation curve to drop to zero for $\tau \to 0$. It is due to the fact that for very small lag times the emission of a second photon from the same fluorophore cannot occur.

Considering that the triplet state dynamics is a statistically independant process from the diffusion of the tracers, one can separate it from the diffusive decay. Thus, the contributions of the triplet state and diffusion to the autocorrelation function are independent. It is therefore sufficient to multiply the diffusive autocorrelation function by the exponentially decaying triplet autocorrelation function:

$$C_{trip}(\tau) = (1 - f_T) + f_T e^{-\frac{\tau}{\tau_T}} \tag{4.26}$$

In Fig. 4.5a typical autocorrelation curves with a triplet fraction are plotted. As the triplet state dynamics take place in the μs regime, it can also easily be separated from the diffusive decay when fitting the data.

Similar exponentially decaying terms can also occur due to chemical modifications of the chromophore, such as protonation, or due to configurational changes that cause the fluorophore to switch between a bright and a dark state. This has been used to monitor pH-changes within cells with Green Fluorescent Protein [74]. Depending on the pH and the protonation state, GFP shows a very big triplet fraction of up to 80% with triplet times of up to 400 μs [75].

4.4.2 Background and scattered light

Some background light also reaches the detector and thus contributes to the measured fluorescence signal $F(t)$. It is generated by reflections of the laser light on the sample or the optical instruments and by scattering. As it is uncorrelated and typically possesses a different wavelength due to the Stokes shift, it does not contribute to the autocorrelation function. Nevertheless, the concentration of particles can be overestimated at high noise levels, as the autocorrelation curve is

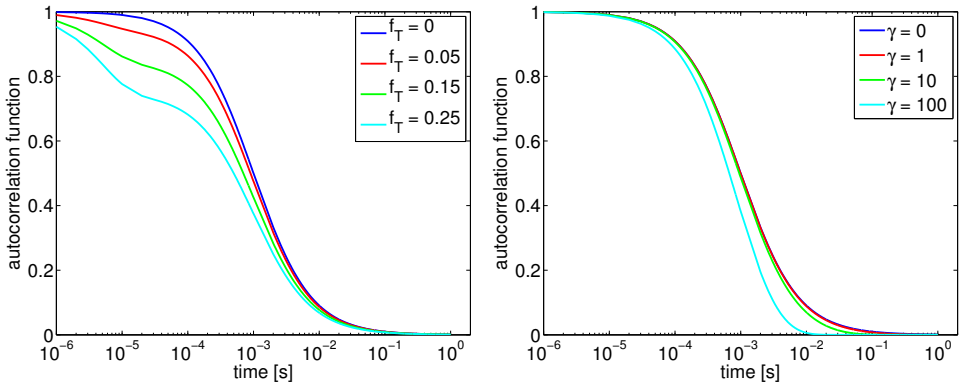

(a) (b)

Figure 4.5: *(a) Autocorrelation function with τ_D = 1 ms, τ_T =5 μs and different triplet fractions f_T (b) FCS curves with different bleaching rates γ and a diffusion time of 1 ms*

normalized to the average fluorescence. A correction factor can be applied in cases of high noise levels:

$$F_{background} = (1 - \frac{\bar{I}_{backgr}}{\bar{I}_{total}})^2 \tag{4.27}$$

Mostly, a good signal to noise ratio can be obtained by using appropriate filter systems and stable lasers. So the background correction can be avoided.

4.4.3 Detector afterpulsing

Another artifact arises from the properties of the detector - typically an avalanche photodiode that is able to count single photons. In about 1% of the detection events, a second electron avalanche is triggered by electrons remaining in the APD. The typical time range between the real photon event and this spuriously generated second event is some microseconds. Thus, there is an additional artificial correlation with a decay time of microseconds [76]. This has to be considered if one is interested in the triplet dynamics, whose typical time scales are similar. It does not affect measurements of diffusion times or anomaly coefficients.

4.4.4 Photobleaching

Fluorophores do possess a finite life time. They can undergo only a certain number of excitations and emissions before the molecule irreversibly changes into a non-fluorescent state. Mostly, these chemical changes take part when the fluorophore is in its triplet state T_1, which is especially reactive and possesses a long lifetime.

Typically, fluorophores can emit about 10^6 photons before getting bleached [77]. Photobleaching becomes important whenever fluorophores are illuminated long enough to reach this limit. This might happen in cells, as the same fluorophores can return several times into the focal volume due to the finite size of the total system. As the counts per molecule depend on the laser power, one needs to measure at low intensities. Typically, laser powers in the range of 10 to $100mW$ are used. Immobilization of molecules can also lead to an increase of bleaching. When measuring diffusion times, bleaching will lead to a shift towards smaller times. Once molecules are bleached they do not contribute to the signal anymore and it seems as if they had already left the focal volume.

Mathematically, photobleaching can be taken into account in the limit of small bleaching rates. If one assumes that photobleaching is an irreversible reaction with a rate γ proportional to the illumination intensity $I_{ill}(\vec{r})$, the concentration of functional fluorophores decreases according to

$$\left[\frac{\partial c(\vec{r},t)}{\partial t}\right]_{bleach} = -\gamma I_{ill}(\vec{r})c(\vec{r},t) \tag{4.28}$$

Using several approximations, an additional exponentially decaying factor appears in the autocorrelation function [78]. As the time-scales of the decays due to photobleaching and diffusion are similar, it cannot be separated in an experiment. Photobleaching thus leads to the estimated faster diffusion constants in FCS curves, as is shown in Fig. 4.5b. It therefore needs to be avoided by using small laser powers.

4.4.5 Deviations of the confocal volume from a three-dimensional Gaussian

Depending on the settings used during a FCS experiments, the approximation of the confocal volume as a three-dimensional Gaussian can lead to significant artifacts. So, apparent additional exponentially decaying components might appear or diffusion times might be overestimated. Deviations from a Gaussian can be limited by using a small confocal detector aperture and underfilling the objective back-aperture. However, this leads to a decrease in the signal to noise ratio in FCS experiments. Therefore, a trade-off has to be found [79]. When doing comparative measurements, it is especially important to always use the same settings.

Part II

Results: (Un)folded proteins in the ER

Chapter 5

Subdiffusion of misfolded proteins

In this chapter, we report on the mobility of folded versus unfolded proteins as quantified by FCS. The experimental results and a simulation model explaining the findings are presented.

5.1 Introduction

After translation virtually all transmembrane proteins, i.e. about 30% of the cell's proteome, enter the endoplasmic reticulum (ER) as unfolded polypeptide chains. Here, they undergo chaperone-assisted folding to their tertiary structure [80] and are subsequently packaged into COPII vesicles at distinct ER exit sites (ERES) [81]. Eventually, they are transported through the secretory pathway as described in Chapter 3.

An important and fundamental question in this sequence of events concerns the quality control in the ER, i.e. how do unfolded proteins know that they should reside in the ER rather than entering an emerging COPII vesicle? The mechanism by which this is achieved is still poorly understood and several models have been proposed to explain the phenomenon: Based on biochemical data it has been hypothesized that the abundant ER chaperones, e.g. calnexin, build extensive network-like structures in the ER that bind and immobilize unfolded proteins [82]. As a consequence, unfolded proteins would not be able to enter ERES and hence could not participate in a default anterograde bulk flow. However, the crucial aspect of this model, the immobilization of unfolded proteins, was challenged by the observation that the temperature-sensitive folding mutant VSVG ts045 (sometimes also referred to as tsO-45-G) of the vesicular stomatitis virus G protein was equally

mobile on ER membranes in the folded and unfolded state [83]. This result, derived via quantitative fluorescence recovery after photobleaching (FRAP) experiments, therefore supported the view of an active cargo selection and concentration into ERES [84] (see Section 3.3.2 for more details).

However, since diffusion on membranes only depends logarithmically on the size of the diffusing entity [85], the available FRAP data did not allow one to draw any conclusion if and to which extent unfolded proteins change their diffusion behavior due to complex formation with the ER's chaperone machinery. Indeed, a change in VSVG ts045's local diffusion properties not only is a signature of an interaction with chaperones but also may have a considerable impact on the frequency and success of interactions with other molecular co-factors [86].

To elucidate the diffusion properties of (un)folded VSVG ts045 and its chaperone calnexin under various conditions, we have utilized fluorescence correlation spectroscopy (FCS) and model simulations of size-dependent obstructed diffusion. Our experimental data clearly show a folding-dependent anomalous diffusion characteristics of VSVG ts045. The significantly stronger anomaly of the unfolded protein most likely reflects a transient oligomerization with the folding sensor UDP-glucose:glycoprotein glucosyl-transferase (UGT1). In contrast, enhancing the association with calnexin yielded a less anomalous diffusion behavior of unfolded VSVG ts045. Also, mobilizing the abundant translocon complexes of the ER softened the anomaly of unfolded VSVG ts045. Calnexin therefore 'solubilizes' larger clusters of unfolded VSVG ts045 to enhance its diffusion in an 'obstacle maze' of translocons, hence making the unfolded protein more accessible to interactions with other members of the quality control machinery.

5.2 Material and Methods

Cell Culture

HeLa cells were cultured in DMEM supplemented with 10% fetal calf serum, 1% L-glutamine, 1% non-essential amino acids (Invitrogen) and 1% penicillin and streptomycin. For microscopy cells were grown on glass coverslips in 12-well dishes or on Lab-Tek chambered coverglass (2-well, thickness #1; Nunc) overnight. Transfection with the GFP-tagged tsO45-G [87] was performed using FuGene6 (Roche) and the manufacturer's protocol (0.5μg DNA, 2μl FuGene6 in a total volume of 50μl supplement-free MEM). The same protocol was used for GFP-tagged GalNAc-T2 [88] and calnexin [89]. At the time of transfection, cells were about 40% to 60% confluent. Cells were incubated for 24h at the non-permissive temperature (39.5°C) and then taken to the microscope stage. Here, the temperature was either set to 39.5°C or 32°C. Cells were treated with 1mM castanospermine (CST), 100μg/ml cycloheximide (CHX), 100μM puromycin (PUR), or 5μg/ml Brefeldin A

TREATMENT	CONCENTRATION	TIME	FUNCTION
Brefeldin A	5μg/ml	1h	retains VSV-G in ER
Cyclohexamide	100μg/ml	1h	blocks translation
Castanospermine	1mM	1h	blocks chaperone interactions
Puromycin	100μM	10min	mobilizes translocons

Table 5.1: *Drug concentration and minimal time of treatment before measurement and effect of the drug*

(BFA) for the indicated times prior to performing microscopy (see table 5.1); the live imaging medium (MEM without phenol red + 25mM Hepes) also contained the drugs in the respective concentrations.

Microscopy and FCS

Imaging and fluorescence correlation spectroscopy (FCS) was performed with a Leica SP2-TCS confocal laser scanning microscope equipped with a water immersion objective (HCX PL APO 63x1.2W CORR) and an FCS-unit (Leica Microsystems, Mannheim, Germany). Samples were illuminated using the 488nm line of an Argon laser; fluorescence was detected using a bandpass filter (500-530nm). The pinhole was set to one Airy unit. Microscope and sample were kept at constant temperature by a climate chamber (Life Imaging Services, Switzerland).

Fluorescence time traces of 20s to 50s length were taken for autocorrelation analysis. Data that showed photobleaching or jumps in mean fluorescence was discarded. Such jumps can for example be caused by a drift of the laser beam relative to the sample or by large aggregates of fluorophores which enter or leave the focal volume. In these cases, FCS analysis would not yield reliable results. Autocorrelation was performed either directly with the software provided by the microscope manufacturer (Leica Mircosystems, Mannheim, Germany) or with a similar correlation routine. Both correlators produced the same results.

To reduce the influence of the local ER geometry, we collected FCS data on several loci within the same cell (see Fig. 5.3a) and on a large cell population. We did not observe systematic changes in the FCS curves between different loci and/or cells. FCS data were fitted with the appropriate mathematical expression for diffusion on a two-dimensional substrate [90]

$$C(\tau) = \frac{(1 + f_T \exp(-\tau/\tau_T))/N}{1 + (\tau/\tau_D)^\alpha} \ . \tag{5.1}$$

where α denotes the degree of anomaly of the diffusion while τ_D is the mean dwell time of a particle in the confocal volume. The mean number of particles in the confocal volume is denoted by N, whereas f_T denotes the fraction of fluorophores

in the triplet state having a lifetime τ_T (see Chapter 4 for a derivation of the formula and more details). For all measurements $1 < N < 20$. Fitting was done with the free software XMGRACE.

Due to the photophysics of the GFP variant attached to VSVG ts045, the triplet fraction and times were fairly high [91]. Still, the diffusive decay could be resolved unambiguously. All measurements were repeated on several days (no systematic variation), and only stable and unambiguous data were taken into account. We also note that a multi-component approach with different protein sizes and mobilities (e.g. monomers and trimers for VSVG) cannot explain the observed FCS curves as fitting with a normal diffusive, two-component autocorrelation formula yielded a mobility of the fast pool that was higher than that of a lipid (see also discussion in [90]).

Simulations

Monte Carlo simulations for obstructed diffusion were performed using a square lattice (200×200 sites, lattice constant $\Delta x = 5$nm) with periodic boundary conditions. Diffusive steps of 10-20 tracer particles were taken according to the blind ant algorithm, e.g. the jump direction was determined without considering whether the chosen site was occupied or not. If a chosen site was occupied, the tracer stayed at its position and did not move in this time increment. The parameters used were $\Delta t = 5\mu$s, diffusion coefficient $D_0 = 1\mu\text{m}^2/\text{s}$. To achieve a subdiffusive behavior, we randomly placed obstacles on 41% of the lattice sites. This value is near to the percolation threshold and thus yields a transient, yet long-lasting subdiffusion with an anomaly $\alpha > 0.7$ [92]. Obstacles were allowed to perform a random walk with diffusion constant D_{obst}.

Small tracers (mimicking, for example, protein monomers or dimers) occupied single lattice sites while large tracers (larger oligomers of proteins) occupied a square of four neighboring lattice sites (see Fig. 5.4). Due to the logarithmic dependence of the diffusion coefficient on the particle size in two dimensions [85], small and large particles were assumed to move with the same diffusion coefficient D_0. Before monitoring the diffusion for 10^6 time steps, the system was equilibrated for 10^6 time steps. The resulting mean square displacement (MSD) was fitted with a power law $\text{MSD} \sim t^\alpha$ to derive the anomaly exponent α. To access the influence of the measurement technique on the derived anomaly exponent α, α was additionally determined via the simulation of an FCS experiment for some data sets. To obtain FCS curves, we used the same setup as above for membrane, tracers and obstacles, but additionally simulated a confocal volume. The Gaussian confocal volume (width $\Delta x = \Delta y = 250nm$ and $\Delta z = 5\Delta x$) was placed in the center of the lattice and particles were assumed to contribute to the total fluorescence proportional to the Gaussian value on their lattice site. To avoid finite size effects, the lattice was chosen 14-fold larger than the confocal volume. Before data acquisition, 10^6

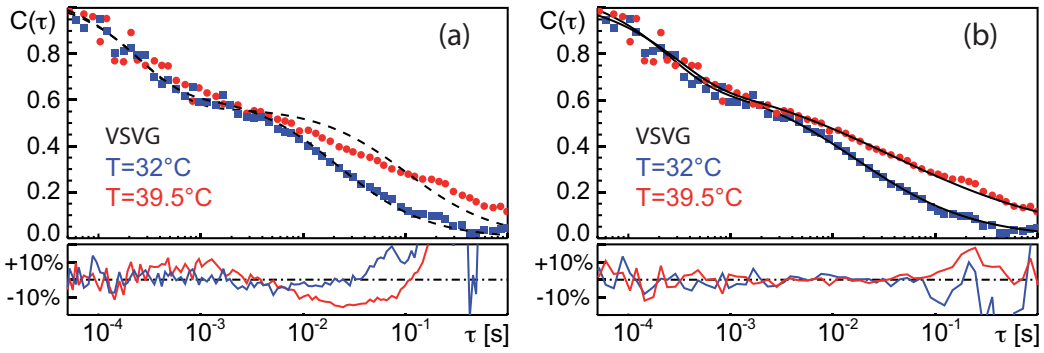

Figure 5.1: *(a) Representative FCS curves for VSVG ts045 in the ER in the unfolded (red circles) and folded (blue squares) state at 39.5° C and 32° C, respectively. Dashed black lines are fits according to Eq. 5.1 with the constraint $\alpha = 1$, i.e. normal diffusion. The residuals below the autocorrelation functions highlight the systematic deviations of these fits. (b) Same as before but full black lines represent fits according to equation 5.1 with $\alpha < 1$ as an open parameter. The residuals highlight the improved fit to the experimental data.*

equilibration steps were performed. Data sets corresponding to 20s of measurement were recorded, comparable to the experimental data acquisition time.

5.3 Results

Diffusion of VSVG ts045 depends on its folding status

To elucidate the diffusion properties of GFP-tagged VSVG ts045 in the endoplasmic reticulum (ER) of HeLa cells in the folded and unfolded state, we have used fluorescence correlation spectroscopy (FCS) at the permissive and non-permissive temperatures (32°C and 39.5°C, respectively). At both temperatures we applied Brefeldin A (BFA) which disrupts the Golgi apparatus and hence prevented a loss of VSVG ts045 from the ER at the permissive temperature [83]. In agreement with previous FRAP experiments [83], we observed that VSVG ts045 is mobile in the ER irrespective of its folding status. Yet, in contrast to the observations via FRAP, which had indicated a similar diffusive mobility for VSVG ts045 in the folded and unfolded state, we found qualitatively and quantitatively different diffusion behaviors in the two states (representative FCS curves are shown in Fig. 5.1). At both temperatures we observed anomalous instead of normal diffusion when using Eq. 5.1, i.e we found a nonlinear growth of the mean square displacement, $\mathsf{MSD} \sim t^{\alpha}$, with an anomaly exponent $\alpha < 1$ ($\alpha = 1$ for normal diffusion).

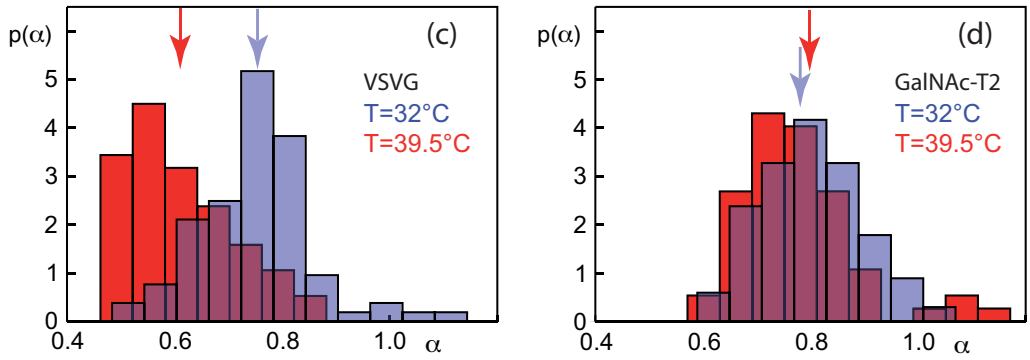

Figure 5.2: *(a) The distribution of anomalies, $p(\alpha)$ for VSVG shows a clear shift from low values in the unfolded state (red) towards larger values in the folded state at (light blue). Arrows highlight the mean of the distributions. (b) The distributions $p(\alpha)$ for GalNac-T2, a Golgi enzyme that was relocated to the ER by BFA treatment, did not show a significant variation after the temperature shift (red: 39.5° C; light blue: 32° C) highlighting the folding-specific behavior of VSVG ts045.*

Trying to fit $C(\tau)$ with an expression for normal diffusion resulted in systematic deviations of the fit curve from the experimental data (see residuals in Fig. 5.1a). Using a two-component fit with two normally diffusive pools consistently lead to diffusion coefficients of the faster pool that exceeded the mobility of single lipids on model membranes (see also similar discussion in [90]). We therefore relied on the usage of the anomalous diffusion model Eq. 5.1 that yielded considerably lower residuals (see Fig. 5.1b).

We observed that the anomaly was significantly stronger for the unfolded VSVG ts045, i.e. α was lower. In the past, subdiffusion has been observed frequently in cells [93, 90, 94–96] and its emergence reflects on how a protein interacts with its environment [97]. To obtain statistically meaningful results, we inspected the distribution of anomalies, $p(\alpha)$, and the associated arithmetic mean, $\langle\alpha\rangle$ in a larger cell population (Fig. 5.2a and table 5.2). In each cell, different loci were used for data acquisition (Fig. 5.3a) among which no systematic variation of α was detected.

We observed that both, $p(\alpha)$ and $\langle\alpha\rangle$, showed a significant shift towards smaller α for unfolded VSVG ts045 as compared to the folded form, while the associated mean residence times τ_D did not vary systematically (table 5.2). To confirm that the shift in the anomaly was due to folding and not a mere effect of temperature, we performed FCS measurements on GFP-tagged GalNAc-T2 [88], a Golgi-resident transmembrane enzyme that is folded at both temperatures. GalNAc-T2, relocated to the ER via BFA, showed no variation of the anomaly with temperature

		39.5°C	32°C
GalNAc-T2	α	0.80 ± 0.01	0.78 ± 0.02
	τ_D [ms]	9 ± 0.53	13 ± 0.88
	n	56	62
VSVG ts045	α	0.61 ± 0.01	0.75 ± 0.01
	τ_D [ms]	14 ± 0.76	18 ± 0.75
	n	63	87
VSVG ts045	α	0.70 ± 0.02	NA
(N336S)	τ_D [ms]	43 ± 4.87	NA
	n	33	NA

Table 5.2: *Summary of anomalies α and mean residence times τ_D and the corresponding standard deviations of the mean for the indicated proteins at the permissive and non-permissive temperature for VSVG ts045 folding. Testing the significance of the change in α when shifting to $32°C$ via a student's t-test yielded $p = 0.363$ (GalNAc-T2) and $p = 1.8 \times 10^{-14}$ (VSVG ts045).*

(Fig. 5.2b and table 5.2). Indeed, GalNAc-T2 showed a statistics $p(\alpha)$ that was similar to the folded VSVG ts045, highlighting a folding-independent background anomaly that may be due to molecular crowding on ER membranes (see Discussion). Thus, the folding of VSVG ts045 rather than the temperature shift itself is responsible for the observed changes in the diffusion behavior.

Interaction with the ER quality control determines the diffusion anomaly

We next aimed at elucidating the origin of the folding-specific subdiffusion of VSVG ts045. During their interaction with the quality control machinery of the ER, unfolded glycoproteins are known to interact with lectin chaperones like calnexin, glucosidase II (GlcII), and UDP-glucose:glycoprotein glucosyl-transferase (UGT1) via glucose residues on their glycans (see Fig. 5.3b for a sketch of the folding cycle and Chapter 3 for more details). To probe whether the increased anomaly for the unfolded VSVG ts045 was due to the interaction with GlcII, UGT1, or its chaperone calnexin (CNX) [98], we first impaired the folding cycle by blocking the action of GlcII via castanospermine (CST) [82] 1-2 hours prior to performing FCS measurements. Since treatment with CST prevents trimming of the terminal glucose, unfolded VSVG ts045 is well recognized by CNX and is hence not expected to exit the ER even after a shift to the folded state. Indeed, VSVG ts045 was retained in the ER even after shifting to the permissive temperature in the presence of CST (data not shown). However, FCS measurements on the

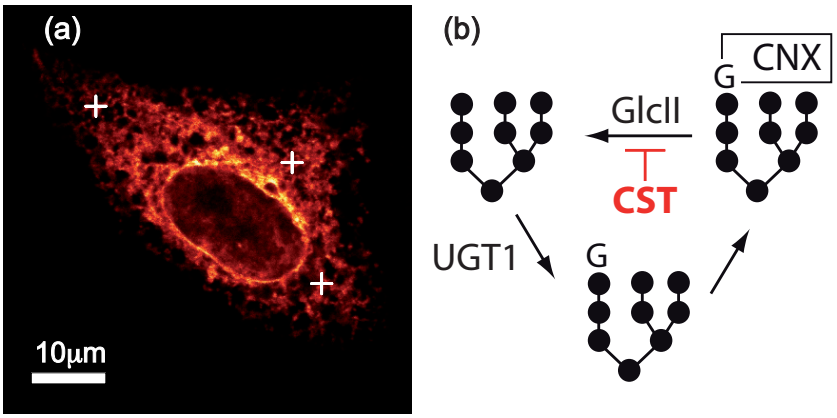

Figure 5.3: *(a) Representative image of a cell expressing VSVG ts045 at the non-permissive temperature. Three positions at which FCS experiments have been performed are highlighted by white crosses. (b) Graphical representation of the biochemically established quality control cycle for VSVG ts045. After trimming of the outermost glucose group by GlcII (which can be inhibited by CST), UGT1 tests the folding state and re-glycosylates the glycan of the unfolded protein. The mono-glycosylated state is then recognized by CNX. Since UGT1 has been reported to be a dimer, it may induce the formation of transient oligomers of unfolded proteins.*

unfolded protein in the presence of CST revealed a significant shift of the anomaly towards the value for folded VSVG ts045 (table 5.3) while GalNAc-T2 was not affected at any temperature (data not shown). The latter result is expected since GalNAc-T2 was relocated to the ER in its folded form and thus may not interact with the ER quality control. In addition, we observed a slight increase in the residence time τ_D for VSVG ts045. Hence, only if unfolded VSVG ts045 can interact with GlcII and/or UGT1 the folding state is reflected by the protein's anomalous diffusion behavior.

To test whether the strong subdiffusion of unfolded VSVG ts045 requires multiple glycans that interact with GlcII and/or UGT1, we utilized the mutant form VSVG ts045(N336S) [99] which lacks one of the two N-glycosylation sites. As a result, VSVG ts045(N336S) showed a significantly less pronounced anomalous diffusion (table 5.2) at the non-permissive temperature, indicating that at least two glycans are needed to induce a strongly anomalous diffusion.

We therefore hypothesized that a dynamic oligomerization of VSVG ts045 with GlcII and/or UGT1 is causal for the folding-specific value of the anomaly.

	39.5°C	32°C	39.5°C + CST	39.5°C + PUR
α	0.61 ± 0.01	0.75 ± 0.01	0.74 ± 0.01	0.74 ± 0.01
τ_D [ms]	14 ± 0.76	18 ± 0.75	30 ± 1.74	30 ± 3.16
n	63	87	56	40

Table 5.3: *Summary of anomalies α and mean residence times τ_D and the corresponding standard deviations of the mean for VSVG ts045 with the indicated treatment. Testing the significance of the anomalies in the respective columns via a student's t-test yielded $p_{13} = 1.3 \times 10^{-10}$, $p_{23} = 0.489$, $p_{14} = 1.1 \times 10^{-11}$, and $p_{24} = 0.488$.*

	39.5°C	32°C	39.5°C + CHX	39.5°C + CST
α	0.68 ± 0.02	0.69 ± 0.02	0.75 ± 0.02	0.73 ± 0.01
τ_D [ms]	28 ± 3.06	27 ± 2.08	21 ± 1.41	47 ± 3.49
n	18	28	18	21

Table 5.4: *Summary of anomalies α and mean residence times τ_D and the corresponding standard deviations of the mean for CNX with the indicated treatment. Testing the significance of the anomalies in the respective columns via a student's t-test yielded $p_{13} = 0.018$, $p_{23} = 0.061$, $p_{14} = 0.021$, and $p_{24} = 0.110$.*

Abundance of unfolded cargo determines the diffusion properties of calnexin in the ER

To test whether also the mobility of CNX is modulated by unfolded proteins, we performed FCS on a GFP-tagged calnexin [89]. This approach also allowed us to probe the hypothesis that chaperones form a network that may partially immobilize unfolded proteins in vivo [82]. Consistent with earlier reports [99], we observed that calnexin was very mobile in the ER at both temperatures with similar diffusion characteristics (see table 5.4), i.e. chaperones are unlikely to form an immobilizing network. The mean anomaly exponent for CNX, however, was lower than that observed for GalNAc-T2 and folded VSVG ts045. A significant increase of α was observed when reducing the amount of newly synthesized (unfolded) cargo by inhibiting protein synthesis via cycloheximide (CHX) [82] two hours prior to FCS measurements or when applying CST to avoid complex formation of unfolded proteins with UGT1 (table 5.4). This result suggests that CNX (transiently) associates with the subdiffusively moving (putative) oligomers made of unfolded VSVG ts045 and members of the ER quality control.

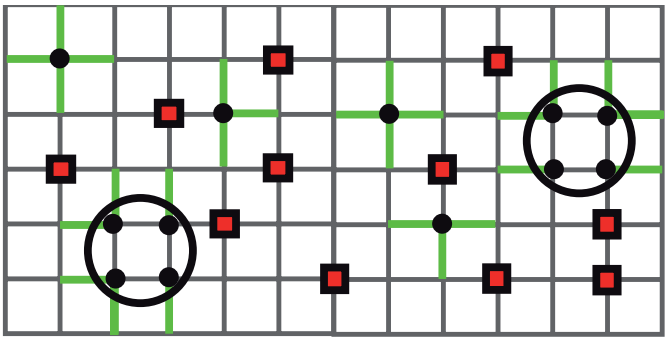

Figure 5.4: *Setup of the model for obstructed diffusion. Tracer particles (black circles) were allowed to move via diffusion (diffusion coefficient D_0) on a square lattice using a Monte Carlo scheme (cf. Methods). Small tracers occupied single lattice sites while large tracers were taken as tetramers (highlighted by an enclosing circle). Obstacles (red squares) occupied single lattice sites and were assigned a mobility $D_{\mathrm{obst}} \leq D_0$. When a next-neighbor lattice site was blocked, the tracer (or the moving obstacle) was not allowed to hop to this new position while hopping to free sites was allowed (highlighted as green paths).*

Obstructed diffusion explains the folding-dependent anomaly

To elaborate on the hypothesis that unfolded VSVG ts045 participates in the formation of larger oligomeric structures, we employed a simulation approach. While several mechanisms can give rise to anomalous diffusion behavior, the most likely scenario for the case considered here is obstructed diffusion. Previous studies have highlighted that diffusion in a maze of immobile obstacles can lead to anomalous diffusion on extended time scales even if the density of immobile obstacles is not yet at the critical percolation threshold [100]. Following this approach, we have tested whether anomalous diffusion can also arise when obstacles are mobile. To this end, we placed obstacles randomly on a two-dimensional square lattice (see Fig. 5.4) and allowed tracer particles to move with a diffusive mobility D_0 while obstacles moved with a diffusion coefficient $D_{\mathrm{obst}} \leq D_0$ (see Methods for details). We tested two methods for determining the anomaly coefficient α. One directly evaluates the particles' MSD whereas the other determines the anomaly from a fit to a simulated FCS curve (see Methods for details).

Fitting the mean square displacement (MSD) of the SPT data (see Fig. 5.5a) and using these parameters to calculate an analytical autocorrelation function yields a very good agreement with the numerically obtained FCS data (see Fig. 5.5b). Slight deviations for large time lags τ in the FCS curve indicate why SPT is the more favorable approach for us: To obtain a reasonable statistics of the

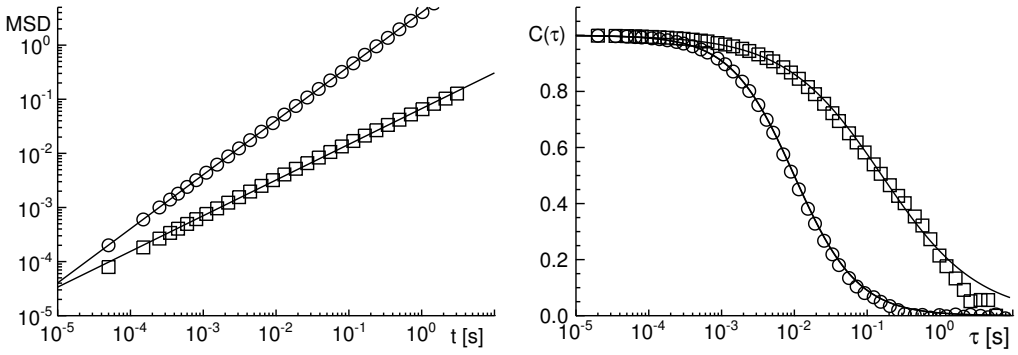

(a) (b)

Figure 5.5: *(a) Mean square displacement (MSD) in μm^2 for free diffusional motion (circles) and obstructed diffusion with fixed obstacles (squares). Full lines are best fits. (b) Using the results of the fits to the MSD as parameters for the autocorrelation function reveals an almost perfect agreement with the numerically obtained FCS curves (symbols as before). Thus, SPT and FCS yield the same information.*

autocorrelation function at times $\tau > 0.1$s, one needs to simulate the particle motion for more than 100s. Hence, the FCS simulation is computationally more expensive than analyzing SPT data but both yield the same information. We therefore used the SPT analysis for further evaluation. As anticipated, we observed a nonlinear growth of the MSD, $\langle r^2(t)\rangle \sim t^\alpha$, with the anomaly α depending on the size of the tracer and the mobility ratio D_{obst}/D_0 (Fig. 5.6). A suitable way to highlight the transient nature of the anomalous diffusion below the percolation threshold is a plot of $\langle r^2(t)\rangle/t$ which converges towards a constant for normal diffusion. Indeed, depending on the tracer size and the mobility of the obstacles, the cross-over towards the asymptotic normal diffusion occurred earlier or later. As expected, normal diffusion (i.e. $\alpha = 1$) was recovered on all time scales for fully mobile obstacles ($D_{\text{obst}}/D_0 \to 1$). For immobile obstacles ($D_{\text{obst}}/D_0 \to 0$) and small tracers (i.e. tracers and obstacles have the same size) the limiting anomaly $\alpha \approx 0.7$ for two-dimensional percolation [92, 100] emerged. In between these extreme cases the anomaly interpolated between the limiting values, when fitting the MSD in a reasonable range (highlighted by grey-shaded regions in Fig. 5.6). The values of α derived from fitting in this range are shown in Fig. 5.7 as a function of the obstacle mobility, D_{obst}/D_0.

When using larger tracer particles, i.e. a tetramer of small tracers, we observed that the dependency of the anomaly on the ratio D_{obst}/D_0 was considerably enhanced (Fig. 5.7): The value of α decreased stronger as compared to small tracers when obstacles became more and more immobile and the apparent anomaly ex-

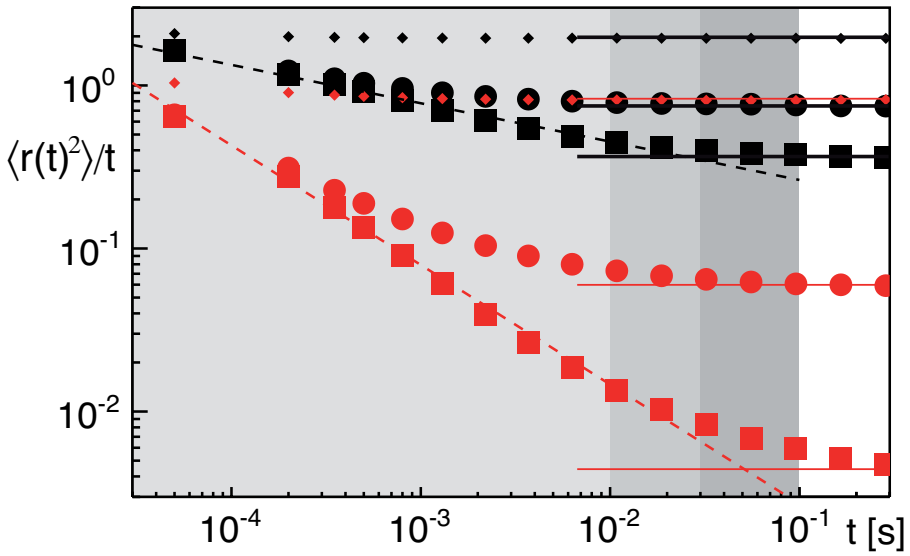

Figure 5.6: *Representative MSDs $\langle r^2(t)\rangle$ as obtained from simulations with small and large tracers (black and red symbols, respectively). Different mobilities of obstacles are denoted as small diamonds ($D_{obst}/D_0 = 1$), circles ($D_{obst}/D_0 = 0.02$), and squares ($D_{obst}/D_0 = 10^{-3}$). Dashed lines indicate the power-law decays $\langle r^2(t)/t \sim t^{\alpha-1}$ that emerge for $D_{obst}/D_0 \ll 1$ while full lines highlight the asymptotic normal diffusion, $\langle r^2(t)/t = \text{const}$. Grey shaded regions denote the range in which $\langle r^2(t)\rangle \sim t^{\alpha}$ was fitted to extract α. Here, $t < 0.03s$ yielded $\langle\alpha\rangle$, while the ranges $t < 0.01s$ and $t < 0.1s$ were used for determining the uncertainty of $\langle\alpha\rangle$.*

ponents become as low as $\alpha = 0.3$. It is worthwhile noting, however, that the MSD for terameric tracer particles is not a clear power law for very low ratios D_{obst}/D_0 but rather shows a transient kinetic arrest that mimics a power law only on average.

As a result of the simulations, we can state that obstructed diffusion (i) leads to anomalous diffusion even if the obstacles are (slowly) mobile, and (ii) that the same obstacle "maze" yields different anomalies for differently sized protein entities. These findings fit well to our experimental observations if we assume that VSVG ts045 is part of a higher-order structure in its unfolded but not in its folded form. While unobstructed diffusion in two dimension only depends logarithmically on the size of the diffusing entity [85] and hence does hardly allow one to determine the oligomeric status, obstacles act as a size-dependent sieve that highlights the oligomeric status. Folded VSVG ts045 proteins (which form homo-trimers [84])

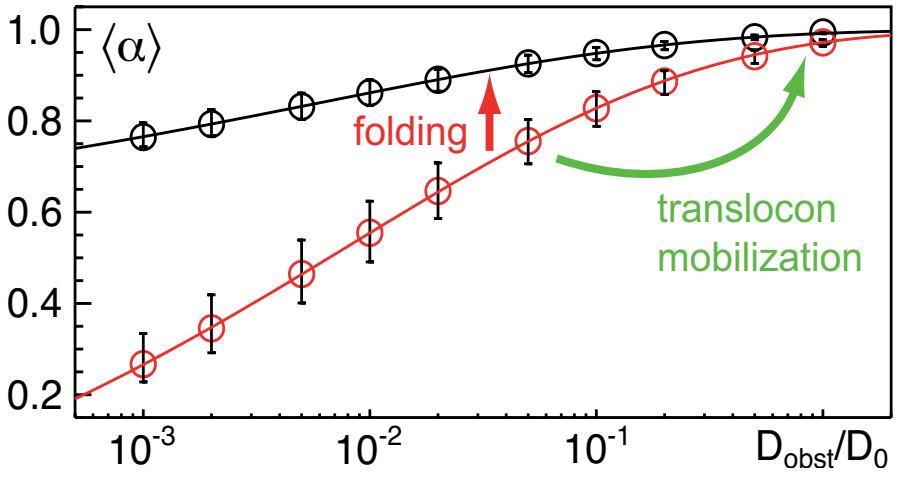

Figure 5.7: *The anomalies $\langle\alpha\rangle$ extracted from $\langle r^2(t)\rangle$ show a strong dependency on the relative mobility of obstacles, D_{obst}/D_0. Using a small tracer particle (black circles), the anomaly α is enhanced moderately when obstacles become more immobile. Using a large tracer (red circles) this dependency is much more pronounced. Error bars indicate the uncertainty associated with the fit range from which α was extracted (see above). Both, folding of VSVG ts045 (i.e. making the tracer smaller) and mobilizing obstacles shift α to larger values, in agreement with our experimental data (highlighted by arrows).*

are small entities (= small tracers) that should only feel a minor obstruction of the random walk, i.e. α is large. The unfolded protein, however, interacts repetitively with GlcII and UGT1, the latter of which has been reported to act as a dimer [101]. Using the two glycans of VSVG ts045, UGT1 may therefore support oligomer formation of the unfolded protein (= large tracers) with a concomitantly reduced value of α. Shifting to the permissive temperature leads to folding of VSVG ts045, the diffusing entity becomes smaller as an interaction with UGT1 does not occur any more, and consequently α rises (see Fig. 5.7). Alternatively, the oligomeric status can also be broken at the non-permissive temperature by applying CST (freezing the unfolded protein in a CNX-associated state that does not interact with UGT1) or by deleting one glycan of VSVG ts045 (N336S mutant). In either case, oligomerization of the unfolded protein is hampered, and thus α increases as observed experimentally. On the basis of this model we can also predict a new effect: Mobilizing obstacles without affecting the oligomeric status of VSVG ts045 should lead to a softening of the anomaly.

We hypothesized that the highly abundant and fairly immobile translocons, which mediate the translocation of polypeptide chains from ribosomes into the ER, may

constitute the diffusion obstacles. Indeed, releasing translocons from ribosomes by applying puromycin (PUR), i.e. enhancing the mobility of translocons [102], we observed a significant shift of the anomaly for unfolded VSVG ts045 while the folded form was not significantly affected (table 5.3). These data support our model predictions on a size-dependent anomalous diffusion with translocons acting as (slowly mobile) obstacles that obstruct the diffusion of (un)folded VSVG ts045 according to its effective oligomeric size.

5.4 Discussion

We have shown here that the diffusion characteristics of the model cargo VSVG ts045 in ER membranes significantly depends on its folding status. Blocking the interaction with GlcII or using a mutant form with only one glycan resulted in a diffusion behavior of the unfolded protein that was indistinguishable from the folded form. The same reduction of the anomaly was observed when the abundant translocons were mobilized. Together with our model simulations these data are consistent with the notion that unfolded VSVG ts045 and GlcII or UGT1 form larger complexes that show a strongly obstructed (and hence strongly anomalous) diffusion. Perturbing the formation of oligomers, e.g. by folding of VSVG ts045, adding CST, or using the N336S mutant yields smaller entities that are less obstructed in their diffusion and thus show a more normal diffusion behavior. Translocons therefore seem to act as size-selective diffusion obstacles that render the diffusion of unfolded VSVG ts045 more or less anomalous depending on its oligomeric status.

As shown above, two glycans were necessary to obtain a strongly anomalous diffusion, i.e. to induce oligomerization of the unfolded VSVG ts045. Together with the experimental finding that the folding sensor UGT1 acts in a dimeric form [101], this indicates that most likely UGT1, and not GlcII, is responsible for oligomerizing the unfolded VSVG ts045 to larger complexes. After glucose addition to the glycan via UGT1 and the subsequent binding of CNX (see Fig. 5.3b), the unfolded VSVG ts045 can leave the complex and diffuses on ER membranes as a smaller entity. CNX therefore would be crucial to dissolve larger complexes of unfolded proteins that are tethered via UGT1. While one could also envisage that unfolded VSVG ts045 forms simple aggregates, there is no reason why the N336S mutant with only a single glycan should not show such an aggregation. Moreover, its has been shown that VSVG ts045 cannot leave the ER anymore if it has started forming aggregates [103]. Rather the protein is then targeted to the ER degradation pathway. In our experiments we did observe, however, that VSVG ts045 was capable of reaching the plasma membrane upon shifting to the permissive temperature even after keeping cells at the non-permissive temperature over night.

Due to the hand-shaking cycle of GlcII, UGT1, and CNX (Fig. 5.3b) one may

expect CNX to also show a more pronounced anomalous diffusion while trying to liberate unfolded proteins from the complex with UGT1. In support of this expectation, we observed that the anomaly of GFP-tagged CNX in untreated cells was significantly lower than that observed for GalNAc-T2 and folded VSVG ts045 (table 5.4). A significant increase of α was observed, however, when reducing the amount of newly synthesized (unfolded) cargo.

Inspecting our anomaly exponents, a residual anomaly that is not due to the folding state is apparent. Even for folded VSVG ts045 or GalNAc-T2 we observed $\alpha < 0.8$. We attribute this "background" anomaly to the highly crowded state of ER membranes with a density of peripheral and transmembrane proteins that may well exceed $5 \times 10^4/\mu\mathrm{m}^2$ [104]. Indeed, it was shown earlier that crowding is intimately connected to anomalous diffusion in intracellular fluids [94, 96]. However, this anomaly-enhancing effect of crowding was not included in our simulations. As a consequence $\alpha \to 1$ for $D_{\mathrm{obst}} \to D_0$ is observed. A more quantitative comparison of our model and the experimental data would require to take into account also the crowding-induced anomaly. Still, the relative changes of α in our simplified simulations agree well with those observed in experiments, hence supporting our model.

At first glance, our results seem to be in conflict with previous reports on the diffusion of (un)folded VSVG ts045 obtained via FRAP [83]. It is worthwhile noting here, however, that FRAP tests the long-range diffusion of proteins while FCS is better suited to monitor the short-range diffusion properties on length and time scales below 1μm and 100ms. On these scales, the anomaly α is typically a more robust and meaningful measure for the diffusion properties as compared to the mean residence time τ_D in the FCS focus (see, e.g., [90] for a discussion). Indeed, the values for τ_D showed a fairly wide distribution for each condition which may be explained by the different geometries of the ER membrane that had been in the FCS focus. While these (unknown) geometrical constraints do not impose anomalous diffusion, they can considerably increase the variability of the residence time τ_D [90]. Nevertheless, in some cases a significant shift of τ_D emerged, e.g. for the mutant form of VSVG ts045 or when applying CST at the non-permissive temperature. This slowing down of the proteins' motion has been observed before [99], yet a molecular reason for it has remained elusive.

Finally, we would like to comment on the choice of the model of obstructed diffusion. While the model prediction was nicely confirmed by our experiments, one may still wonder whether alternative models could also explain the experimental data reported here. Alternative models are fractional Brownian motion (fBm), in which successive steps are correlated, and a continuous time random walk (CTRW), in which particles take power-law distributed rests between successive steps. Relating to the latter, it is worth noting that a simple binding event, i.e. a stochastic switching between a bound/slow and a free/fast state with Poissonian statistics cannot induce anomalous diffusion. The typical binding time

of such an event introduces only a single additional time scale into the problem while multiple time scales are needed for the emergence of a subdiffusive scaling of the MSD. These multiple time scales are introduced naturally by fBm, CTRW, or by restricting the diffusion in a self-similar maze of obstacles. Given that we were able to affect the diffusion behavior of VSVG ts045 by applying certain drugs or shifting to the folded state, it appears unlikely that fractional Gaussian noise (the thermal driving force for fBm) is the cause for the experimentally observed anomalous diffusion. Inspecting CTRW as a potential model, we have to note that this process has non-stationary increments and hence shows weak ergodicity breaking. As we did not observe any ageing between successively taken FCS curves and mobilizing potential obstacles (the translocons) gave experimental support for the obstruction model, we considered a CTRW to be the more unlikely model.

In conclusion, we have shown that transmembrane proteins like the model cargo VSVG ts045 show a folding-specific subdiffusion on ER membranes due to the interaction with the folding machinery. Counteracting the associated complex formation, CNX liberates unfolded proteins and dissolves the complexes, hence preventing the formation of immobile structures that potentially could poison the ER.

Chapter 6

ER retention of calnexin mutants

In this chapter, the retention mechanism of the chaperone calnexin in the ER is studied. A mutagenesis approach is taken: Several mutants with altered transmembrane domains are produced to test the effect of hydrophobic mismatch. Also mutants lacking whole domains are studied.

6.1 Introduction

As we have seen in the previous chapter, folded and unfolded proteins as well as chaperones are highly mobile in the endoplasmic reticulum. As described in more detail in Section 3.3.2, some ER-resident proteins are efficiently retrieved when having erroneously escaped the ER. These proteins possess a cytosolic KDEL binding motive by which they are recognized [41]. However, the majority of unfolded proteins never leaves the ER. The mechanism by which this is achieved is still poorly understood and several models have aimed at explaining this phenomenon [105]. Many are based on the idea that the association (either permanently or transiently) of unfolded proteins with chaperones is responsible for their retention. However, it is not even clear why the chaperones themselves are not exported.

One important ER chaperone that is involved in the quality control of proteins is the lectin calnexin that already played a role in the previous chapter. It is a highly abundant ER membrane protein that possesses a binding site for glycoproteins on the lumenal site. The lumenal part consists of a globular domain and an extended 140Å arm [106]. The cytosolic side contains a KDEL signal, which could be the origin of the ER retention of calnexin via retrieval.

Another important mechanism for localization of transmembrane proteins in cells

is the hydrophobic mismatch: If the length of the hydrophobic transmembrane (TM) domain of a protein is shorter or longer than the thickness of the embedding membrane, a mismatch occurs. Computer simulations have shown that proteins prefer the lipid environment which minimizes the hydrophobic mismatch [50]. Also in various experimental studies is has been observed that the length of the transmembrane domain can influence the localization of a protein within the secretory pathway [53, 107]. This can be explained by the fact that the membranes of the different organelles possess different thicknesses [108]. Therefore, the hydrophobic mismatch differs depending on the subcellular localization. In addition to the length of the TM domain, the hydrophobicity and charge of the amino acids composing the TM domain influences the engagement of the protein into the membrane [109].

To assess the importance of the various domains of CNX for its retention, we performed mutagenesis experiments on CNX-GFP [110].

6.2 Materials and methods

Cell culture

CNX-GFP [110] and all mutant forms were expressed in Hela wt cells. Transfection was done with FuGene 6 (Roche) as described in Section 5.2.

Protein mutagenesis

Mutagensis of the CNX-GFP plasmid was done with the Stratagene Quick Change kit (La Jolla, CA) and adequate primers. In more detail, first, two primers, i.e. DNA pieces of 25 to 45 bases, were designed. The primers can bind by base-pairing to the forward and reverse DNA strands in the region, where the mutation should be introduced. The two ends of each primer are designed to exactly match the original DNA sequence, but in the middle, the desired mutation is introduced. When designing the primers, some conditions need to be met, e.g. a guanine-cytosine content of at least 40% to achieve effective binding of the primers to the original DNA strands. Primers were ordered from Eurofins MWG Operon (Ebersberg). Using these primers and the original DNA, a polymerase chain reaction (PCR) is conducted.

In a PCR experiment, the enzyme DNA polymerase complements single stranded DNA with new nucleotides to produce new double-stranded DNA in vitro. As a starting point, a region of double-stranded DNA is needed. So, the mix of polymerase, nucleotides, primers and DNA template are heated to $\sim$ 95°C to dissolve the double-stranded DNA into two single-stranded DNAs. Upon cooling

to $\sim 60°C$, the primers bind to their target site. This is then the double-stranded starting point for the polymerase. Then the mixture is heated to $\sim 68°C$ and the polymerase doubles the number of DNA strands. This temperature cycle is repeated ~ 20 times. As the primers do not fit perfectly, but introduce a mutation, parts of the DNA is now in the mutated form. To extract only the mutated DNA, one uses the fact that the original DNA possesses chemical DNA modifications called methylations. Another enzyme is used to digest specifically the methylated DNA. Competent bacteria further multiply the DNA, a process called transformation (for details see the Stratagene Quick Change kit protocol). The bacteria are plated on agar plates containing the selection antibiotic that fits the used plasmid and colonies are grown. Some of these colonies then contain the desired mutations. Larger amount of DNA was then produced using the Quiagen Mini or Maxi kit and the standard protocol. The presence of the right mutation was checked by sequencing by the company GATC. For more details on the procedure, see Alberts et al. [54].

For the deletion of the KDEL retention signal, we used the primer 5'-AAC AGA TCA CCA AGA AAC GGG ATC CAC CGG-3' and the original CNX-GFP plasmid. For the mutagenesis of the TM domain, the following primers were used: To produce the mutant R1: 5'-CGT GGC TGT GGG TAG TCG CCA TTC TAA CTG TAG CCC TTC C-3' ; for the mutant R2: 5'-GGG TAG TCT ATA TTC TAG CCG TAG CCC TTC CTG TGT TCC-3'; for the mutant F: 5'-CCG TGG CTG TGG GTA GTC GCG ATT CTA GCG GTA GCC CTT CCT GTG TTC C-3'; for the mutant I1: 5'-CTG TGT TCC TGG TTA TCC TCG TAG CAA TCT TCT GCT GTT CTG GAA AG-3'; 5'-GTG TTC CTG GTT ATC CTC GTT ATC CTC TTC TGC TGT TCT GGA-3'; for the mutant XY: 5'-GT GTT CCTG GTT TGC TGT TCT GGA AAG AAA CAG ACC-3' on the CNX-Mut4 (without KDEL retrieval sequence) template. The same primer than for XY but on the E1 template was used for mutant XX. E1 was also taken as template for I2 with the primer 5'-GTG TTC CTG GTT ATC CTC GTA ATC TTC TGC TGT TCT GGA AAG-3' as well as for mutant 1 with the same primer than for mutant A. For E1, we used R1 as a template and the primer 5'-GGG TAG TCG CCA TTC TAG TCG TAG CCC TTG TCG TGT TCC TGG TTA TCC -3'. Mutant D1 was done by using A as a template and the primer 5'-GGT AGT CTA TAT TCT AAC TGC CAT CGT AGC CCT TCC TGT GTT CC-3'.

Deletion of protein domains

To remove a whole domain, one cuts out the DNA piece coding for the domain and reconnects the ends of the plasmid. To cut the DNA, DNA cutting enzymes are used. Each of these enzymes specifically recognizes a certain pattern of 4-5 base pairs. To achieve a single cut in the DNA, it is important that the cutting site is only present once in the whole plasmid. After the cutting, the two pieces

of DNA are separated via gel electrophoresis and the piece of interest is extracted from the gel using a gel extraction kit (Quiagen). The ends of the DNA piece are ligated, i.e. joined together with an enzyme to produce a new functional plasmid. The plasmid was checked by sequencing to exclude any errors. In praxis, it is not always straight forward to find appropriate cutting enzymes, so some tricks have to be applied.

To remove the luminal part, CNX-GFP was cut with Nhe1 and Blp1. This also removes the ER signal peptide, which had to be introduced again. The signal peptide is a short sequence that is responsible for ER localization of the newly synthesized protein. Thus, we inserted $\approx$ 80 nucleotide oligomers that contained the signal peptide sequence into the cut vector. The oligomers were ordered at MWG and contained compatible sites to Nhe1 and Blp1 cut ends.

To delete the cytosolic part, we cut out a large piece of the CNX template and put back in a piece of DNA that contained much of the cut-away sequence but not the part coding for the cytosolic part. In this way, the part of the DNA coding for the GFP, which is attached to the cytosolic part, was preserved. To obtain the piece of DNA that needs to be put back in, we performed a PCR on the CNX wt template with the following two primers: TGT ATG TTC TGG TGT TGG AAC TGC TAT TGT TGA GG and ATG GCA TGG ATC CCA CTG GTC TGT TTC TTT CC. For the PCR we used the pfusion enzyme from Finnzymes and the following PCR mix (pipetted in a cold PCR tube block): $10\mu l$ PCR 5x Buffer, $2\mu l$ dNTP mix, $1\mu l$ DNA template from a $10ng/\mu l$ solution, $1\mu l$ of each primer at a concentration of $100ng/\mu l$, $1,5\mu l$ DMSO, $33,5\mu l$ water and $1\mu l$ pfusion enzyme. We used the following PCR program: 30s at 98C followed by 35 cycles of 10s at 98°C, 30°C at 60°C and 40s at 72°C and a final step of 10 min at 72°C. The PCR amplifies a $\approx$1200 bp part of CNX, starting at the Hind1 cutting site and introducing a new BamH1 cutting site shortly after the transmembrane domain in the cytosolic part of CNX. Cutting the original vector and the PCR product with

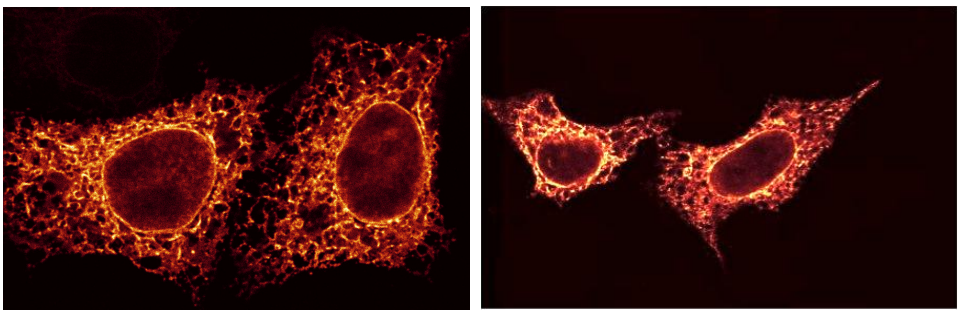

Figure 6.1: *Confocal images: (a)wt CNX-eGFP expressed in HeLa cells (b)CNX-Mut4-eGFP expressed in HeLa cells. This mutant lacks the KDEL retrieval sequence. Both proteins locate to the ER.*

BamH1 and Hind1 and ligating the PCR product into the vector thus produces the desired shortened mutant.

To replace eGFP by the non-dimerizing mGFP, we cut a mGFP-N2 Clonetech vector and the CNX-eGFP with Not1 and BamH1 and inserted the mGFP into the calnexin vector.

6.3 Results

Deletion of the ER retention signal

The ER retrieval signal in CNX is located in the extracellular part. We deleted the retention signal (RKPRRE) as described above. HeLa cells were transfected with wt and mutant DNA. In confocal fluorescence images, a clear ER staining was visible, thus the mutant showed the same localization as wt CNX (see Fig. 6.1).

Influence of the transmembrane domain

The transmembrane domain of CNX consists of 21 amino acids (WLWVVYILT-VALPVFLVILFC). It contains three hydrophilic amino acids (Y,T,P) that come to lie directly on top of each other in the secondary structure (an α-helix). We performed several mutations to shorten/extend the transmembrane domain and/or to eliminate the hydrophilic amino acids within it (see Table 6.1). All mutants additionally had the ER retention signal removed so that no retrieval would take place and export from the ER becomes visible.

In confocal images none of the mutants seemed to be exported from the ER. Also after 3h, 6h and 24h of cyclohexamide (CHX) treatment, which blocks the synthesis of new proteins, no other location was seen. In some cases, the protein located more to the sheet like regions of the ER. In Fig. 6.2 representative confocal images of some of the mutants after 3h of CHX treatment are shown.

On two mutants, we also performed FCS measurements. We chose mutant A having three extra amino acids in the transmembrane domain and mutant R2, which has one of the hydrophilic amino acids replaced by a hydrophobic one. For both cases, the mean anomaly coefficient was slightly shifted towards higher values as compared to the wildtype protein. We treated the cells with CHX to block synthesis of new proteins and therefore deprive the cells of unfolded proteins, the binding partner of CNX. Here, all three protein variants showed fairly similar values (see Table 6.2). We note that the observed distributions of the anomaly

NAME	CHANGE OF LENGTH OF TM	CHANGE OF AA
R1	-	1 (Y→ A)
R2	-	1 (T → A)
F	-	2 (T→ A, Y → A
E1	-	3 (Y→ P, V → A, T → A)
I1	+3 aa (+ VAI after VIL)	-
A	+ 3 aa (+ VIL after VIL)	-
I2	+ 2 aa (+ VI after VIL)	3 (Y → P, V → A, T→ A)
1	+3 aa (+ VIL after VIL)	3 (Y → P, V → A, T → A)
D	+ 5 aa (+ VIL after VIL, + AI after LTV)	-
XY	- 3 aa (- ILF)	-
XX	- 3 aa (- ILF)	3 (Y→ P, V → A, T → A)

Table 6.1: *The introduced mutations in the wild type calnexin. The net change in lengths of the transmembrane domain and the amico acids exchanged are given. Additionally, the KDEL ER retrieval signal was always removed.*

		without treatment	> 3h CHX
CNX-A	α	0.73 ± 0.03	0.75 ± 0.03
(37° C)	τ_D [ms]	36 ± 5	18 ± 2
	n	12	12
CNX-R2	α	0.71 ± 0.03	0.73 ± 0.03
(37° C)	τ_D [ms]	39 ± 4	15 ± 1
	n	14	12
CNX-wt	α	0.69 ± 0.02	0.75 ± 0.01
(32° C)	τ_D [ms]	27 ± 2	21 ± 1
	n	28	21

Table 6.2: *Summary of anomalies α and mean residence times τ_D and the corresponding standard deviations of the mean for the indicated CNX mutants without treatment and after treating with CHX for at least 3h to block new protein synthesis.*

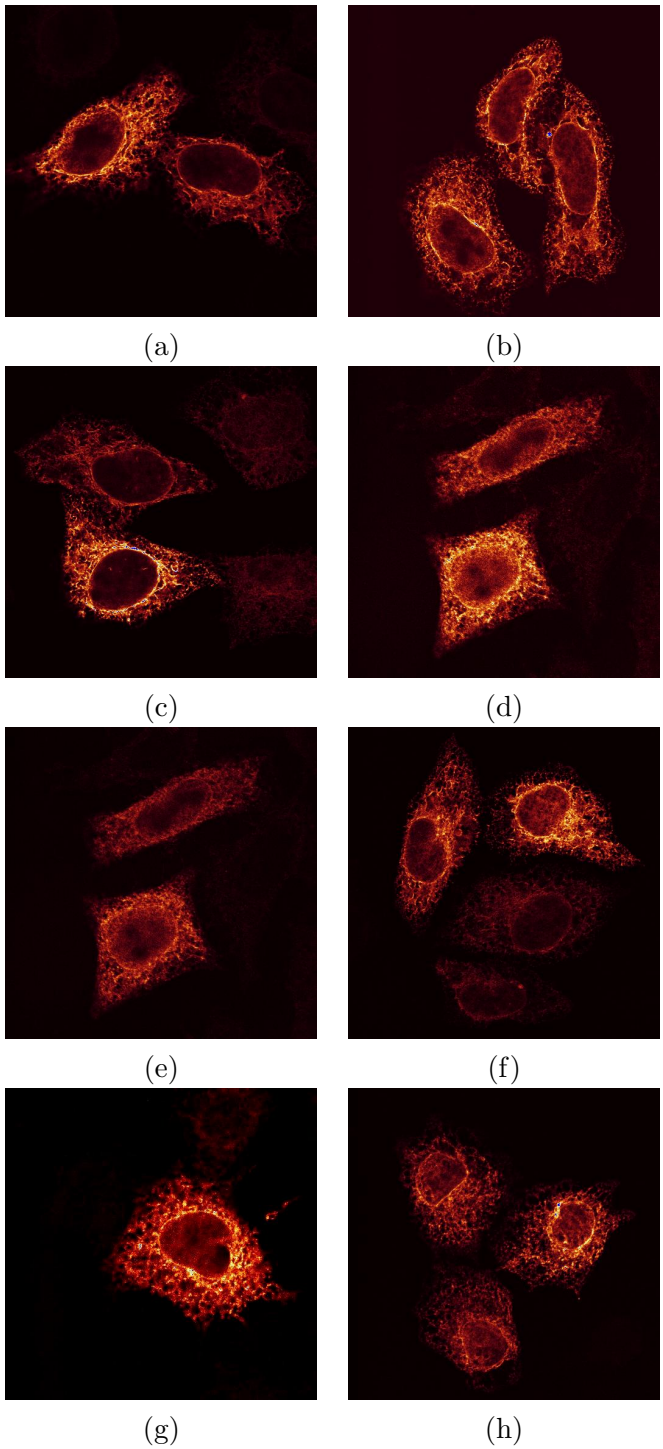

Figure 6.2: *Confocal images of the transmembrane mutants (a)-(f): after 3h of CHX treatment, (g)-(h) without any treatment; (a) mutant A, (b) mutant D1, (c) mutant E1, (d) mutant I1, (e) mutant R1, (f) mutant R2, (g) mutant XY, (h) mutant XX*

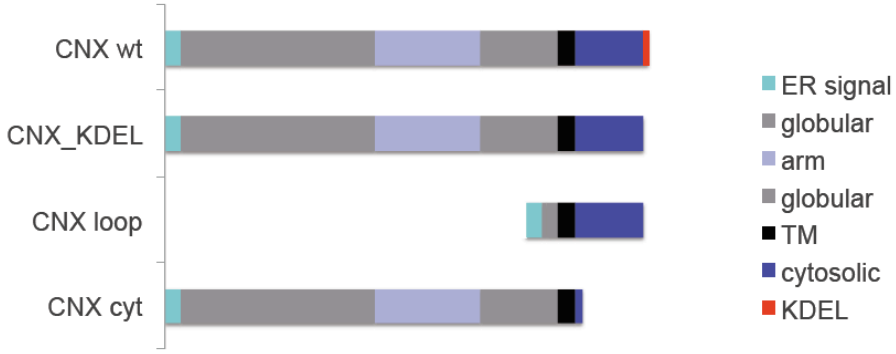

Figure 6.3: *Overview of the deletion mutants produced in this study.*

coefficient (and with it the deviation of the mean) are less well defined than for the wildtype protein.

The slight changes in presence of unfolded proteins could in principle be explained with a reduced functionality of the mutants. As we did not want to start functional testing of the mutants, we refrained from doing further experiments. In summary, we could not see any striking phenotype for the CNX mutants with different TM domain. Neither the localization nor the mobility data showed significant effects.

Deletion of whole domains

As the TM domain did not influence the localization, we next assessed the role of the luminal and cytosolic domain.

Wildtype calnexin consists of a signal peptide, a ER lumenal part, a transmembrane domain and a cytosolic part which includes a KDEL retrieval signal. The GFP is attached to the cytosolic part of the protein. We produced several mutants lacking whole domains. An overview is given in Fig. 6.3.

Deletion of the luminal part of CNX

The luminal part of CNX consists of a globular domain and a loop domain that extends far into the ER [111]. The size of this domain is further increased by another ER enzyme, the disulfide isomerase ERp57 that binds to the loop. Hence, it could hinder the engagement of CNX into COPII vesicles by steric repulsion. We therefore removed the loop domain.

After transfection, this CNXloop mutant showed an ER staining with additional big bright spots (mostly 3-4 per cell). The spots did not coincidence with the

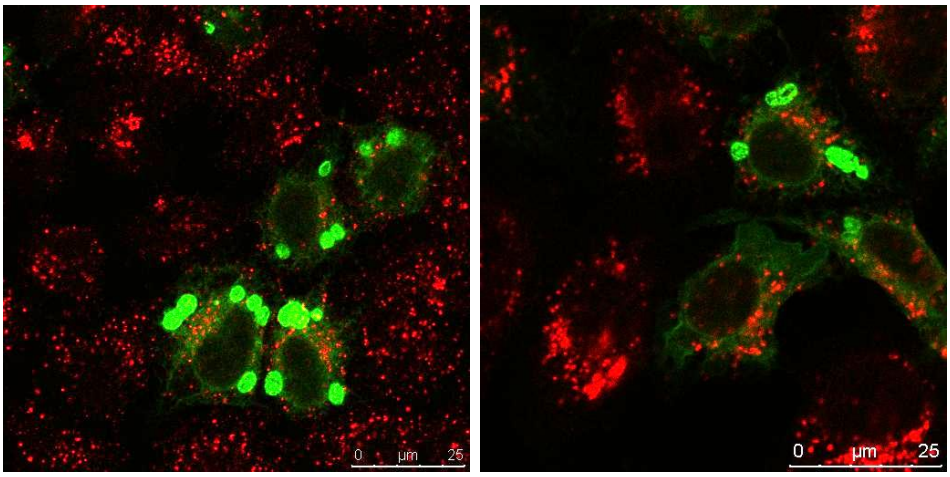

Figure 6.4: *Confocal images: (a)CNX-loop-GFP (green) was transfected and endosomes were stained with EEA1 marker (red) (b)CNX-loop-GFP (green) was transfected and lysosomes were stained with lamp2 marker (red). In both cases, the bright green spots were larger and showed no co-localization.*

lysosome marker lamp2 nor with the early endosome marker eea1 (see Fig. 6.4) in an immunofluorescence experiment. The spots mainly occurred in bright cells - hinting at an aggregation effect.

When performing FRAP experiments and bleaching a complete bright spot (no pinhole), it recovered within the time scale of 10min (85% after 7min). When only half of a bright spot was bleached, the exchange via diffusion from the unbleached part to the bleached part took part within 5-30s. Similar results were observed by Snapp et al. [112]. They concluded that the bright spots are organized smooth ER (OSER) structures that are formed due to dimerization of the cytosolic part of membrane proteins since the attached eGFP has a tendency to dimerize. For the wt CNX-eGFP, we also very occasionally found some bright spots.

We replaced the eGFP by a slightly different fluorophore, the mGFP fluorophore which has the same spectral properties but no tendency to dimerize. As expected, we hardly saw any bright spots in cells expressing CNX-loop-mGFP, hence confirming our above reasoning.

Therefore, one can conclude that the bright spots are aggregates of calnexin-GFP in the ER that are caused by the tendency of eGFP to dimerize. The calnexin mutant lacking the large loop domain has a higher tendency to form these aggregates. This could be due to less steric repulsion between calnexin-loop mutants as compared to calnexin wt. However, its ER localization was preserved.

Next, we removed the entire cytosolic part of CNX (starting from amino acid 511

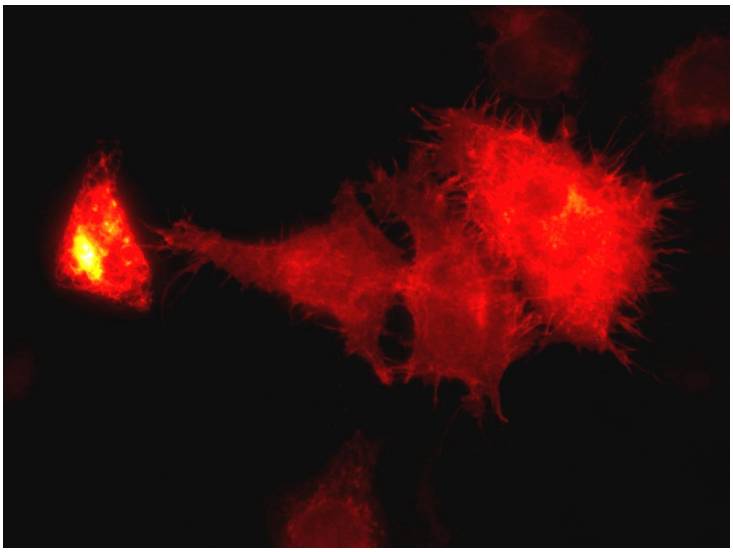

Figure 6.5: *Flourescent image of CNX-cyt-eGFP expressed in HeLa cells: Parts of the protein reached the plasma membrane.*

to the last amino acid 592). The GFP is attached on the cytosolic part, and we conserved its cytosolic position. A similar mutant, but without GFP-label, has been used by Rajagopalan et al.[113] in COS cells. They observed localization to ER, Golgi, plasma membrane and endosomes.

Deletion of the cytosolic part of CNX

20h after transfection the CNX-cyt mutant DNA in HeLa cells, the plasma membrane was stained in bright cells (see Fig. 6.5). Occasionally, rather ER and punctuate stainings were observed. So, at high expression levels, this mutant could overcome the retention mechanism and escape from the ER. Mostly at lower expression levels, the retention was still functional. Hence, one could speculate that CNX is retained in the ER by two mechanisms, one of which is disabled for the CNX-cyt mutant. At high expression levels, the second mechanisms fails to retain all CNX-cyt and a plasma membrane staining becomes visible.

6.4 Discussion

We produced several mutants of CNX in order to examine the reason for the ER localization.

To test the effect of hydrophobic mismatch, we produced several mutants with shortened or elongated TM domains and/or with changed hydrophobicity. All

these mutants additionally had the KDEL retrieval signal removed. However, none of these mutants was exported from the ER. So, the performed changes did not suffice to overcome the ER retention. Either the properties of the TM domain did not change enough or are not important for CNX localization or another powerful retention mechanism is at work. In principle, one could try out many other mutations of the TM domain, but it is not very likely that other moderate mutations would show an effect.

To assess whether another domain is responsible for ER retention, we removed larger parts of the protein. One mutant was lacking the luminal arm of the protein, a domain that extends far into the ER. Apart from a tendency to aggregate - possibly because of less steric repulsion between the luminal parts - it did not show any effect.

Removing only the KDEL retention signal has been reported to give rise to a Golgi pool in COS cells [113]. However, we still saw a clear ER localization in Hela wt cells. The difference might either come from the different cell line used or from the fact that our construct additionally possesses a GFP on the cytosolic side.

Removing most of the cytosolic domain (including the KDEL signal) finally resulted in ER export, in agreement with the findings by Rajagopalan [113]. However, it is challenging to extract information about the retention mechanism from this brute change. One can speculate that the larger cytosolic part in the wild type protein hinders engagement in COPII vesicles - possibly because some recognition sites are hidden by the large domain or more likely for steric reasons. We can also not exclude that the lack of the cytosolic domain changes the positioning of the protein within the membrane more dramatically than our TM domain mutations. In this case, hydrophobic mismatch might still play a role.

Part III

Results: Cell shape and organelle organization

Chapter 7

Shaping cells

In order to impose a certain geometry on cells, we first used microcontact printing. Later on, we switched to a commercially available solution based on a similar approach. Both approaches and results obtained are described in this chapter.

7.1 Introduction

In the last part of this thesis, we wish to study the influence of cell shape on the internal spatial organization of the cell. Therefore, a means to influence the cell shape was needed.

Microcontact printing has been used by various groups to restrict cell growth to certain areas of the substrate [114–116]. To this end, an elastic stamp is fabricated and used to print a substance onto a substrate that promotes cell adhesion. Additional surface modifications might be used depending on the exact protocol. Often, the surface around the stamped region is additionally passivated. In the ideal case, cells will only grow on the stamped regions and adapt their shapes to the printed pattern.

Recently, patterned chips became available from Cytoo SA (Grenoble, France). Several geometries and sizes of patterns are available.

7.2 Microcontact printing

The basic principle of microcontact printing is illustrated in Fig. 7.1. First, an elastic stamp is fabricated from a silicon master. Then, this stamp is used to stamp a material that promotes cell attachment onto a cleaned and activated glass slide.

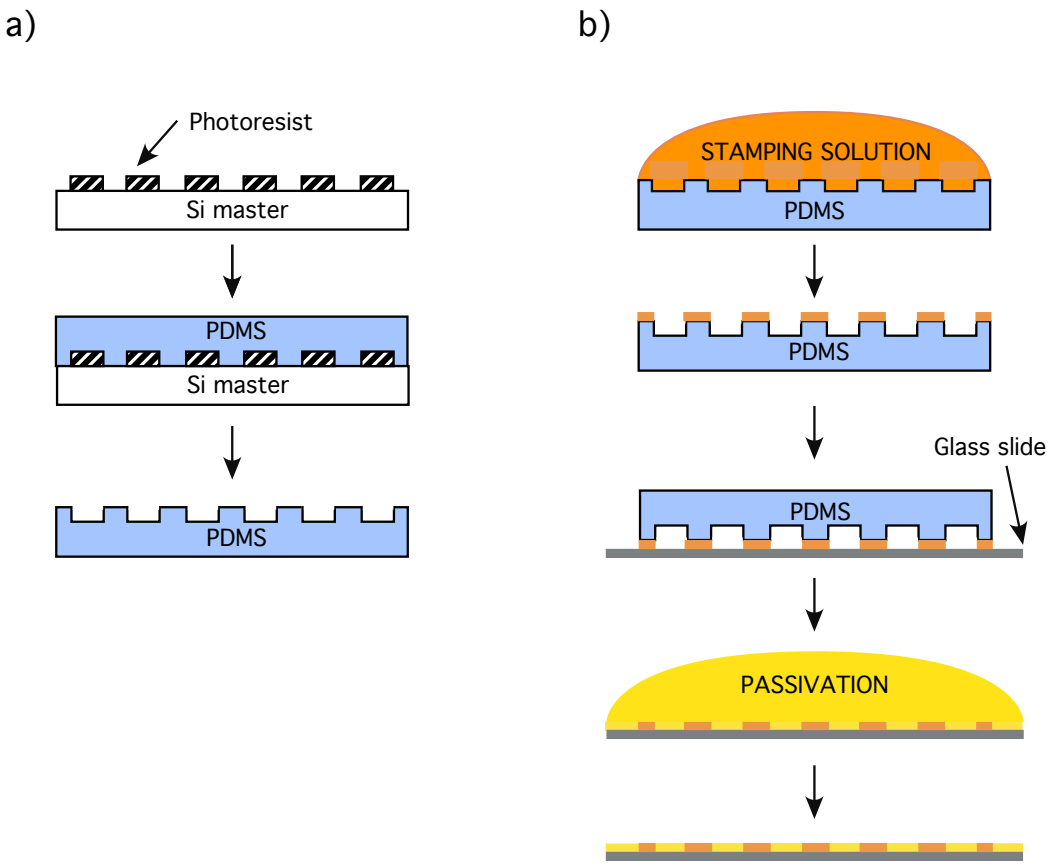

Figure 7.1: *(a) Principle of stamp fabrication: A silicon master is produced by photo-lithography and used to cast-mold a PDMS stamp (b) Principle of microcontact printing: PDMS stamps are incubated with stamping solution, dried and placed into contact with glass substratum. To passivate surrounding parts of the substratum, the slide is washed with a passivating solution.*

Commonly, extracellular matrix proteins such as fibronectin are used as stamping solution. Additionally, the regions around the fibronectin patches are passivated.

7.2.1 Material and methods

For our microcontact printing protocol, three steps are necessary: Fabrication of the stamp, stamping and finally cell seeding.

The elastomeric stamp is fabricated by cast molding

For stamp preparation, a silicon master is prepared by lithography. The photo mask was designed with CleWin software and ordered at ML&C, Jena. As patterns, different geometric forms (square, circle, rectangle, L-shaped form, triangle, hexagon, half-circle) were chosen, with an area of 900 μm^2 each. Additionally, the mask contains a region with gradients of different sized rectangles and triangles. From this photographic mask, silicon masters were produced in the lithographic facility at the KIP (University of Heidelberg), by spin-coating photoresist on a silicon master, placing the mask over it, and illuminating the resist. The non-illuminated regions can then be removed by etching.

The actual stamp is made from Sylgard 184 elastomer (Dow Corning Inc, curing agent:elastomer 1:7). After mixing the two components and centrifuging the mixture for 5 min at 1500 RPM, the mix is poured over the master and placed in a dessicator for half an hour to remove air bubbles. Afterwards, the stamp is cured at $70°C$ for 2h. The obtained stamps are about 5mm to 1cm thick, elastic, and hydrophobic.

The stamping process consists of surface cleaning and activation, surface modification, stamping and passivation

The actual stamping process consists of several steps: Cleaning and activation of cover slides, optional surface modifications (silanization), stamping and passivation of the non-stamped regions. For most of these, several strategies have been explored. Below, some of the more successful options are listed.

Surface cleaning and activation Two approaches for surface cleaning and activation were chosen.

1. To clean cover slides, they were sonicated for 10min in acetone, followed by 10min in ethanol and two times 5min in Millipore water. For activation, they were incubated in a 1:1 mix of MeOH:HCl (1M) for at least 1h to overnight and rinsed again in water. Afterwards, they were dried with nitrogen.

2. For some experiments, the slides were cleaned in Caro's acid for at least 1h, stored in water and shortly before usage plasma treated for 10min for better surface activation. These experiments were conducted in the group of Prof. J. Spatz (Biophysical Chemistry, University of Heidelberg).

Surface modification - silanization To prepare the surface for stamping, an optional surface modification step can be introduced. Here, the slides were

put for 30s up to 30min in 5% Aminopropyltriethoxysilane (APES) in acetone after activation. Afterwards, they are rinsed in PBS and incubated for 10min in 0.5mg/ml BS3 (bis sulfosuccinimidyl suberate) for cross-linking. Finally, slides were rinsed in PBS and dried with nitrogen.

However, this step did not seem to improve results and was therefore skipped in later experiments.

Stamping Several stamping solutions were tested. First, a mixture of extracellular matrix proteins, i.e. a 2:1 fibronectin:labelled fibrinogen mixture at a concentration of 50 $\mu g/ml$ was used. Later, a 0.01% solution of poly-l-lysine was taken. Poly-l-lysine is small natural homopolymer of the essential amino acid l-lysine. It is commonly used to enhance cell attachment in cell culture.

The PDMS stamps were incubated with the stamping solution at least 30 minutes before stamping to let the protein/polymer adsorb to the surface. Excess liquid was removed by blowing nitrogen over the surface and the stamp was placed on the cover slide and a small weight placed onto the stamp. After 5 minutes the stamp was removed.

Optionally, the stamps were treated with plasma for about 1 minute before incubation. This renders the PDMS surface hydrophilic. Protein unfolding due to hydrophobic interactions hence becomes less likely (when using a protein, e.g. fibronectin, for stamping).

Passivation For passivation, the cover slides were placed upside down onto a drop of PLL-g-PEG or PLL-g-PEG-FITC (1mg/ml) on parafilm for 5min to 2h. PLL-g-PEG is a graft co-polymer of poly(L-lysine) and poly(ethylene glycol), which repels proteins when adsorbed to a surface. Afterwards, slides were rinsed and stored in PBS. Also passivating slides in a first and stamping thereafter was tried.

Cells were seeded in serum-reduced medium

HeLa wt cells were trypsinized, centrifuged and resuspended in serum-reduced medium (2.5% FCS). Stamped slides were placed in 6-well dishes and the cell solution was added.

Optionally, a medium change was done after 80 minutes to remove non-attached cells.

Figure 7.2: *(a) Fluorescence image of a microcontact stamp on glass slides that were treated with Caro's acid and plasma, stamped with fibronectin:fibrinogen-FITC and passivated with PLL-g-PEG. (b) bright field image of the cells growing on these stamps.*

7.2.2 Results

With all protocol variations listed above, samples which showed preferential cell attachment on the stamped regions could be produced. In Fig. 7.2, a sample were the glass slide was cleaned in Caro's acid and activated by plasma treatment is shown. Here, no silanization was applied and a fibronectin:fibrinogen mixture was used for stamping and PLL-g-PEG for passivation. Cells grew on the stamped parts. However, their attachment seems to be limited and cells do not adapt their shape to the stamped forms.

Better results were obtained using poly-l-lysine for stamping and PLL-g-PEG for passivation. The sequence of the two steps did not seem to matter. Mostly, cleaning in acetone and ethanol and activation in MeOH:HCl was used.

On some samples, results as shown in Fig. 7.3 were obtained. Here, cells roughly take the shape of the stamps, yet do not follow exactly. Also, some passivation material (labeled with the fluorophore FITC) is seen in the stamped regions.

However, overall only about 1 out of 8 samples worked. Additionally, the cell shapes were rarely optimal, so we decided to switch to the solution by Cytoo that became commercially available at that time. With the experience made with Cytoo chips, some points for improvement became obvious. First, the cell type used was not optimal (RPE1 cells adapt more easily than HeLa wt cells to the patterns on the Cytoo chips). Second, our mask design features shapes, which are completely filled with the attachment protein. This, however, provides the cell too many possibilities to form attachment points and thus does not force it to exactly follow the shape of the pattern. Stamping only the boundaries of the shape or some other appropriate line pattern would have been the better approach.

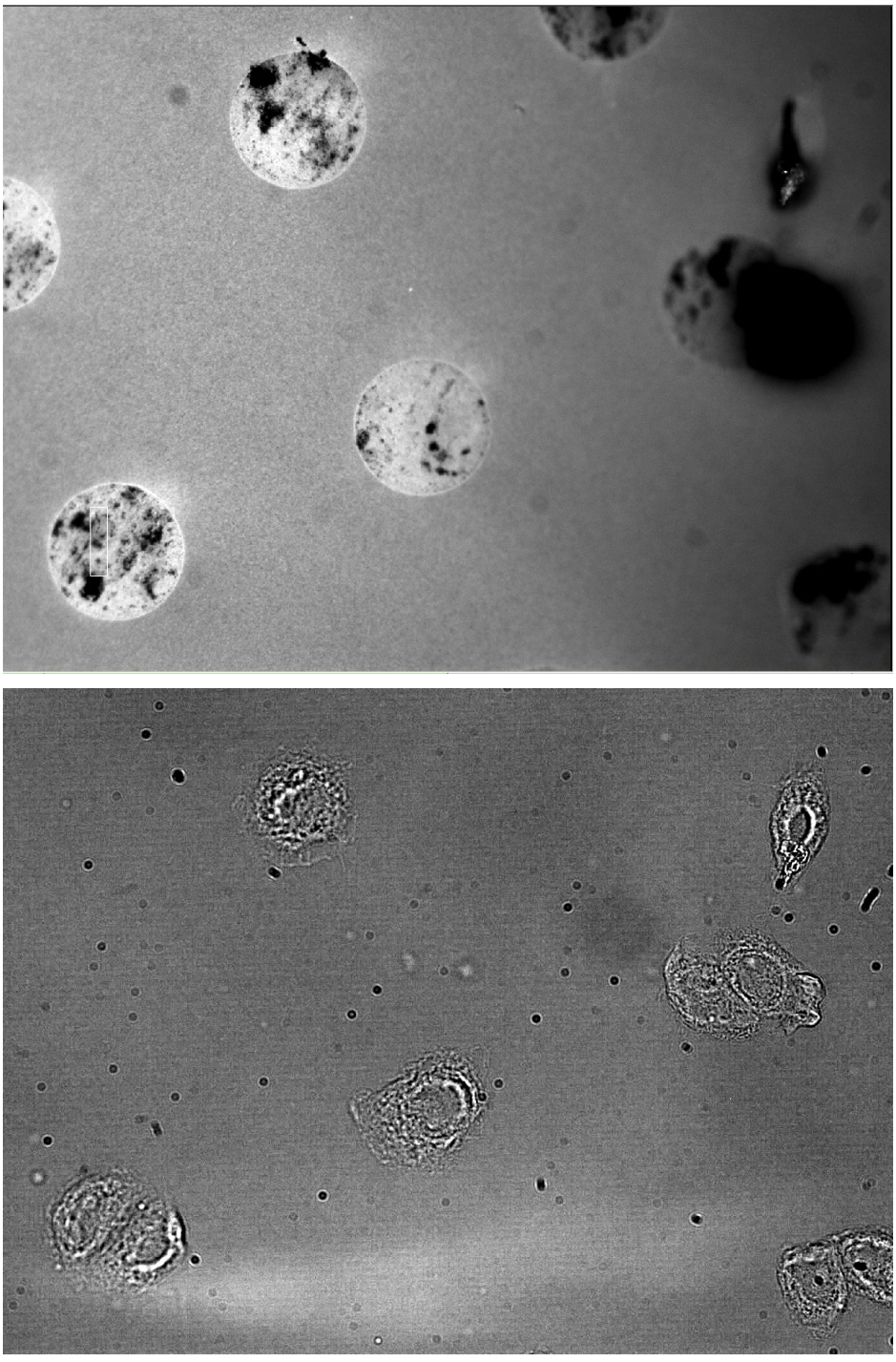

Figure 7.3: *(a) Fluorescence image of a microcontact stamp of poly-l-lysine on a glass slide that was treated with acetone and methanol for cleaning, MeOH:HCl for activation, stamped and passivated with PLL-g-PEG-FITC for 5min (b) bright field image of the cells growing on these stamps.*

7.3 Cytoo chips

Cytoo SA (Grenoble, France; http://www.cytoo.com/) offers adhesive micropatterns to control cell shape. The adhesive substance used is fibronectin, attached to glass slides. Several standard shapes and sizes can be ordered. Starter chips exist, containing patterns in four different shapes and three different sizes, and standard chips containing only one shape in one size. In Fig. 7.4 a starter chip and a standard chip featuring crossbow patterns are shown. Each chip is subdivided into 144 areas, each containing 81 or 144 big or medium/small patterns, respectively. The 144 areas are separated by lines of fibronectin, to which cells can also attach. The three sizes of the shapes available are 700 μm^2, 1100μm^2 and 1600 μm^2.

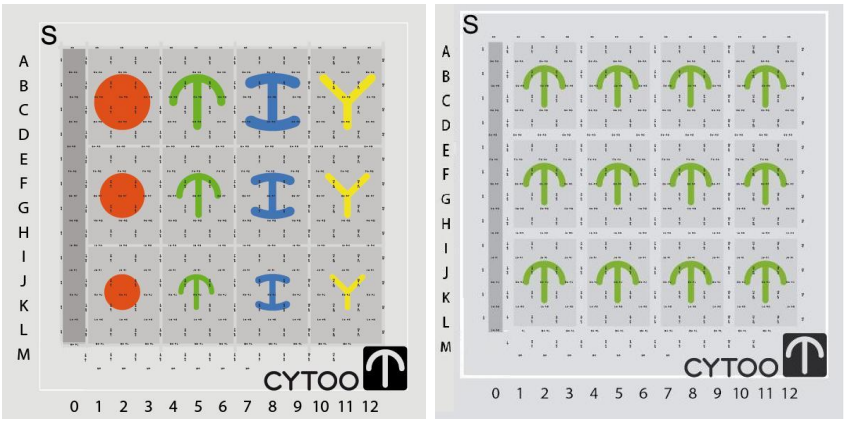

(a) starter chip (b) standard crossbow chip

Figure 7.4: *(a) Starter cytoo chip containing circular, crossbow-shaped, H-shaped and triangular patterns in three sizes (b) Standard cytoo chip featuring only crossbow-shaped patterns of one size. Pictures taken from http://www.cytoo.com/.*

7.3.1 Materials and Methods

Cell culture

HeLa wt cells and RPE1 (retinal pigment epithelial) cells were cultured in DMEM supplemented with 10% fetal calf serum and 1% penicillin and streptomycin (Invitrogen). RPE1 cells were a gift from Rainer Pepperkok (EMBL, Heidelberg).

For cell shape experiments, cells were seeded on Cytoo chips following the manufactures protocol (CYTOO SA, Grenoble), but with a modified cell concentration. Briefly, cells were trypsinized, centrifuged and well resuspended in fresh medium

ANTIBODY	DILUTION	TARGET	COMPANY
GM130 (mouse)	1:200	golgi	BD Biosciences
α -tubulin (mouse)	1:200	microtubuli	BD Biosciences
α -tubulin (rabbit)	1:100	microtubuli	Molecular Probes
γ-tubulin (mouse)	1:400	centrosome	Sigma
Alexa594 (goat-anti-ms)	1:300	secondary antibody	Invitrogen
Alexa633 (goat-anti-rb)	1:300	secondary antibody	Invitrogen

Table 7.1: *Antibodies and concentrations used for immunofluorescence of RPE1 cells.*

at a concentration of 60000cells/ml. Cytoo chips were placed in 6-well dishes and $1.4ml$ of cell suspension was carefully added. Plates were kept in the hood for 10min and afterwards transferred to the incubator. 25min after seeding, slides were washed with fresh medium to removed non-attached cells. Care was taken not to dry the cells in order not to cause cell stress. Afterwards, cells were grown on the chips for at least 1h to 24h before fixation.

Mostly, cells were fixed with 4% paraformaldehyde (PFA) for 10 minutes. Afterwards, cells were stained using the standard Abcam immunofluorescence protocol and primary antibodies α-tubulin, rabbit (Molecular Probes) and GM130, mouse (BD Biosciences). Cells were mounted on object holders using Fluoromount (SouthernBiotech).

When centrosome staining was done, cells were transfected using $2\mu l$ Fugene6 (Roche) and $0.7\mu g$ GalNac-T2-GFP DNA in $48\mu l$ of DMEM the day before the experiment (at least 4h before seeding cells on the Cytoo chips). For immunofluorescence, cells were fixed with $1:1$ methanol : acetone at $-20°$C for 10min.

Image acquistion

Fixed samples were imaged using a Leica SP5 confocal laser scanning microscope equipped with a 40X oil objective. All images were taken in sequential imaging mode and with 2-or 3-fold line averaging and zoom 6. The pinhole was set to 2 Airy units.

7.3.2 Results

At first, we used HeLa wt cells on the Cytoo starter chips. Cell shape adaptation worked best on the smallest pattern size. However, only about 200 cells with

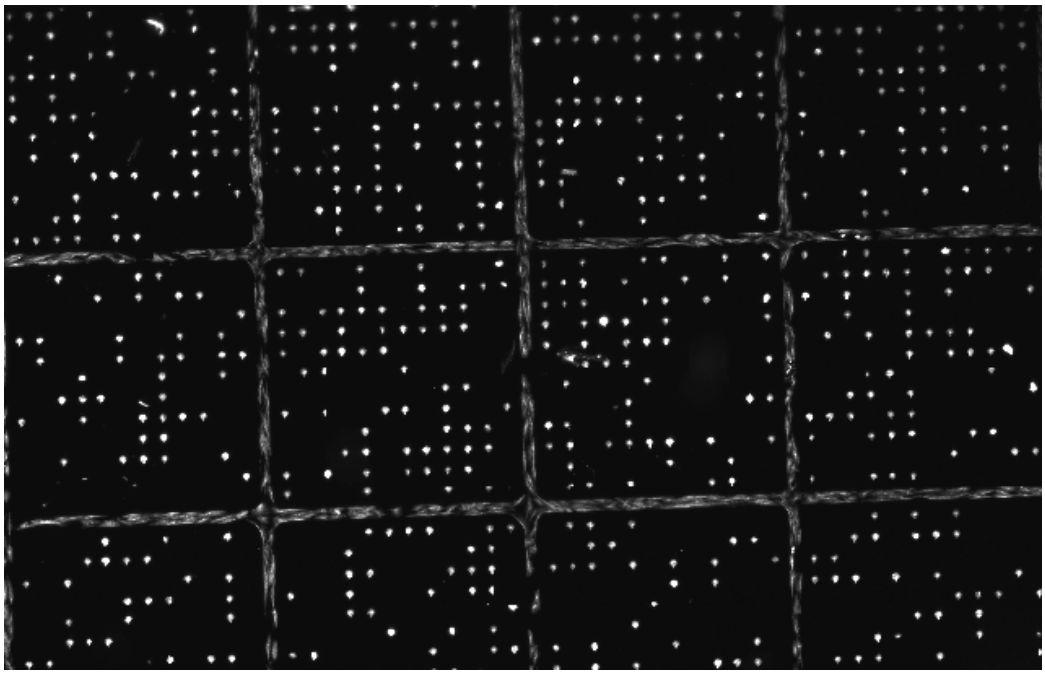

Figure 7.5: *Tile scan wide field fluorescent image: RPE1 cells growing on a standard crossbow Cytoo chip. Cells can attach on the fibronectin lines separating the 144 areas on the chip and on the bow-shaped patterns. Cells were fixed and microtubules were stained with an α-tubulin antibody.*

the right shape could be detected on a chip. As a chip provides printed patterns for 20736 cells, this corresponds to a successful attachment rate of only about 1%. Therefore, we switched to RPE1 cells that have been used on Cytoo chips before [117, 118]. These cells are larger than HeLa cells and grow best on the medium size patterns. Circle, crossbow and triangle worked better than the H-shape. As the circle possesses no predefined orientation for analysis of spatial relationships within the cell, all further experiments are conducted with bow-shaped or triangular patterns.

In Fig. 7.5 RPE1 cells growing on a standard crossbow ship are shown. Obviously, not every pattern is occupied by a cell. Also, many patterns are occupied with several cells. Therefore, higher resolution image acquisition was not automated and only spots containing single cells were imaged.

In Fig. 7.6 and Fig. 7.7, a triangular and a crossbow-shaped RPE1 cell are shown. In both cases, the cells were stained for microtubules, nucleus and Golgi apparatus. Images were taken with a confocal microscope (pinhole opened at 2 Airy units). The image plane was optimized to see the Golgi apparatus. Obviously, in the triangular cell (Fig. 7.6) the Golgi apparatus and the microtubules lie in

the same plane, so that the whole microtubule network is visible. In contrast, in crossbow cells, the Golgi apparatus lies in a different section and only parts of the microtubules are visible (Fig. 7.7). This can be explained by a bigger thickness of the crossbow cells as compared to the triangular ones.

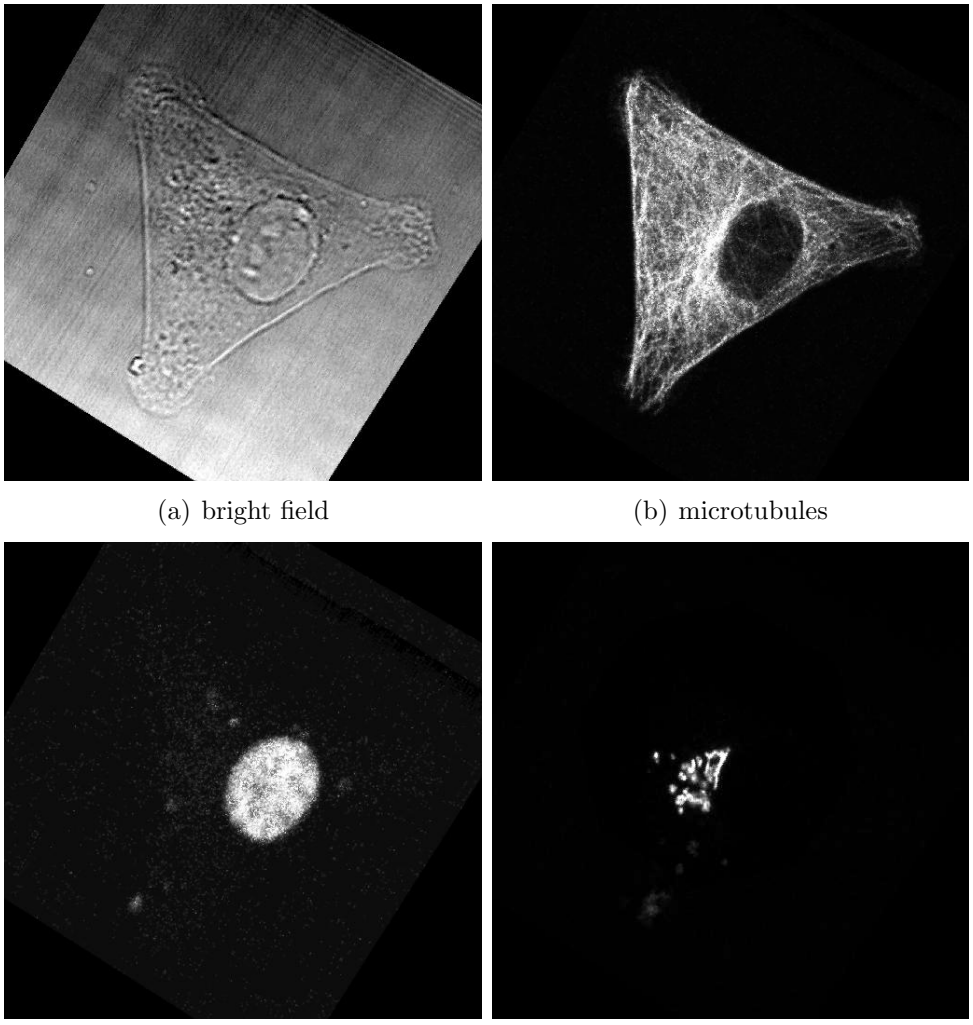

(a) bright field (b) microtubules

(c) nucleus (d) Golgi apparatus

Figure 7.6: *Confocal image of a triangular cell. a) bright field b) microtubule network c) nucleus d) Golgi apparatus.*

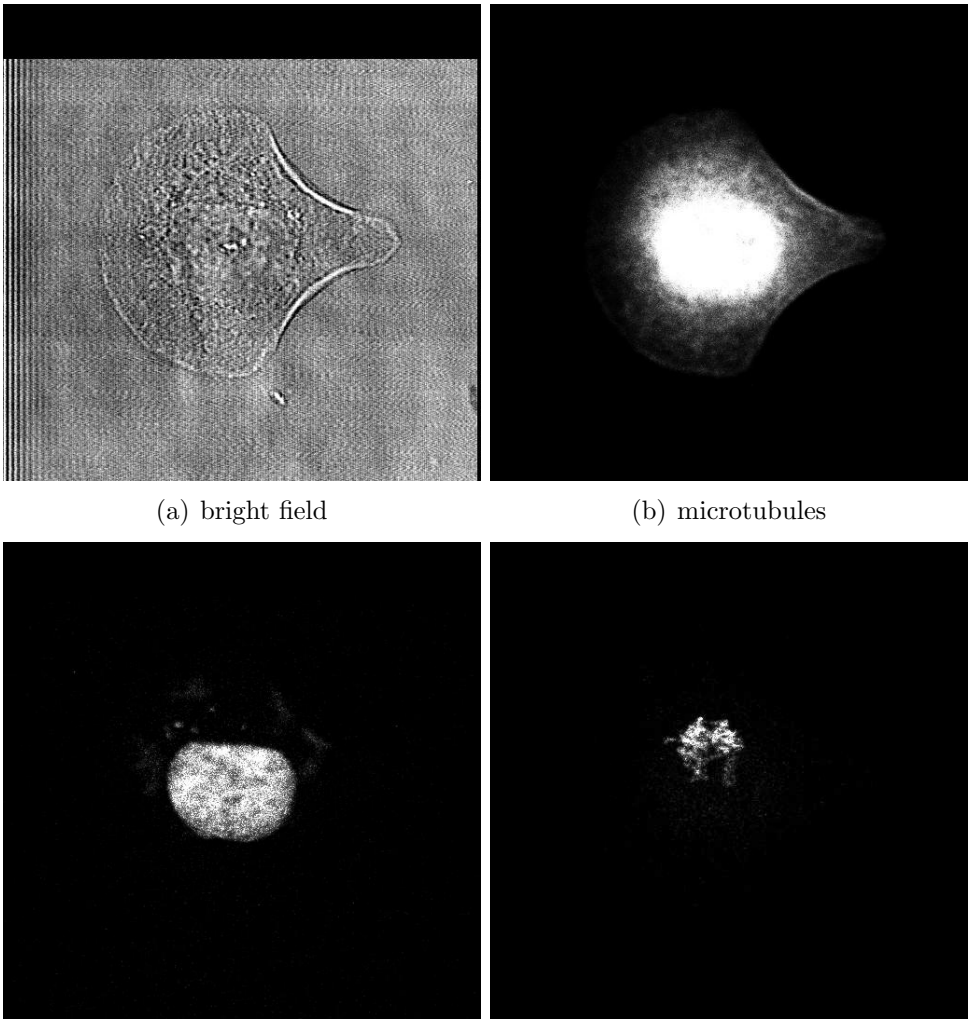

(a) bright field (b) microtubules

(c) nucleus (d) Golgi apparatus

Figure 7.7: *Confocal image of a bow-shaped cell. (a) bright field (b) microtubule network (c) nucleus (d) Golgi apparatus.*

Chapter 8

The influence of cell shape on organelle position

In this chapter, we study the position of centrosome, Golgi apparatus and nucleus in triangular and crossbow-shaped cells. For triangular cells, the problem can be approximated as being two-dimensional and the observed positions can by explained by simulations.

8.1 Introduction

One of the most prominent feature in cell biological experiments is the heterogeneity of a cell population. Data on anomalous diffusion in the ER presented in Chapter 5, transport rates through the secretory pathway [119], or differences in DNA expression after transfection show strange cell-to-cell variations. Therefore, populations of seemingly identical cells show different features. Sometimes, by looking just at the mean, the real information in the data is lost [5, 120]. One of the key tasks for single cell measurements is to find out whether any of these differences serve a biological function.

Many cell biological experiments are using culture cells, where cells that grow in 2D without any further restrictions made on attachment points or available space. Under such conditions, individual cells have very different shapes. However, in a body many tissues exist that are highly organized, constraining e.g. the geometry of cells and defining interfaces to neighboring cells. Prominent examples are epitheliums in mammals as well as muscle tissues. Furthermore, cells building tubes of all kinds, e.g. blood vessels, have a defined shape. Also in Drosophila embryos, somatic cells form a layer around the embrio and possess a highly regulated shape [54].

As has been shown in the previous chapter, cells grown on Cytoo chips possess a predefined (two-dimensional) geometry. Some publication used this tool to define a "standard cell" [118, 117]. Here, we want to revisit this approach and look at the relative positions of nucleus, Golgi apparatus and centrosome with a particular focus on the remaining noise in the positioning. We find that also in equally shaped cells, variations in the positions of the organelles remain. Also, adaptation of the internal geometry to the cell shape is slow. For the Golgi apparatus and the centrosome, the variability of the position decreases between 6h and 20h after cell seeding, corresponding to a remarkably long time scale of almost one cell cycle. Additionally, the centrosome is normally supposed to locate at the cell center (see Section 3.4). However, we find a surprisingly large distance of the centrosome from the cell center. Any of these persisting variations will probably be a source of noise for transport through the secretory pathway or along microtubules that cannot be suppressed by using cells of equal geometry and thus contradict the notion of a "standard cell". Furthermore, also in tissues with equally shaped cells, this noise will persist and probably influence the functionality of the cells.

In a second step, the observed positions are explained by a simulation model. Following the approach of Holy et al. and Nedelec [55, 121] microtubules showing dynamic instability and growing radially from an aster were simulated. Additionally, we applied boundary conditions corresponding to the Cytoo geometry and modeled the interaction of the cell membrane with the nucleus. This simple model already provides a good agreement with many experimental observations. Additional microtubule interactions with the cell boundary and restricting their growth to the cytoplasm further improve the model.

8.2 Experimental results

8.2.1 Positioning of the Golgi apparatus and the centrosome is a slow process

As described in Sections 7.3.1 and 7.3.2, RPE1 cells were seeded on Cytoo chips (crossbow-shaped or triangular) and fixed after a certain time. Samples were stained for microtubules, nucleus, Golgi apparatus and/or centrosome and images of single cells were acquired. To label the Golgi apparatus and the centrosome at the same time, cells were transfected with the Golgi protein GalNAc-T2-GFP prior to cell seeding on Cytoo chips (using Fugene6, Roche as transfection agent) and stained for γ-tubulin, a centrosome component. Fixation times and stainings for each sample are shown in table 8.1.

To analyze the images, they were automatically processed in Matlab. The outline of the cell was determined by thresholding the microtubule image. The obtained

Fixation time	Transfection DNA	antibodies against	Number
triangular			
2 h	GalNAc-T2	centrosome, MT	81
4 h	GalNAc-T2	centrosome, MT	63
6h	GalNAc-T2	centrosome, MT	84
20h	-	golgi, MT	108
bow-shaped			
4 h	GalNAc-T2	centrosome, MT	66
6h	GalNAc-T2	centrosome, MT	83
20h - sample 1	-	golgi, MT	152
20h - sample 2	-	centrosome, MT	95

Table 8.1: *Overview of the fixed samples: fixation time, transfections, staining performed and number of cells imaged.*

binary image was shifted in random steps and the overlay with a binary cell-shaped picture was maximized.

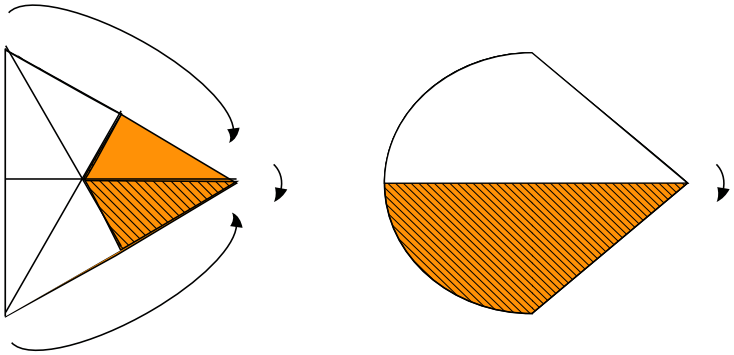

Figure 8.1: *Triangular cells are rotated so that the center of mass of the nucleus lies within the orange region. Afterwards, cells are flipped so that the center of mass ends up in the orange striped region. For the crossbow cells, only flipping is possible. Here, the nucleus is also moved to the orange and striped region.*

To take into account the symmetry of the pattern, the center of mass of the nucleus was determined from a thresholded image of the nucleus. The images were turned and/or flipped in order to overlay the nuclei as well as possible. For the crossbow cells, the reflection symmetry was used so that the center of mass of the nucleus always came to lie in the lower half of the image. For the triangle, the image was rotated to place the center of mass of the nucleus close to the left edge of the triangle and afterwards the reflection symmetry was used to mirror the center of mass of the nucleus into the lower half. For illustration see Fig. 8.1.

In Fig. 8.2 and Fig. 8.3 overlays of cells fixed at different time points are shown. Interestingly, in triangular cells the nucleus never assumes a position in the middle of the cell. The nucleus is for all time points close to one side of the triangle. The Golgi apparatus and the centrosome are more centralized in the cell. However, the variations in the positions still seem fairly large. Only for the 20h time point, the Golgi apparatus locates well to the cell center. Hence, adaptation of the internal geometry to the cell shape is remarkably slow.

For the bow-shaped cells, the same observation holds true for the Golgi apparatus. The nucleus here positions towards the tip of the bow, but more in the cell center than for the triangular cells. Also the overlap with the Golgi apparatus or centrosome is bigger, meaning that the centrosome and Golgi apparatus come to lie on top of the nucleus (c.f. Fig. 7.7 in the previous chapter) more often, especially for larger times.

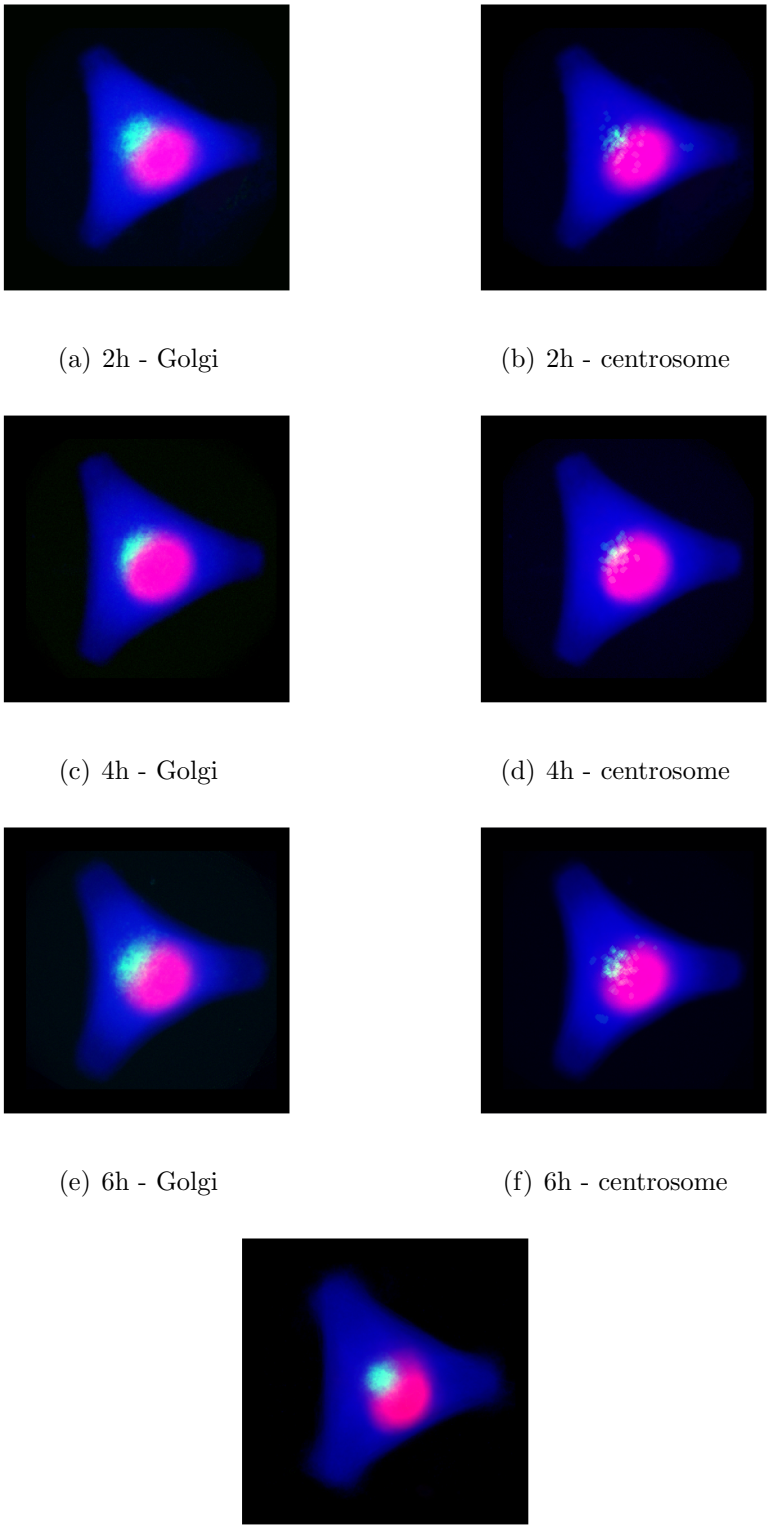

(a) 2h - Golgi

(b) 2h - centrosome

(c) 4h - Golgi

(d) 4h - centrosome

(e) 6h - Golgi

(f) 6h - centrosome

(g) 20h - Golgi

Figure 8.2: *Overlays of nucleus (pink), microtubules (blue) and Golgi apparatus (green) or centrosome (green) in triangular cells. Cells were fixed 2h, 4h, 6h or 20h after seeding on Cytoo chips.*

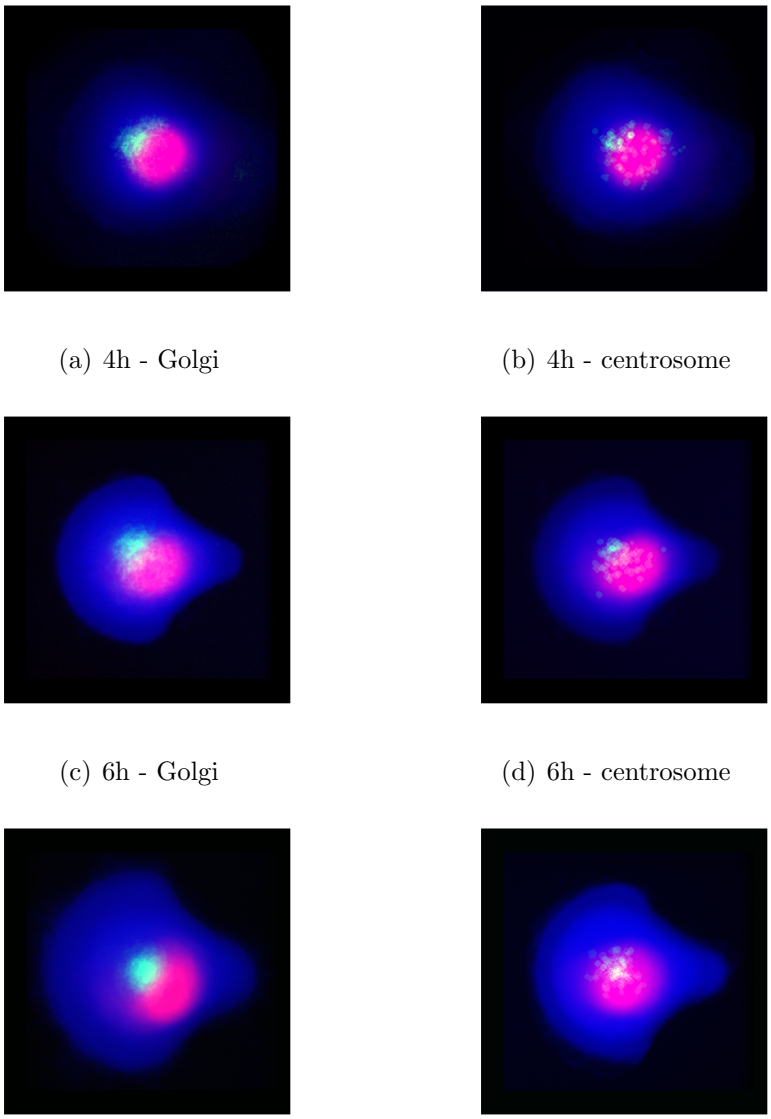

(a) 4h - Golgi

(b) 4h - centrosome

(c) 6h - Golgi

(d) 6h - centrosome

(e) 20h - sample 1- Golgi

(f) 20h - sample 2 - centrosome

Figure 8.3: *Overlays of nucleus (pink), microtubules (blue) and Golgi apparatus (green) or centrosome (green) in crossbow cells. Cells were fixed 4h, 6h or 20h after seeding on Cytoo chips. For the 20h data point, Golgi apparatus and centrosome staining were performed on different samples.*

8.2.2 Positions of organelles show large variations

As already mentioned above, all cells show a quite large variation in the positions of organelles. This becomes even more obvious, when looking at the scatter plots in Fig. 8.4 and the display for nine individual cells in Fig. 8.5 (data for crossbow-shaped cells not shown). Standard deviations are in the order of 10 to 30 pixels, which corresponds to 1.3 to $3.9\mu m$. Taking into account that the width of the triangular cell is only about $35\mu m$ and the diameter of the crossbow cell $28.2\mu m$, positioning seems to be surprisingly imprecise.

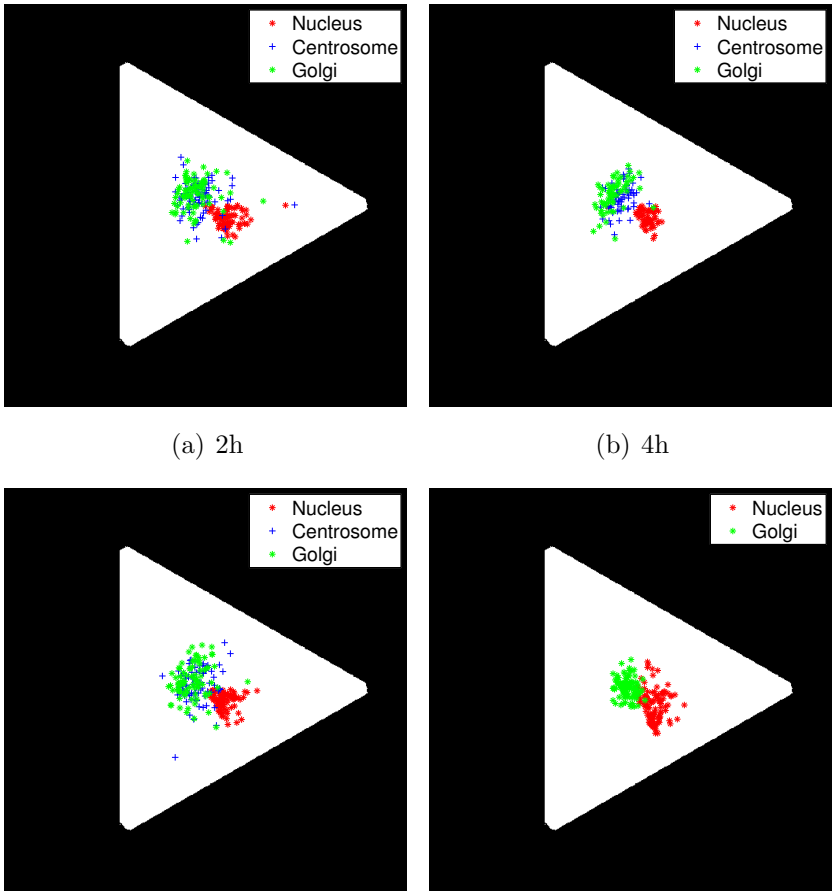

(a) 2h (b) 4h

(c) 6h (d) 20h

Figure 8.4: *Positions of nucleus, centrosome and Golgi apparatus in triangular cells.*

In summary, the positions of Golgi apparatus, centrosome and nucleus show large variations. Golgi apparatus and centrosome find the cell center more precisely, when waiting 20h after cell seeding - i.e. after almost one cell cycle. These results

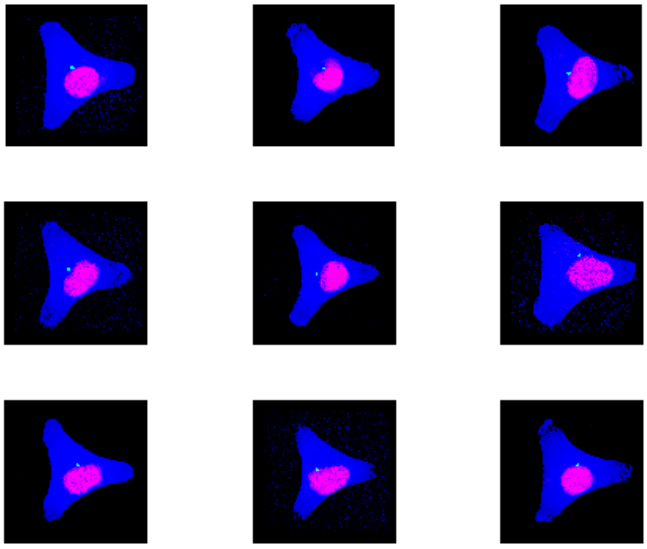

Figure 8.5: *Overlays of nucleus (pink), centrosome (green) and microtubules (blue) for nine individual triangular cells, fixed 6h after cell seeding. Obviously, cell-to-cell differences in organelle positions exist.*

highlight the persistence of variations in the cells' internal organization and thus challenge the notion of a "standard cell" that has been introduced before [118, 117]. Remarkably, this idea of a standard cell is based on data that was taken from cells fixed only 2-4h after cell seeding on Cytoo chips.

8.2.3 Positions of Golgi apparatus and centrosome are correlated, the position of the nucleus' center of mass is independent

As the variations in the positions are big, we next looked at correlations in the positions of the different organelles. Correlation coefficients were calculated using the formula $R(i,j) = \frac{C(i,j)}{\sqrt{C(i,i)C(j,j)}}$ where $C(i,j) = E[(x_i - \mu_i)(x_j - \mu_j)]$ is the covariance of x_i and x_j.

The positions of Golgi apparatus and centrosome are correlated with correlation values $R(i,j) > 0.8$. This can be understood easily, when remembering the formation of a Golgi apparatus: Vesicles budding at the endoplasmic reticulum fuse and are transported along microtubules towards the cell center. As the microtubules are emanating from the centrosome, it is obvious that Golgi apparatus and cen-

trosome position depend on each other. For further analysis we hence take the centrosome position to be representative of the Golgi apparatus position and only analyze the centrosome position further.

Surprisingly, no significant correlations between the positions of Golgi apparatus or centrosome and nucleus exist.

8.2.4 The centrosome does not position precisely at the cell center

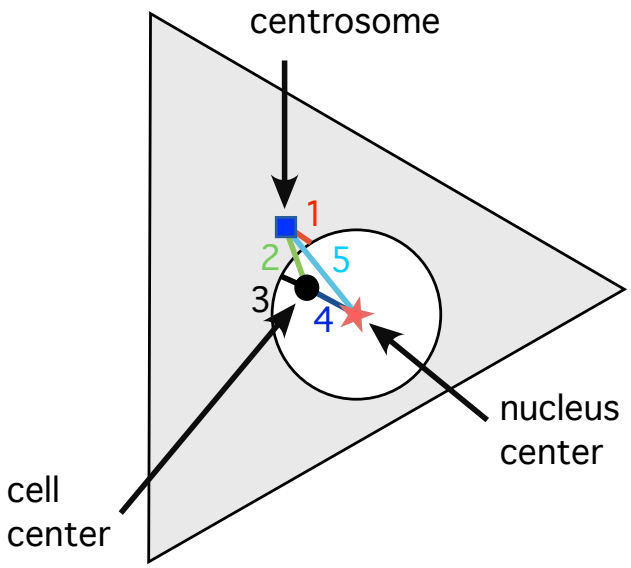

Figure 8.6: *Illustration of the distances analyzed: The red star represents the center of mass of the nucleus, the blue square the centrosome, and the black circle the cell center. Distances 4 and 5 are the distances from the nucleus center to the cell center and centrosome respectively. Distance 2 is the distance from the cell center to the centrosome. Distances 1 and 3 are the distances from the centrosome and the cell center to the nucleus boundary, respectively. The most common arrangement of the organelles is depicted here, i.e. with the cell center within the nucleus and the centrosome on the outside.*

Next, we looked at several distances between the centrosome, nucleus, and cell center. In Fig. 8.6, the considered distances are explained. Distance 1 and 3 are the distances from the centrosome and the cell center to the nucleus surface, respectively. When cell center or centrosome lie "in" the nucleus in the two-dimensional image, the corresponding distance is taken to be negative. Distance 2 is the distance between the centrosome and the cell center. Distances 4 and 5 are

the distances from the nucleus center of mass to the cell center and the centrosome, respectively.

Histograms of the lengths 1 to 5 for the latest time points are shown in Fig. 8.7 and Fig. 8.8 for triangular and crossbow-shaped cells, respectively.

The cell center lies inside the nucleus Distance 3, the distance from the cell center to the nucleus surface is mostly negative, i.e. the nucleus in most cases includes the cell center. However, as distance 4 (from the nucleus center of mass to the cell center) is always greater than zero, the middle of the nucleus and of the cell never colocalize.

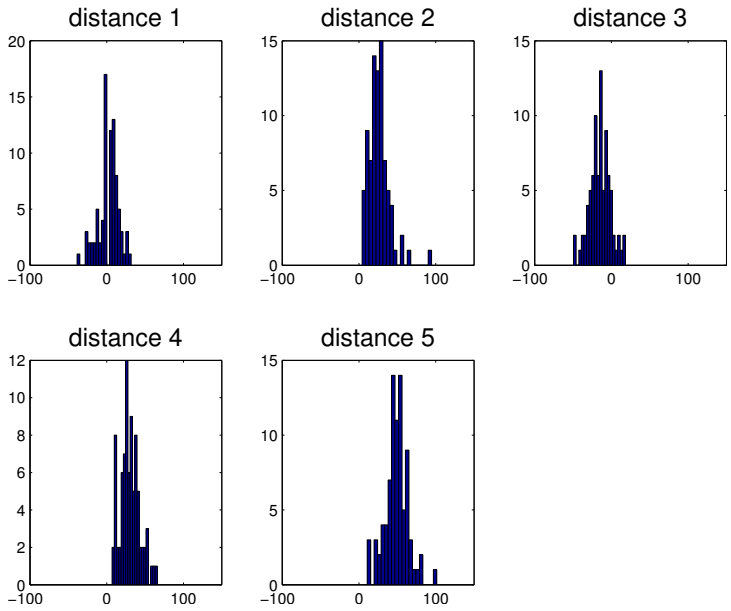

Figure 8.7: *Histograms of distances 1 to 5 (c.f. Fig. 8.6) in triangular cells , fixed 6h after cell seeding. Remarkably, distance 1 is close to zero and mostly positive, e.g. the centrosome lies close to the nucleus surface, but mostly outside of it (in the two-dimensional projection). Distance 2, the distance between the centrosome and the cell center is similar to all other distances.*

The centrosome positions beside the nucleus in triangular cells Another interesting observation concerns the position of the centrosome relative to the nucleus surface (distance 1). Importantly, one has to keep in mind that the images are a two-dimensional projection of a three-dimensional cell. In vivo, the centrosome surely cannot enter the nucleus, but it can lie on top (or below) of it. In this cases, the centrosome lies "within" the nucleus in the two-dimensional

image and the distance 1 becomes negative. Distance 1 shows in all cases a peak at zero distance with only small variations, i.e. the centrosome is touching the side of the nucleus. As already mentioned before, for crossbow-shaped cells the centrosome more frequently lies on top of the nucleus. This can be explained by crossbow-shaped cells being thicker and thus providing more space for the Golgi apparatus and centrosome above the nucleus. This was also already noticed during imaging of the cells (see remark in Section 7.3.2).

As a consequence, the spatial arrangement of nucleus, centrosome, and Golgi apparatus can be approximated as a two-dimensional problem in triangular cells. Therefore, our 2D simulation model presented in the next section will concentrate on explaining the phenotype in triangular cells.

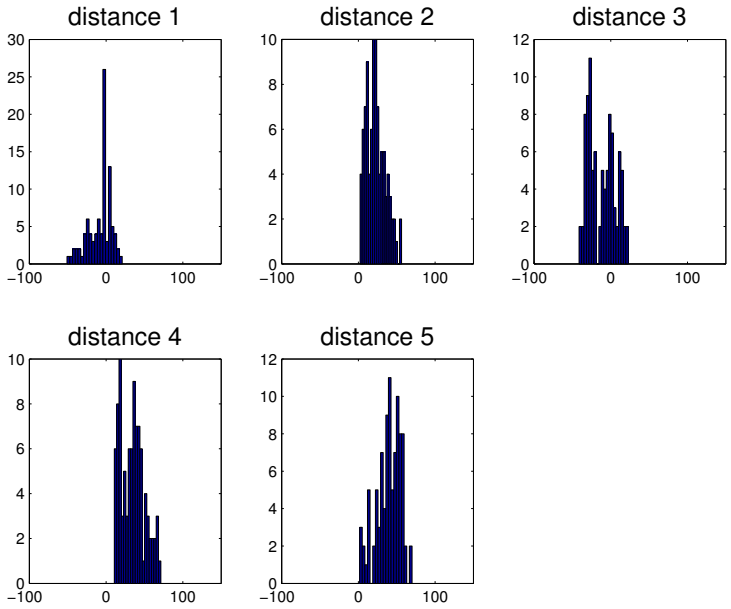

Figure 8.8: *Histograms of distances 1 to 5 (c.f. Fig. 8.6) in crossbow-shaped cells, fixed 20h after cell seeding. Remarkably, distance 1 is here also close to zero, but often "within" the nucleus in the 2D projection. Distance 2, the distance between the centrosome and the cell center is again similar to all other distances.*

The centrosome does not position precisely at the cell center and shows a preferential direction of displacement in triangular cells In in vitro experiments, an aster from which microtubules emanate, finds the center of a dish [55]. Surprisingly, distance 2 and distance 4 are comparable, i.e. nucleus and centrosome show a similar distance from the cell center. Hence, the centrosome does not position precisely at the cell center in vivo, but additional forces seem

to be at work. A model explaining the centrosome and nucleus position will be described in Section 8.3.

In Fig. 8.9 the vector 2, e.g. the vector pointing from the cell center to the centrosome is displayed. Obviously, the distribution is non-uniform for triangular cells. The centrosome preferentially lies in the direction opposing the nucleus, i.e. there seem to be steric interactions between centrosome and nucleus. In crossbow-shaped cells the distribution is more uniform (see Fig. 8.10). Again, this agrees with the picture of crossbow-cells being thicker than triangular cells which allows the centrosome to lie on top of the nucleus for larger times.

In summary, in triangular cells the relative positions of nucleus and centrosome can be displayed as a two-dimensional problem, as the centrosome only rarely lies on top of the nucleus. For crossbow-shaped cells, this is not possible as these cells are thicker. For both cell types we observed surprisingly large distances from the centrosome to the cell center and for triangular cells a preferential displacement of the centrosome away from the nucleus. In the next section, we will describe a simulation model capable of explaining the situation in the triangular cells.

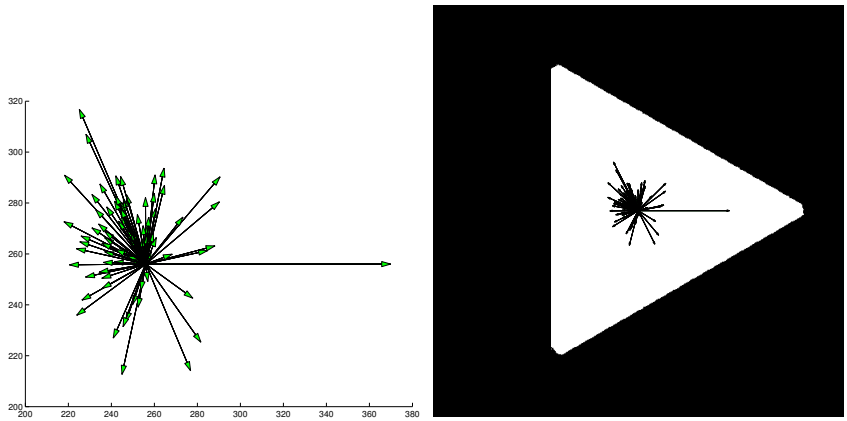

(a) 2h

(b) 2h

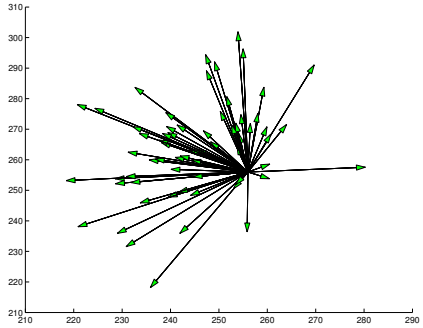

(c) 4h

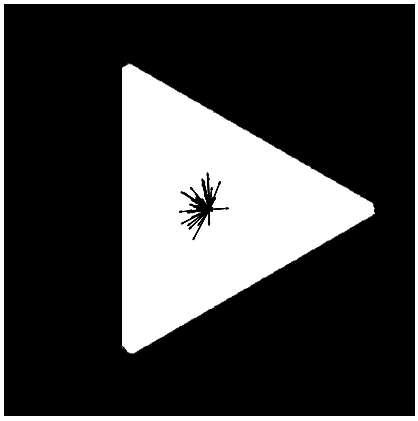

(d) 4h

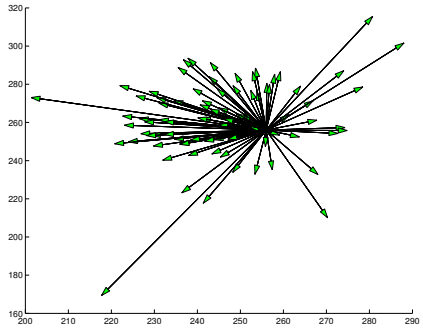

(e) 6h

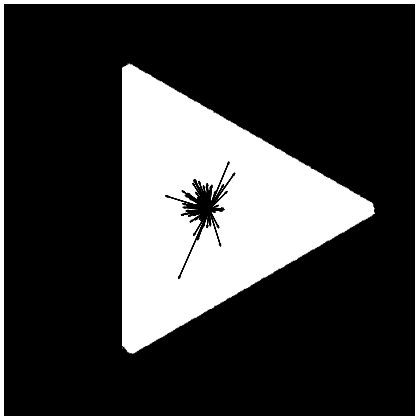

(f) 6h

Figure 8.9: *Vectors pointing from the cell center towards the centrosome in triangular cells. The vectors preferentially point away from the nucleus (c.f. Fig. 8.2).*

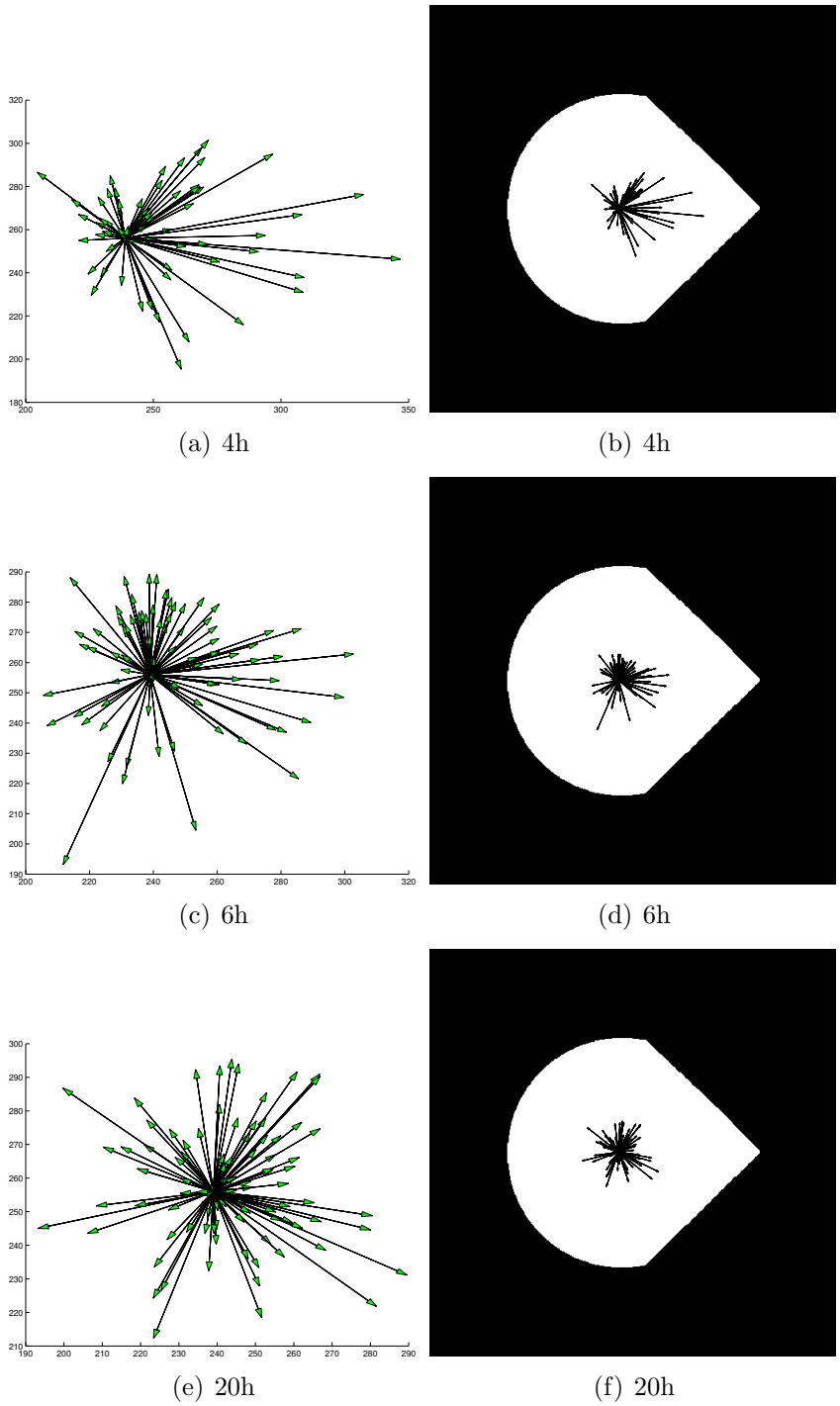

(a) 4h (b) 4h

(c) 6h (d) 6h

(e) 20h (f) 20h

Figure 8.10: *Vectors pointing from the cell center towards the centrosome in crossbow-shaped cells. For large time points they are uniformly oriented (c.f. Fig. 8.3).*

8.3 Simulation results

Since the experiments and simulations by Holy et al. [55] it is known that a microtubule aster can find the center of a dish in vitro. This aster forms part of the centrosome in vivo (see Section 3.4). Microtubules are semiflexible polymers that grow and shrink stochastically in a process called "dynamic instability". Depending on the molecular state of the polymer tip, the microtubules either grow with a certain rate or they depolymerize. The switching between these two states occurs stochastically [122, 123]. Here, we perform simulations of microtubules that undergo dynamic instability. We additionally attach a nucleus to the centrosome and apply triangular boundary conditions to model the situation in triangular cells. Furthermore, we take care of the fact that the cell height decreases towards the sides by imposing a potential acting on the nucleus. This simple model already reproduces many features of the experimental data observed for triangular cells. Even better results are obtained when adding steric restrictions so that microtubules avoid the nucleus and also interact with the cell boundary.

8.3.1 Simulation method

The principal components of the simulation is an aster, from which microtubules grow radially in random directions. The cell boundary has a triangular shape, while the nucleus is simulated as a circle. Centrosome and nucleus are connected via a stiff rod, which is free to move on the nucleus surface.

Motion of particles is simulated via Brownian dynamics, i.e. in the overdamped limit of the Langevin equation where inertia terms are neglected. This is adequate, as lengths scales in a cell are small and the cytoplasm is a very viscous medium, i.e. we work in the low Reynolds number regime and viscous forces dominate over inertial forces.

Hence, positions of particles are calculated via

$$\vec{x}(t+\Delta t) = \vec{x}(t) + \Delta t \frac{\vec{F}}{\gamma} + \vec{\xi} \tag{8.1}$$

where $\vec{\xi}$ is a random number with zero mean and variance $2D\Delta t$ (D: diffusion coefficient), $\vec{F}$ are the deterministic, conservative forces. The friction coefficient γ is related to the diffusion coefficient via the fluctuation-dissipation theorem, i.e. $\gamma = \frac{k_B T}{D}$. As strong deterministic forces caused by the cell membrane and microtubules are at work, we also neglect the random force $\vec{\xi}$. Hence, in the simulations we work with effective parameters including the friction γ.

We simulated an aster from which 50 microtubules radially emanate in randomly drawn directions. Microtubules undergo the process of dynamic instability: They

stochastically switch between a growing and a shrinking state, in which they either polymerize with a rate $p_{grow} = 10\mu m/min$ or depolymerize with a rate $p_{shrink} = 15\mu m/min$. The probabilities for switching from one modus to the other depend on the microtubule length according to

$$pcat = 1 \times 10^{-3} L_{MT} \Delta t \tag{8.2}$$

$$pres = 3.33 \times 10^{-3} (L_{max} - L_{MT}) \Delta t \tag{8.3}$$

where pcat and pres are the probabilities to switch to the shrinking or growing state respectively, L_{MT} is the current microtubule length, and $L_{max} = 25\mu m$ defines the length above with microtubules cannot switch back into the growing state. Rates for switching and (de-)polymerization were taken from [121]. When a microtubule completely depolymerizes, a new microtubule will grow in a random direction. For each microtubule, the starting point, i.e. the centrosome, is stored, as well as a vector that defines its growing direction, its current number of monomers and its state (growing/shrinking). Microtubules are initialized with a starting length of one monomer, being in the growing state.

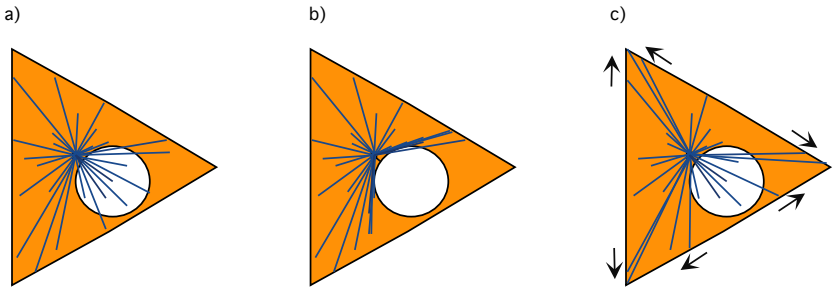

Figure 8.11: *Scheme of different simulation features: (a) and (b) depict two possible ways of microtubule interactions with the nucleus. In (a) microtubules do not interact with the nucleus. In (b) new microtubules are not allowed to grow in the direction of the nucleus. Instead they grow tangentially to the nucleus, thus forming microtubule bundles next to the nucleus. However, the nucleus can move over already existing microtubules. (c) depicts an option for the microtubule interactions at the cell boundary: Microtubules that touch the boundary slowly slide towards the next cell corner ("slip boundary conditions"). This can be combined with option a or b. Here: combined with option a.*

The triangular cell shape is implemented as the triangle defined by the points $(0, R/2)$, $(0, -R/2)$ and $(-\sqrt{3}R/2, 0)$. $R = 40.5\mu m$ so that the size of the triangle corresponds to the size of cells in the experiment. In each time step, the position of each microtubule tip is calculated, and it is checked if it intersects the lines defining the triangle. When a microtubule touches the boundary, it exerts a pushing force along the microtubule onto the aster, neglecting the finite bending modulus of

the filaments. The strength of the pushing force is proportional to its component perpendicular to the cell membrane, i.e. each microtubule j that hits the boundary moves the centrosome by

$$\vec{x_j} = -fmax\ (\vec{v}\vec{e})\vec{v} \tag{8.4}$$

where $fmax = 10^{-3}\Delta t$, $\vec{v}$ is the unit vector giving the growing direction of the microtubule and $\vec{e}$ the normal to the cell boundary. The total force on the centrosome caused by all microtubules that touch the cell boundary is $\vec{F}_{mt} = \sum_j \vec{F}_j$.

Cell corners in the experiment are rounded and microtubules will hit them quasi perpendicular. In the simulation, microtubules push back with maximum force along the microtubules if the microtubule direction deviates by less than 2° from a straight line connecting the aster and a corner of the triangle.

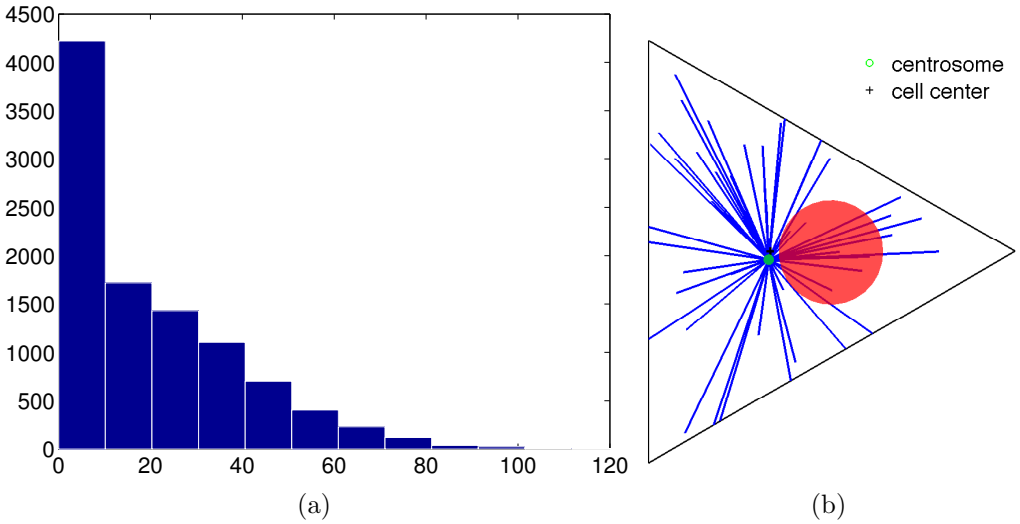

(a) (b)

Figure 8.12: *(a) Distribution of microtubule length with the parameters used for the simulations. (b) Typical snapshot of microtubules, centrosome, and nucleus for simulation model A.*

The nucleus was modeled as a sphere of radius $R = 5\mu m$. With this radius, the nucleus covers about the same area fraction of the cell as in the experimental data. The surface of the nucleus is linked to the aster via a rigid rod of length $l_{rod} = 1\mu m$. During initialization, it is placed at a random direction relative to the centrosome within the cell.

Similar to the microtubules, it is checked for each time point if the nucleus touches the cell boundary. In that case, a repulsive force $\vec{F}_{membrane}$ moves the nucleus by the distance $\vec{x}_{nuc} = -10^3\ fmax\ \vec{e}$, where $\vec{e}$ and fmax are defined as above.

As the centrosome and nucleus are linked, they exceed forces on each other. We assume that the link is a stiff rod, but with an anchoring point of this rod on the

nucleus surface that can slide along it (the nucleus membrane is fluid), i.e. the centrosome can freely move tangentially to the nucleus surface.

Thus, forces acting on the centrosome can move it tangentially along the surface of the nucleus without influencing the motion of the nucleus. However, if it is pushed perpendicular to the nucleus surface, it has to drag the nucleus with it or push it away. For implementation, the total force of microtubules on the centrosome is split in a component perpendicular and tangentially to the nucleus surface. The tangential component only moves the centrosome along the nucleus surface. However, the perpendicular component acts on both, nucleus and centrosome.

We assume that forces acting on the nucleus move centrosome and nucleus in the same way. This takes care of the fact that the aster is a delicate and thin structure and its main components, the microtubules can be considered as one-dimensional objects, i.e. the friction of this object compared to the friction of the massive nucleus can be neglected. Therefore, the movement of the centrosome simply follows the movement of the nucleus. This approximation is similar to the Born-Oppenheimer approximation in atomic physics that is frequently used when calculating the motion of atom nucleus and electrons in atoms or molecules. Here, one assumes that the electrons adapt immediately to motions of the nucleus, which has a far bigger mass and moves slowly.

In total, the forces acting on nucleus and centrosome in each time step are:

$$\vec{F}_{nuc} = \vec{F}_{mt\parallel} + \vec{F}_{membrane} \tag{8.5}$$

$$\vec{F}_{centrosome} = \vec{F}_{mt} + \vec{F}_{membrane} \tag{8.6}$$

where $\vec{F}_{mt\parallel}$ is the component of $\vec{F}_{mt}$ along the connection centrosome - nucleus center.

This simplest model is extended to include the fact that the cell decreases in height when approaching the sides. To this end, a harmonic potential acting on the nucleus is added ($V = k(\vec{x_{nuc}} - \vec{x_{center}})^2/2$), causing a displacement of $\vec{\Delta x} = k(\vec{x}_{center} - \vec{x}_{nuc})$, where $k = 1 \times 10^{-6}$, $\vec{x}_{nuc}$ and $\vec{x}_{center}$ are the positions of the nucleus and the cell center, respectively. This force is included in $\vec{F}_{membrane}$ in Eq. 8.6.

Furthermore, another interaction possibility of the microtubules with the nucleus is implemented: So far, microtubules ignore the nucleus and simply cross it. In the second option implemented, microtubules cannot grow in the direction occupied by the nucleus. Instead, they grow tangentially to the nucleus at the side closest to their originally determined growing direction. This corresponds to microtubules that hit the nucleus and search for a away around it. So, microtubules are focused to grow directly next to the nucleus. In all cases, the nucleus can move above existing microtubules without affecting them. The two approaches are depicted in Fig. 8.11a and b.

Additionally, we implemented a slow sliding of microtubules along the cell walls into the corners of the triangle when hitting the cell boundary (see Fig. 8.11c). This option was inspired by an observation in [124], where microtubules were observed to slide along the non-adhesive sides of crossbow-shaped Cytoo patterns. They then accumulate at the adhesive sides. In the triangular cells, the adhesive pattern corresponds to a Y, so only the edges of the triangle provide points for attachment. Sliding is implemented as a deterministic motion with a small increment of $\Delta x_{slide} = 10^{-4}\mu m$ per time step ($\Delta t = 10ms$) along the cell boundary. Such small increments lead to a realistic situation in which some but not all microtubules are accumulated in the edges. The slowness of the sliding process can be explained by the fact that, in vivo, microtubules interact with dense actin/intermediate filament networks in the cell periphery. The direction of sliding is determined by the angle between the microtubule and the cell boundary (c.f. 8.11c).

Simulations were done in Fortran. All simulations run for a total of 3.6 million steps. With a time increment of 10ms, this corresponds to a real time of 10h.

8.3.2 Simulation results

First, we looked at the length distribution of the microtubules. In Fig. 8.12a the distribution of microtubules lengths with the dynamics used in all simulations are shown. Many short microtubules exist, but a certain fraction is large enough to touch the walls of the cells independent of the current position of the aster. The mean length of the microtubules is $L_{mean} = 19.5\mu m$. In Fig. 8.12b a typical snapshot of the simulations (model A, for explanation see below) is shown.

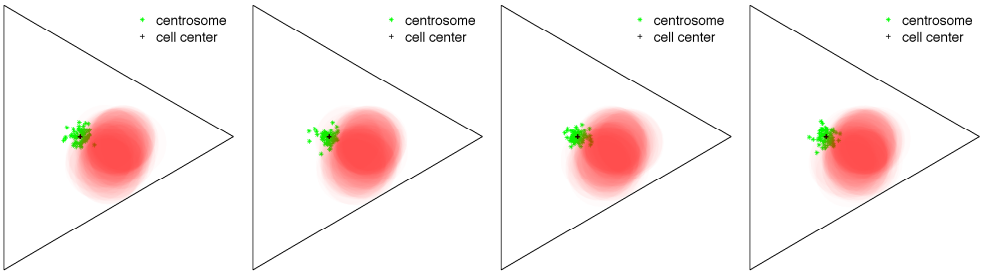

(a) 1/4 total time (b) 1/2 total time (c) 3/4 total time (d) total time

Figure 8.13: *Ensemble of nuclei (red) and centrosomes (green) for independent simulation runs of model A. Distributions are shown at 1/4, 1/2, 3/4 of the total simulation time and at the end point. At all times, the pictures look qualitatively the same, so the simulation has clearly reached its equilibrium.*

First, we simulated the situation shown in setup 1a) in Fig. 8.11. We will refer to this model as "setup A" in the following. Here, microtubules keep their direction of growth and the nucleus is attached to the aster. However, no further interactions between microtubules and nucleus exist. For details on the simulation, the Section 8.3.1.

We first checked that the stationary state is reached within our simulation time. Therefore, the situation after 1/4, 1/2, 3/4 and at the end of the simulation were visualized (Fig. 8.13). Already after 1/4 of the total time, the steady state is reached.

For comparison the experimental and theoretical results are displayed in Fig. 8.14 (experimental data: triangular cells fixed 6h after seeding). For each, the overlay of the images as well as histograms of the angles between a horizontal line and the connection from the cell center to the centrosome or nucleus center are displayed.

Qualitatively, this very simple model can already reproduce some features of the experimental observations. The centrosome is positioned in the cell center, on the upper left of the nucleus. The mean and standard deviations of the distances cell center - centrosome and cell center - nucleus center are $distance_{centrosome} = (1.1 \pm 0.6)\mu m$ and $distance_{nucleus} = (5.9 \pm 0.8)\mu m$. This compares quite well to experimental distances for triangular cells at 6h, $distance_{centrosome} = (3.4 \pm 1.8)\mu m$ and $distance_{nucleus} = (3.9 \pm 1.6)\mu m$. Still, the variations in the experimental data are about 2-to 3-fold higher than in the simple simulation.

However, the centrosome lies too close to the cell center and its angular distribution (see Fig. 8.14e) is uniform in contradiction to the experimental observations (see Fig. 8.14b). When looking at the histogram of angles for the nucleus and the overlay pictures, it also becomes obvious that the nucleus preferentially lies in the direction of the corner of the triangle in the simulation results (c.f. Fig. 8.14c and f). Additionally, in the experimental data the nucleus mostly includes the cell center - which is not observed in the simulation with model A.

In model A, the nucleus only experienced a hard core repulsion when touching the cell boundary. However, in real life a cell decreases in height towards the edges, thus pushing the nucleus closer to the cell center. Towards the edges of the triangular cells, the height decreases even faster than along the sides of the triangle.

To include this additional effect, we added a weak harmonic potential to the cell center, acting only on the nucleus (c.f. Section 8.3.1. Results for this model B are shown in Fig. 8.15. Here, the position of the centrosome and the nucleus show a better agreement with the experimental data. The centrosome is preferentially oriented away from the nucleus (c.f. the angular distributions 8.14b and 8.15b). The nucleus now includes the cell center more often. However, its preferential orientation is still towards the corner of the triangle. The mean and standard deviation of the distances cell center - centrosome and cell center - center nucleus

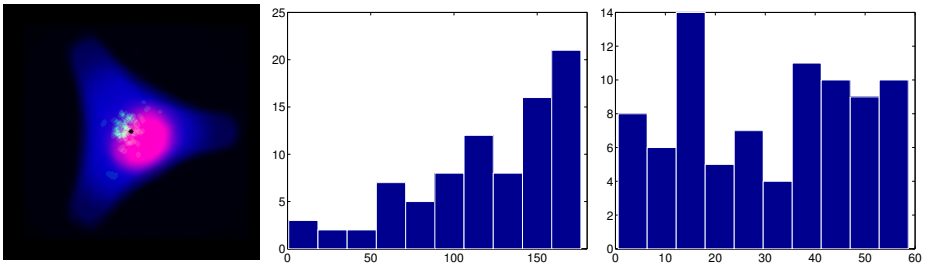

(a) overlay - experiment

(b) distribution $\alpha_{centrosome}$ - experiment

(c) distribution $\alpha_{nucleus}$ - experiment

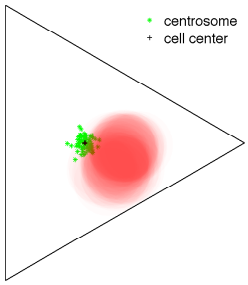

(d) overlay - simulation

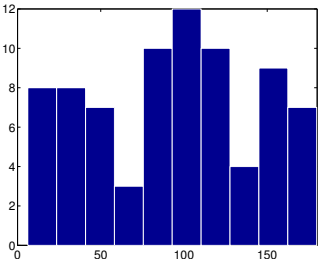

(e) distribution $\alpha_{centrosome}$ - simulation

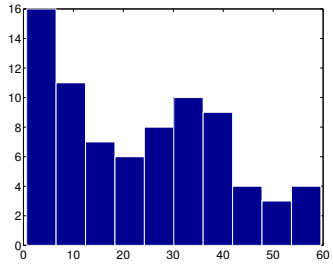

(f) distribution $\alpha_{nucleus}$ - simulation

Figure 8.14: *Comparison of experimental data for triangular cells, fixed 6h after cell seeding and simulation results with setup A. Left: Overlay of all cells imaged/simulation runs: centrosome (green), nucleus (red). The cell center is marked by a black cross/point. Distribution of $\alpha_{centrosome}$, the angle between a horizontal line and the vector connecting the cell center to the centrosome. Right: Distribution of $\alpha_{nucleus}$, the angle between a horizontal and the vector connecting the cell center to the nucleus center.*

now are $distance_{centrosome} = (1.2 \pm 0.7)\mu m$ and $distance_{nucleus} = (5.2 \pm 0.9)\mu m$, slightly more towards to the values obtained in experiment.

Apart from being two-dimensional, the model so far still includes one very crude assumption: Microtubules do not interact with the nucleus and simply grow through it. However, in the cell, microtubules obviously cannot do so. They must grow above or below the nucleus or bend around it as much as they can (microtubules are relatively stiff, with a persistence length of around 5mm, much longer than the size of a cell [125]). To include this effect in the model, newly emerging microtubules were not allowed to grow into the direction of the nucleus anymore. When just letting them grow in a random direction in free space, the nucleus gets pushed into one of the corners of the cell, as expected. However, a more realistic picture emerges when microtubules that wanted to grow through the nucleus are pushed

to the side of the nucleus and grow tangentially to it instead. By that forces get balanced and centrosome and nucleus keep a central position in the cell. For an illustration of this model see Fig. 8.11b.

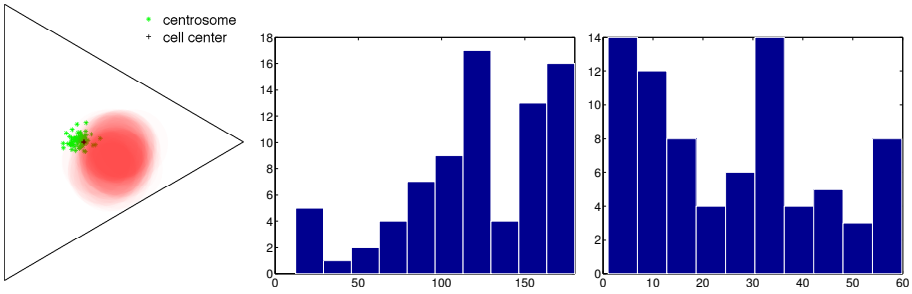

(a) overlay (b) distribution $\alpha_{centrosome}$ (c) distribution $\alpha_{nucleus}$

Figure 8.15: *Simulation results for setup B, including a harmonic potential acting on the nucleus. Left: Overlay of all simulation runs: centrosome (green), nucleus (red). The cell center is marked by black cross. Middle: Distribution of $\alpha_{centrosome}$, the angle between a horizontal line and the vector connecting the cell center to the centrosome. Right: Distribution of $\alpha_{nucleus}$, the angle between a horizontal and the vector connecting the cell center to the nucleus center.*

Additionally, it has been observed for cells growing on micropatterns that microtubules can only attach on the cell membrane on adhesive edges of the cell [118]. For triangular cells the stamped pattern is Y-shaped, i.e. only the edges are adhesive. On non-adhesive sides microtubules slide along the cell membrane until they find an adhesive spot. This effect was also included in the simulation by letting microtubules move along the wall when hitting an the cell boundary (see Fig. 8.11c).

Including the interaction of the microtubules with the nucleus and the sliding along the cell walls towards the edges and fine-tuning the parameters finally leads to model C (see Fig. 8.16). The harmonic potential of model B was kept.

Model C, now reproduces the experiment well: The angular distribution of the nucleus position agrees well with the experimental result. Also, the cell center now lies within in the nucleus. This can also be seen in the distance between cell center and the nucleus, which now agrees with the experimental distance within the standard deviation: model C: $distance_{nucleus} = (2.9 \pm 0.8)\mu m$, experimental: $distance_{nucleus} = (3.9 \pm 1.6)\mu m$. Also the distance cell center - centrosome agrees well: model C: $distance_{centrosome} = (3.1 \pm 0.8)\mu m$ and experimental: $distance_{centrosome} = (3.4 \pm 1.8)\mu m$. The preferential position (see angular distributions Fig. 8.16b and Fig. 8.14b) of the centrosome also can be reproduced.

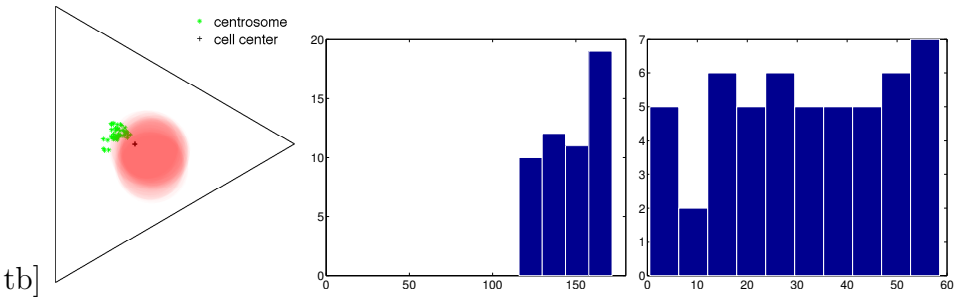

tb]

(a) overlay (b) distribution $\alpha_{centrosome}$ (c) distribution $\alpha_{nucleus}$

Figure 8.16: *Simulation results for setup C, including a harmonic potential, accumulation of microtubules next to the nucleus and sliding of microtubules along the cell walls. Left: Overlay of all simulation runs: centrosome (green), nucleus (red). The cell center is marked by a black cross. Middle: Distribution of $\alpha_{centrosome}$, the angle between a horizontal line and the vector connecting the cell center to the centrosome. Right: Distribution of $\alpha_{nucleus}$, the angle between a horizontal and the vector connecting the cell center to the nucleus center.*

However, variations in the positions of centrosome and nucleus are still too small. Also, in the experiment the centrosome has a broader angular distribution and it is sometimes closer to the cell center. This cannot be captured in our model as it is probably an effect of the three-dimensionality. Even if in the triangular cells the centrosome is mostly seen to lie beside the nucleus in the images, it will sometimes moves a bit up or down and is then seen to lie "inside" the nucleus in the 2d image. This leads to a smaller distance of the centrosome from the the cell center and a broadening of the angular distribution.

An additional source of noise in the experimental data is the shape of the nucleus. It is rarely spherical and differs from cell to cell.

Adding a dipole and quadrupole moment to the nucleus in the simulations and making a real three-dimensional simulation would probably increase the agreement even further. Possibly, also crossbow cells which are thicker and where hence the centrosome lies more often on top of the nucleus, could be captured by a three-dimensional model.

8.4 Discussion

Using cells grown on micropatterns, we have studied the position of centrosome, Golgi apparatus and nucleus in triangular and crossbow-shaped cells. For all organelles we find a surprisingly high variability in the positions, contradicting the

idea of a "standard cell" emerging due to micropatterns [118, 117]. The noise that remains in the spatial organization will most probably also influence functionality, such as transport rates through the secretory pathway.

For both geometries, we find a good correlation of the position of the Golgi apparatus and the centrosome. The centrosome lies mostly close to the nucleus surface and in the triangular cells besides it. Crossbow-shaped cells seem to be thicker, so that the centrosome more frequently lies on top of the nucleus. When imagining the three-dimensional shape of a triangular and a crossbow cell, it appears logical that there is more room in the middle of the crossbow cell. In a tetrahedron (triangle) of the same maximum height as a circular shape (crossbow) the height drops faster when approaching the edges the shape. So, in crossbow cells there is space to pile the centrosome and the Golgi apparatus onto the nucleus.

Furthermore, the centrosome positions not precisely at the cell center, which one would expect if only pushing forces from microtubules existed. For triangular cells the centrosome is preferentially shifted (with respect to the cell center) away from the nucleus.

To explain the position of the centrosome and the nucleus in triangular cells, we set up a two-dimensional simulation model. Basic features of the model are microtubules that grow radially from a centrosome and undergo dynamic instability while growing. When hitting the triangular boundary of the cell, microtubules transmit forces on the centrosome. Additionally, a nucleus is attached to the centrosome. The cell membrane is pushing the nucleus towards the middle of the cell via a harmonic potential. This mimics the fact that the cell decreases in height towards the cell periphery. This basic model already reproduces many features of the experimental data.

All features of the experiment can (at least qualitatively) be reproduced in model C, which is biologically more realistic than the simplest model (A). Model C includes steric restriction of the microtubules by the nucleus and hence forces microtubules to accumulate next to it. Additional sliding of microtubules along the non-adhesive cell walls was added to increase agreement with experimental observations in [118]. Due to the sliding, some microtubules will also reach the region behind the nucleus. In reality, this region would also be reached as microtubules would bend a little around the nucleus. Together with the feature that microtubules undergo dynamic instability, this provides a quite realistic model for microtubules.

To explain the noise in the data, one would probably need to take the shape of the nucleus and its liquid properties into account. Additional improvement could be made by using a real 3D model that could then also explain the positions of organelles in crossbow-shaped cells.

Interestingly, not many direct interactions of the nucleus are needed to explain its position. The model only includes a harmonic potential to mimic the fact that the

cell becomes less high towards the sides and the membrane thus pushes the nucleus back. All other positioning and the dynamics is only achieved via the link of the nucleus to the centrosome. Especially, the microtubules do not push directly on the nucleus.

The model thus suggests that two forces without any further regulating mechanisms are sufficient to explain the data. Microtubules are pushing the centrosome and the cell membranes pushes the nucleus towards the cell center to position the centrosome and the nucleus. As one of the forces acts on the centrosome and one on the nucleus, it is also clear that some experimental data suggests that the centrosome positions the nucleus and some vice versa (see Section 3.4). One might speculate that the predominance of one of the forces depends on the cell type and external conditions used: In a higher cell with a more elastic membrane the nucleus would experience less force from the membrane, thus giving the microtubules more importance. For future work, more experimental data could be collected and tested against the model suggested here.

Bibliography

[1] Gernot Guigas, Claudia Kalla, and Matthias Weiss. The degree of macromolecular crowding in the cytoplasm and nucleoplasm of mammalian cells is conserved. *FEBS Lett*, 581(26):5094–5098, Oct 2007.

[2] Gernot Guigas and Matthias Weiss. Sampling the cell with anomalous diffusion - the discovery of slowness. *Biophys J*, 94(1):90–94, Jan 2008.

[3] José M G Vilar, Hao Yuan Kueh, Naama Barkai, and Stanislas Leibler. Mechanisms of noise-resistance in genetic oscillators. *Proc Natl Acad Sci U S A*, 99(9):5988–92, Apr 2002.

[4] Nitzan Rosenfeld, Jonathan W Young, Uri Alon, Peter S Swain, and Michael B Elowitz. Gene regulation at the single-cell level. *Science*, 307(5717):1962–5, Mar 2005.

[5] Berend Snijder, Raphael Sacher, Pauli Rämö, Eva-Maria Damm, Prisca Liberali, and Lucas Pelkmans. Population context determines cell-to-cell variability in endocytosis and virus infection. *Nature*, 461(7263):520–3, Sep 2009.

[6] S. Nehls, E. L. Snapp, N. B. Cole, K. J. Zaal, A. K. Kenworthy, T. H. Roberts, J. Ellenberg, J. F. Presley, E. Siggia, and J. Lippincott-Schwartz. Dynamics and retention of misfolded proteins in native er membranes. *Nat Cell Biol*, 2(5):288–295, May 2000.

[7] J. Philibert. One and a half century of diffusion: Fick, einstein, before and beyond. *Diffusion Fundamentals*, 4(6):1–19, 2006.

[8] Harvey Scher and Elliott W. Montroll. Anomalous transit-time dispersion in amorphous solids. *Phys. Rev. B*, 12(6):2455–2477, Sep 1975.

[9] Matthias Weiss, Hitoshi Hashimoto, and Tommy Nilsson. Anomalous protein diffusion in living cells as seen by fluorescence correlation spectroscopy. *Biophys J*, 84(6):4043–4052, Jun 2003.

[10] L. F. Richardson. Atmospheric diffusion shown on a distance-neighbour graph. *Royal Society of London Proceedings Series A*, 110:709–737, 1926.

[11] M. Levandowsky, B. White, and F. Schuster. Random movements of soil amebas. *Acta Protozoologica*, 36:237 – 248 237 – 248, 1997.

[12] S. Havlin D. Ben-Avraham. *Diffusion and Reactions in Fractals and Disordered Systems*. Cambridge University Press, 2000.

[13] Armin Bunde and Shlomo Havlin, editors. *Fractals and disordered systems*. Springer-Verlag New York, Inc., New York, NY, USA, 1991.

[14] M. J. Saxton. Anomalous diffusion due to obstacles: a monte carlo study. *Biophys J*, 66(2 Pt 1):394–401, Feb 1994.

[15] M. J. Saxton. Lateral diffusion in an archipelago. single-particle diffusion. *Biophys J*, 64(6):1766–1780, Jun 1993.

[16] M. J. Saxton. Lateral diffusion in a mixture of mobile and immobile particles. a monte carlo study. *Biophys J*, 58(5):1303–1306, Nov 1990.

[17] Jean-Philippe Bouchaud and Antoine Georges. Anomalous diffusion in disordered media: Statistical mechanisms, models and physical applications. *Physics Reports*, 195:127 – 293, 1990.

[18] Havlin, Kiefer, and Weiss. Anomalous diffusion on a random comblike structure. *Phys Rev A*, 36(3):1403–1408, Aug 1987.

[19] Michael J Saxton. A biological interpretation of transient anomalous subdiffusion. i. qualitative model. *Biophys J*, 92(4):1178–1191, Feb 2007.

[20] Y He, S Burov, R Metzler, and E Barkai. Random time-scale invariant diffusion and transport coefficients. *Phys Rev Lett*, 101(5):058101, Aug 2008.

[21] Ralf Metzler and Joseph Klafter. The random walk's guide to anomalous diffusion: a fractional dynamics approach. *Physics Reports*, 339:1 – 77, 2000.

[22] J. Lippincott-Schwartz, T. H. Roberts, and K. Hirschberg. Secretory protein trafficking and organelle dynamics in living cells. *Annu Rev Cell Dev Biol*, 16:557–589, 2000.

[23] Lars Ellgaard and Ari Helenius. Quality control in the endoplasmic reticulum. *Nat Rev Mol Cell Biol*, 4(3):181–191, Mar 2003.

[24] N. B. Cole, C. L. Smith, N. Sciaky, M. Terasaki, M. Edidin, and J. Lippincott-Schwartz. Diffusional mobility of golgi proteins in membranes of living cells. *Science*, 273(5276):797–801, Aug 1996.

[25] Teresa Sprocati, Paolo Ronchi, Andrea Raimondi, Maura Francolini, and Nica Borgese. Dynamic and reversible restructuring of the er induced by pdmp in cultured cells. *J Cell Sci*, 119(Pt 15):3249–3260, Aug 2006.

[26] B. D. Hughes, B. A. Pailthorpe, L. R. White, and W. H. Sawyer. Extraction of membrane microviscosity from translational and rotational diffusion coefficients. *Biophys J*, 37(3):673–676, Mar 1982.

[27] D. J. Stephens, N. Lin-Marq, A. Pagano, R. Pepperkok, and J. P. Paccaud. Copi-coated er-to-golgi transport complexes segregate from copii in close proximity to er exit sites. *J Cell Sci*, 113 (Pt 12):2177–2185, Jun 2000.

[28] C Guerkan, SM Stagg, P Lapointe, and WE Balch. The copii cage: unifying principles of vesicle coat assembly. *Nat Rev Mol Cell Biol*, 7:727–38, 2006.

[29] T. Kirchhausen. Three ways to make a vesicle. *Nat Rev Mol Cell Biol*, 1(3):187–198, Dec 2000.

[30] J. F. Presley, N. B. Cole, T. A. Schroer, K. Hirschberg, K. J. Zaal, and J. Lippincott-Schwartz. Er-to-golgi transport visualized in living cells. *Nature*, 389(6646):81–85, Sep 1997.

[31] George H Patterson, Koret Hirschberg, Roman S Polishchuk, Daniel Gerlich, Robert D Phair, and Jennifer Lippincott-Schwartz. Transport through the golgi apparatus by rapid partitioning within a two-phase membrane system. *Cell*, 133(6):1055–67, Jun 2008.

[32] Benjamin S Glick and Akihiko Nakano. Membrane traffic within the golgi apparatus. *Annu Rev Cell Dev Biol*, 25:113–32, 2009.

[33] Benjamin S Glick. Can the golgi form de novo? *Nat Rev Mol Cell Biol*, 3(8):615–9, Aug 2002.

[34] H H Mollenhauer and D J Morré. Perspectives on golgi apparatus form and function. *J Electron Microsc Tech*, 17(1):2–14, Jan 1991.

[35] B S Glick. Organization of the golgi apparatus. *Curr Opin Cell Biol*, 12(4):450–6, Aug 2000.

[36] A. M. de Silva, W. E. Balch, and A. Helenius. Quality control in the endoplasmic reticulum: folding and misfolding of vesicular stomatitis virus g protein in cells and in vitro. *J Cell Biol*, 111(3):857–866, Sep 1990.

[37] C. Hammond and A. Helenius. Quality control in the secretory pathway: retention of a misfolded viral membrane glycoprotein involves cycling between the er, intermediate compartment, and golgi apparatus. *J Cell Biol*, 126(1):41–52, Jul 1994.

[38] A. Helenius. How n-linked oligosaccharides affect glycoprotein folding in the endoplasmic reticulum. *Mol Biol Cell*, 5(3):253–265, Mar 1994.

[39] E. S. Trombetta and A. Helenius. Lectins as chaperones in glycoprotein folding. *Curr Opin Struct Biol*, 8(5):587–592, Oct 1998.

[40] G. Kuznetsov and S. K. Nigam. Folding of secretory and membrane proteins. *N Engl J Med*, 339(23):1688–1695, Dec 1998.

[41] S. Munro and H. R. Pelham. A c-terminal signal prevents secretion of luminal er proteins. *Cell*, 48(5):899–907, Mar 1987.

[42] R. D. Teasdale and M. R. Jackson. Signal-mediated sorting of membrane proteins between the endoplasmic reticulum and the golgi apparatus. *Annu Rev Cell Dev Biol*, 12:27–54, 1996.

[43] M R Jackson, T Nilsson, and P A Peterson. Identification of a consensus motif for retention of transmembrane proteins in the endoplasmic reticulum. *EMBO J*, 9(10):3153–62, Oct 1990.

[44] W. E. Balch, J. M. McCaffery, H. Plutner, and M. G. Farquhar. Vesicular stomatitis virus glycoprotein is sorted and concentrated during export from the endoplasmic reticulum. *Cell*, 76(5):841–852, Mar 1994.

[45] S. R. Pfeffer and J. E. Rothman. Biosynthetic protein transport and sorting by the endoplasmic reticulum and golgi. *Annu Rev Biochem*, 56:829–852, 1987.

[46] Anna Mezzacasa and Ari Helenius. The transitional er defines a boundary for quality control in the secretion of tso45 vsv glycoprotein. *Traffic*, 3(11):833–849, Nov 2002.

[47] Anna Dukhovny, Andreas Papadopulos, and Koret Hirschberg. Quantitative live-cell analysis of microtubule-uncoupled cargo-protein sorting in the er. *J Cell Sci*, 121(Pt 6):865–876, Mar 2008.

[48] Erik L Snapp, Ajay Sharma, Jennifer Lippincott-Schwartz, and Ramanujan S Hegde. Monitoring chaperone engagement of substrates in the endoplasmic reticulum of live cells. *Proc Natl Acad Sci U S A*, 103(17):6536–6541, Apr 2006.

[49] Asako Kamada, Hisao Nagaya, Taku Tamura, Masataka Kinjo, Hai-Ying Jin, Toshiharu Yamashita, Kowichi Jimbow, Hideo Kanoh, and Ikuo Wada. Regulation of immature protein dynamics in the endoplasmic reticulum. *J Biol Chem*, 279(20):21533–21542, May 2004.

[50] Ulrich Schmidt, Gernot Guigas, and Matthias Weiss. Cluster formation of transmembrane proteins due to hydrophobic mismatching. *Phys Rev Lett*, 101(12):128104, Sep 2008.

[51] Ulrich Schmidt and Matthias Weiss. Hydrophobic mismatch-induced clustering as a primer for protein sorting in the secretory pathway. *Biophys Chem*, 151(1-2):34–8, Sep 2010.

[52] Kakoli Mitra, Iban Ubarretxena-Belandia, Tomohiko Taguchi, Graham Warren, and Donald M Engelman. Modulation of the bilayer thickness of exocytic pathway membranes by membrane proteins rather than cholesterol. *Proc Natl Acad Sci U S A*, 101(12):4083–8, Mar 2004.

[53] Paolo Ronchi, Sara Colombo, Maura Francolini, and Nica Borgese. Transmembrane domain-dependent partitioning of membrane proteins within the endoplasmic reticulum. *J Cell Biol*, 181(1):105–118, Apr 2008.

[54] Bruce Alberts, Alexander Johnson, Julian Lewis, Martin Raff, Keith Roberts, and Peter Walter, editors. *Molecular biology of the cell, 4th Edition*. Garland Science, New York, 2002.

[55] T E Holy, M Dogterom, B Yurke, and S Leibler. Assembly and positioning of microtubule asters in microfabricated chambers. *Proc Natl Acad Sci U S A*, 94(12):6228–31, Jun 1997.

[56] Jean-Baptiste Manneville and Sandrine Etienne-Manneville. Positioning centrosomes and spindle poles: looking at the periphery to find the centre. *Biol Cell*, 98(9):557–65, Sep 2006.

[57] Christine Sütterlin and Antonino Colanzi. The golgi and the centrosome: building a functional partnership. *J Cell Biol*, 188(5):621–8, Mar 2010.

[58] François Pouthas, Philippe Girard, Virginie Lecaudey, Thi Bach Nga Ly, Darren Gilmour, Christian Boulin, Rainer Pepperkok, and Emmanuel G Reynaud. In migrating cells, the golgi complex and the position of the centrosome depend on geometrical constraints of the substratum. *J Cell Sci*, 121(Pt 14):2406–14, Jul 2008.

[59] Isabelle Dupin, Emeline Camand, and Sandrine Etienne-Manneville. Classical cadherins control nucleus and centrosome position and cell polarity. *J Cell Biol*, 185(5):779–86, Jun 2009.

[60] Sue Vaughan and Helen R Dawe. Common themes in centriole and centrosome movements. *Trends Cell Biol*, 21(1):57–66, Jan 2011.

[61] Daniel A Starr. A nuclear-envelope bridge positions nuclei and moves chromosomes. *J Cell Sci*, 122(Pt 5):577–86, Mar 2009.

[62] D. Magde, E.L. Elson, and W.W. Webb. Fluorescence correlation spectroscopy. ii. an experimental realization. *Biopolymers*, 13(1):29–61, Jan 1974.

[63] P.Schwille and E. Haustein. *Fluorescence Correlation Spectroscopy. An Introduction to its Concepts and Applications.* Biophysics Textbook Online, BTOL, 2002.

[64] M. Ehrenberg and R. Rigler. Fluorescence correlation spectroscopy applied to rotational diffusion of macromolecules. *Q Rev Biophys*, 9(1):69–81, Feb 1976.

[65] M. Kinjo and R. Rigler. Ultrasensitive hybridization analysis using fluorescence correlation spectroscopy. *Nucleic Acids Res*, 23(10):1795 –1799, May 1995.

[66] Gernot Guigas, Claudia Kalla, and Matthias Weiss. Probing the nanoscale viscoelasticity of intracellular fluids in living cells. *Biophys J*, 93(1):316–323, Jul 2007.

[67] Robert H Webb. Confocal optical microscopy. *Rep. Prog. Phys. 59*, 59(3):427–471, 1996.

[68] R. Rigler, U. Mets, J. Widengren, and P. Kask. Fluorescence correlation specroscopy with high count rate and low background: analysis of translational diffusion. *Eur Biophys J*, 22:169 – 175, 1993.

[69] C. J. Scandella, P. Devaux, and H. M. McConnell. Rapid lateral diffusion of phospholipids in rabbit sarcoplasmic reticulum. *Proc Natl Acad Sci U S A*, 69(8):2056–2060, Aug 1972.

[70] P. G. Saffman and M. Delbrueck. Brownian motion in biological membranes. *Proc Natl Acad Sci U S A*, 72(8):3111–3113, Aug 1975.

[71] Matthias Weiss, Markus Elsner, Fredrik Kartberg, and Tommy Nilsson. Anomalous subdiffusion is a measure for cytoplasmic crowding in living cells. *Biophys J*, 87(5):3518–3524, Nov 2004.

[72] Jedrzej Szymanski and Matthias Weiss. Elucidating the origin of anomalous diffusion in crowded fluids. *Phys. Rev. Lett.*, 103:038102, 2009.

[73] Jerker Widengren, Uelo Mets, and Rudolf Rigler. Fluorescence correlation spectroscopy of triplet states in solution: a theoretical and experimental study. *The Journal of Physical Chemistry*, 99(36):13368–13379, 1995.

[74] Elke Haustein and Petra Schwille. Ultrasensitive investigations of biological systems by fluorescence correlation spectroscopy. *Methods*, 29(2):153–66, Feb 2003.

[75] U. Haupts, S. Maiti, P. Schwille, and W. W. Webb. Dynamics of fluorescence fluctuations in green fluorescent protein observed by fluorescence correlation spectroscopy. *Proc Natl Acad Sci U S A*, 95(23):13573–13578, Nov 1998.

[76] J.Enderlein and I.Gregor. Using fluorescence lifetime for discriminating detector afterpulsing in fluorescence correlation spectroscopy. *Rev. Sci. Instrum.*, 76:033102, 2005.

[77] W. E. Moerner and M. Orrit. Illuminating single molecules in condensed matter. *Science*, 283:5408, 1999.

[78] M. Wachsmuth. *Fluoreszenzfluktuationsmikroskopie: Entwicklung eines Prototyps, Theorie und Messung der Beweglichkeit von Biomolekuelen im Zellkern.* PhD thesis, Ruprecht-Karls-Universitaet, Heidelberg, 2001.

[79] Samuel T Hess and Watt W Webb. Focal volume optics and experimental artifacts in confocal fluorescence correlation spectroscopy. *Biophys J*, 83(4):2300–17, Oct 2002.

[80] L. Ellgaard and A. Helenius. Quality control in the endoplasmic reticulum. *Nat. Rev. Mol. Cell Biol.*, 4(3):181–91, 2003.

[81] C. Gurkan, S. M. Stagg, P. Lapointe, and W. E. Balch. The copii cage: unifying principles of vesicle coat assembly. *Nat. Rev. Mol. Cell Biol.*, 7(10):727–38, 2006.

[82] U. Tatu and A. Helenius. Interactions between newly synthesized glycoproteins, calnexin and a network of resident chaperones in the endoplasmic reticulum. *J. Cell Biol.*, 136(3):555–65, 1997.

[83] S. Nehls, E. L. Snapp, N. B. Cole, K. J. Zaal, A. K. Kenworthy, T. H. Roberts, J. Ellenberg, J. F. Presley, E. Siggia, and J. Lippincott-Schwartz. Dynamics and retention of misfolded proteins in native er membranes. *Nat Cell Biol*, 2(5):288–95, 2000.

[84] W. E. Balch, J. M. McCaffery, H. Plutner, and M. G. Farquhar. Vesicular stomatitis virus glycoprotein is sorted and concentrated during export from the endoplasmic reticulum. *Cell*, 76(5):841–52, 1994.

[85] P. G. Saffman and M. Delbruck. Brownian motion in biological membranes. *Proc. Natl. Acad. Sci. USA*, 72(8):3111–3, 1975.

[86] H. X. Zhou, G. Rivas, and A. P. Minton. Macromolecular crowding and confinement: biochemical, biophysical, and potential physiological consequences. *Annu. Rev. Biophys.*, 37:375–97, 2008.

[87] H. Runz, K. Miura, M. Weiss, and R. Pepperkok. Sterols regulate er-export dynamics of secretory cargo protein ts-o45-g. *Embo J*, 25(13):2953–65, 2006.

[88] S. Rottger, J. White, H. H. Wandall, J. C. Olivo, A. Stark, E. P. Bennett, C. Whitehouse, E. G. Berger, H. Clausen, and T. Nilsson. Localization of three human polypeptide galnac-transferases in hela cells suggests initiation of o-linked glycosylation throughout the golgi apparatus. *J. Cell Sci.*, 111 (Pt 1):45–60, 1998.

[89] S. Granell, G. Baldini, S. Mohammad, V. Nicolin, P. Narducci, B. Storrie, and G. Baldini. Sequestration of mutated alpha1-antitrypsin into inclusion bodies is a cell-protective mechanism to maintain endoplasmic reticulum function. *Mol. Biol. Cell*, 19(2):572–86, 2008.

[90] M. Weiss, H. Hashimoto, and T. Nilsson. Anomalous protein diffusion in living cells as seen by fluorescence correlation spectroscopy. *Biophys J*, 84(6):4043–52, 2003.

[91] N. Malchus and M. Weiss. Elucidating anomalous protein diffusion in living cells with fluorescence correlation spectroscopy – facts and pitfalls. *J. Fluor.*, 20:19–26, 2010.

[92] J. P. Bouchaud and A. Georges. Anomalous diffusion in disordered media - statistical mechanisms, models and physical applications. *Physics Reports-Review Section of Physics Letters*, 195(4-5):127–293, 1990.

[93] M. Wachsmuth, W. Waldeck, and J. Langowski. Anomalous diffusion of fluorescent probes inside living cell nuclei investigated by spatially-resolved fluorescence correlation spectroscopy. *J. Mol. Biol.*, 298(4):677–89, 2000.

[94] M. Weiss, M. Elsner, F. Kartberg, and T. Nilsson. Anomalous subdiffusion is a measure for cytoplasmic crowding in living cells. *Biophys J*, 87(5):3518–24, 2004.

[95] I. Golding and E. C. Cox. Physical nature of bacterial cytoplasm. *Phys. Rev. Lett.*, 96(9):098102, 2006.

[96] G. Guigas, C. Kalla, and M. Weiss. Probing the nanoscale viscoelasticity of intracellular fluids in living cells. *Biophys. J.*, 93(1):316–23, 2007.

[97] R. Metzler and J. Klafter. The restaurant at the end of the random walk: recent developments in the description of anomalous transport by fractional dynamics. *J. Phys. A*, 37(31):R161–R208, 2004.

[98] C. Hammond and A. Helenius. Folding of vsv g protein: sequential interaction with bip and calnexin. *Science*, 266(5184):456–8, 1994.

[99] H. Nagaya, T. Tamura, A. Higa-Nishiyama, K. Ohashi, M. Takeuchi, H. Hashimoto, K. Hatsuzawa, M. Kinjo, T. Okada, and I. Wada. Regulated motion of glycoproteins revealed by direct visualization of a single cargo in the endoplasmic reticulum. *J. Cell Biol.*, 180(1):129–43, 2008.

[100] M. J. Saxton. Anomalous diffusion due to obstacles: a monte carlo study. *Biophys. J.*, 66:394–401, 1994.

[101] S. E. Trombetta and A. J. Parodi. Purification to apparent homogeneity and partial characterization of rat liver udp-glucose:glycoprotein glucosyltransferase. *J. Biol. Chem.*, 267(13):9236–40, 1992.

[102] A. V. Nikonov, E. Snapp, J. Lippincott-Schwartz, and G. Kreibich. Active translocon complexes labeled with gfp-dad1 diffuse slowly as large polysome arrays in the endoplasmic reticulum. *J. Cell Biol.*, 158(3):497–506, 2002.

[103] M. Molinari, C. Galli, O. Vanoni, S. M. Arnold, and R. J. Kaufman. Persistent glycoprotein misfolding activates the glucosidase ii/ugt1-driven calnexin cycle to delay aggregation and loss of folding competence. *Mol. Cell*, 20(4):503–12, 2005.

[104] P. Quinn, G. Griffiths, and G. Warren. Density of newly synthesized plasma membrane proteins in intracellular membranes ii. biochemical studies. *J Cell Biol*, 98(6):2142–7, 1984.

[105] L. M. Hendershot. Giving protein traffic the green light. *Nat Cell Biol*, 2(6):E105–E106, Jun 2000.

[106] J. D. Schrag, J. J. Bergeron, Y. Li, S. Borisova, M. Hahn, D. Y. Thomas, and M. Cygler. The structure of calnexin, an er chaperone involved in quality control of protein folding. *Mol Cell*, 8(3):633–644, Sep 2001.

[107] Verena Karsten, Ramanujan S Hegde, Anthony P Sinai, Mei Yang, and Keith A Joiner. Transmembrane domain modulates sorting of membrane proteins in toxoplasma gondii. *J Biol Chem*, 279(25):26052–26057, Jun 2004.

[108] Kakoli Mitra, Iban Ubarretxena-Belandia, Tomohiko Taguchi, Graham Warren, and Donald M Engelman. Modulation of the bilayer thickness of exocytic pathway membranes by membrane proteins rather than cholesterol. *Proc Natl Acad Sci U S A*, 101(12):4083–4088, Mar 2004.

[109] Shyam S Krishnakumar and Erwin London. The control of transmembrane helix transverse position in membranes by hydrophilic residues. *J Mol Biol*, 374(5):1251–1269, Dec 2007.

[110] Susana Granell, Giovanna Baldini, Sameer Mohammad, Vanessa Nicolin, Paola Narducci, Brian Storrie, and Giulia Baldini. Sequestration of mutated alpha1-antitrypsin into inclusion bodies is a cell-protective mechanism to maintain endoplasmic reticulum function. *Mol Biol Cell*, 19(2):572–586, Feb 2008.

[111] David B Williams. Beyond lectins: the calnexin/calreticulin chaperone system of the endoplasmic reticulum. *J Cell Sci*, 119(Pt 4):615–623, Feb 2006.

[112] Erik L Snapp, Ramanujan S Hegde, Maura Francolini, Francesca Lombardo, Sara Colombo, Emanuela Pedrazzini, Nica Borgese, and Jennifer Lippincott-Schwartz. Formation of stacked er cisternae by low affinity protein interactions. *J Cell Biol*, 163(2):257–269, Oct 2003.

[113] S Rajagopalan, Y Xu, and M B Brenner. Retention of unassembled components of integral membrane proteins by calnexin. *Science*, 263(5145):387–390, Jan 1994.

[114] G M Whitesides, E Ostuni, S Takayama, X Jiang, and D E Ingber. Soft lithography in biology and biochemistry. *Annu Rev Biomed Eng*, 3:335–373, 2001.

[115] Francois Pouthas, Philippe Girard, Virginie Lecaudey, Thi Bach Nga Ly, Darren Gilmour, Christian Boulin, Rainer Pepperkok, and Emmanuel G Reynaud. In migrating cells, the golgi complex and the position of the centrosome depend on geometrical constraints of the substratum. *J Cell Sci*, 121(Pt 14):2406–2414, Jul 2008.

[116] Manuel Thery, Andrea Jimenez-Dalmaroni, Victor Racine, Michel Bornens, and Frank Julicher. Experimental and theoretical study of mitotic spindle orientation. *Nature*, 447(7143):493–496, May 2007.

[117] Kristine Schauer, Tarn Duong, Kevin Bleakley, Sabine Bardin, Michel Bornens, and Bruno Goud. Probabilistic density maps to study global endomembrane organization. *Nat Methods*, 7(7):560–6, Jul 2010.

[118] Manuel Théry, Victor Racine, Matthieu Piel, Anne Pépin, Ariane Dimitrov, Yong Chen, Jean-Baptiste Sibarita, and Michel Bornens. Anisotropy of cell adhesive microenvironment governs cell internal organization and orientation of polarity. *Proc Natl Acad Sci U S A*, 103(52):19771–6, Dec 2006.

[119] K. Hirschberg, C. M. Miller, J. Ellenberg, J. F. Presley, E. D. Siggia, R. D. Phair, and J. Lippincott-Schwartz. Kinetic analysis of secretory protein traffic and characterization of golgi to plasma membrane transport intermediates in living cells. *J Cell Biol*, 143(6):1485–1503, Dec 1998.

[120] Steven J Altschuler and Lani F Wu. Cellular heterogeneity: do differences make a difference? *Cell*, 141(4):559–63, May 2010.

[121] François Nédélec. Computer simulations reveal motor properties generating stable antiparallel microtubule interactions. *J Cell Biol*, 158(6):1005–15, Sep 2002.

[122] T Mitchison and M Kirschner. Dynamic instability of microtubule growth. *Nature*, 312(5991):237–42, 1984.

[123] Ludovic Brun, Beat Rupp, Jonathan J Ward, and François Nédélec. A theory of microtubule catastrophes and their regulation. *Proc Natl Acad Sci U S A*, 106(50):21173–8, Dec 2009.

[124] Manuel Théry and Michel Bornens. Cell adhesion guides cell polarity. *Med Sci (Paris)*, 23(3):230–2, Mar 2007.

[125] F Gittes, B Mickey, J Nettleton, and J Howard. Flexural rigidity of microtubules and actin filaments measured from thermal fluctuations in shape. *J Cell Biol*, 120(4):923–34, Feb 1993.

Acknowledgement

At this point, I like to take the opportunity to thank the people that supported me during my PhD in one or the other way.

First, I cordially thank Prof. Dr. Michael Hausmann, member in my TAC committees and referee of my thesis in front of the faculty of physics, for his kind support and advice. I also thank Dr. Holger Erfle, also member of my TAC committees, for his interest in my work and discussions at the coffee machine.

Special thanks go to my supervisor Prof. Dr. Matthias Weiss. I highly appreciated the very valuable discussions and his optimism. Also, I very much thank him for giving me the chance to spend some time during my PhD to look at opportunities beyond science. I also want to thank all people that have been working in the group during my PhD for the kind atmosphere and very much regret that this vivid environment has faded away already about a year ago.

At that time, I joined the group seminars of the Pepperkok group. I thank Rainer Pepperkok and his whole group for the warm welcome and fruitful discussions.

For financial support and personal advice, I also want to thank my graduate school, HBIGS, especially Prof. Dr. Michael Lanzer, Dr. Rolf Lutz and Sandra Martini.

I also thank the group of Prof. Roland Eils for advises concerning molecular biology and microscopy and many chats in coffee corner.

For their great support throughout my life, I thank my parents, who are always there to give advise, and help whenever they can. I also thank my brother and sister for many joyful moments and for listening to whatever is on my mind. I am also grateful to my grandparents and other relatives for the interest they take in my work and life!

Very importantly, I also want to thank all my friends, without which the last years would have been far less pleasant! Furthermore, thanks go to my greatest flatmates ever, Tine and Doro, for distracting me from work in the evenings and making our flat a real home.

Finally, I thank my boyfriend Jan for the strength he gave in the last two years and for taking the effort to familiarize himself with microtubules and strangely shaped cells and discussing these topics with me.

List of publications

N. Malchus
Fluorescence Correlation Spectroscopy: Detecting and Interpreting the Mobility of Transmembrane Proteins In Vivo
Current Protocols in Toxicology, John Wiley &Sons, Inc., May 2011

N. Malchus and M. Weiss
Anomalous diffusion reports on the interaction of misfolded proteins with the quality control machinery in the endoplasmic reticulum
Biophys J, 99, pp. 13218, Aug 2010

N. Malchus and M. Weiss
Elucidating Anomalous Protein Diffusion in Living Cells with Fluorescence Correlation Spectroscopy - Facts and Pitfalls
J Fluorescence, 20, pp. 19-26, Jan 2010